UNIVERSITY OF OKLAHOMA

GRADUATE COLLEGE

MECHANISM AND INTERACTIONS OF INNER AND OUTER MEMBRANE COMPONENTS OF RND EFFLUX PUMPS

A DISSERTATION

SUBMITTED TO THE GRADUATE FACULTY

in partial fulfillment of the requirements for the

Degree of

DOCTOR OF PHILOSOPHY

By

ABIGAIL TAWIAH NTREH
Norman, Oklahoma
2016

Downloaded from SHAREOK. Persistent Handle URL: https://hdl.handle.net/11244/44931

MECHANISM AND INTERACTIONS OF INNER AND OUTER MEMBRANE COMPONENTS OF RND EFFLUX PUMPS

A DISSERTATION APPROVED FOR THE
DEPARTMENT OF CHEMISTRY AND BIOCHEMISTRY

BY

_____
Dr. Helen Zgurskaya, Chair

_____
Dr. Robert Cichewicz

_____
Dr. Charles Rice

_____
Dr. Valentin Rybenkov

_____
Dr. Anne Dunn

© Copyright by ABIGAIL TAWIAH NTREH 2016
All Rights Reserved.

Dedication

I would like to dedicate this writing to you, the reader of this work. Thank you for the time and attention you are giving to the summary of my works at the University of Oklahoma. To you, the one helping me edit, thank you and God bless you again for your time and willingness to help make the final product of this dissertation a wonder to many. To you, the one who has gone before me and helped get me to my point of completion and victory, God bless you for the encouragement and support to help keep focused and motivated. In all your endeavors, may you be consoled and encouraged as you go on to rise to newer heights than you ever imagined. To you, the one seeking inspiration for your own writing, may the grace of the Lord abound in your life as you allow the Spirit to work on your behalf to propel you unto good works. To you, the one who has yet to start on your own journey on the path to a post graduate degree, do not be intimidated or discouraged for you are on this earth for a purpose; let no one undermine you or take away from you that which brings you joy. The visions you have and the completion of your works is for the good of all men, don't back down now because society needs you to play your part. And to you, the one who isn't quite interested yet you are currently browsing through sections of the writing, may you be inspired by the Spirit in order to reignite whatever ideas were once so alive to you but has dimmed with time. Be encouraged that it's not too late to start making those thoughts a reality, and never be discouraged. To you all, I would like to remind you that we are here by the Grace of God and without the Spirit of God we are nothing and can do nothing. I am thankful to the Father for an experience such as this to teach me of the love of God while using each experience to develop the fruit of the Spirit in me.

Therefore, I say, do not resist and grieve the Holy Spirit. Get to know Him, yield to Him, abide in His word and do as He instructs and your life will never be the same! You will have peace and success that the world cannot create or destruct. May the good Lord be with you and your own, may He bless and increase you in all you do for His sake. Once again, thank you and God bless you...

Acknowledgements

I would first like to thank the Almighty God for a life of purpose that has been granted me by the works of the Spirit through Jesus Christ. There was much I thought I knew but then realized that I knew almost nothing about, including God Himself! However, during this journey, the Lord's grace was abundant, more evident and palpable to me and in my life. Although there is more for me to learn, I'm grateful for what I know now and how far He's brought me. It was neither by the power or might of any man, but only by the Spirit of the Lord of Hosts.

I have been so blessed to have many men and women of God used to push and uphold me to get me here! Pastors and Mrs. Johnson, Brodie-Mends and Gasu; my very own Pastor Michael and Auntie Mina Ananncy, Pastor and Mrs Tokoli; Pastors John and Grace Orhion, Pastor Eugene and Sister Abena Foli, the one and only Pastor Kobby!!, my Pastor Dr. Ba (Keturah), and The very esteemed Rev Ken Oyakhilome. What a privilege and honor to have been under your teaching and guidance, as well as to have your prayers, love and support over the years. I'm eternally GRATEFUL! And I know the Lord God will reward you for your labor of love.

To my family – Rev Prof B A and Alice Ntreh, my own Daddy and Mommy, as well as my one and only AK-Wele!, the reverends daughter lol – the amount of love and prayers and calls and everything you've lost and done on my behalf is overwhelming! I'm grateful to God for giving me you, I wouldn't trade you EVER! Ahda! (Yehoda), the numerous times you've been ignored but you remained supportive, I'm grateful and thankful! I won't forget your show of love and support that helped to get me here!

A very big thank you to Dr. Elena I Zgurskaya! Thank you for saying yes to me, I'd pick you again if I had to repeat. To the professors who have served on my advisory committee – Drs. Rybenkov, Cichewicz, Rice, Dunn, Zhang, Klebba, Houser, and Li – Thank you for your time, attention, feedback! Thank you to Drs. Sims, Najar, Richter-Addo and West for the advice and support, though you were not in my committee I learned from you also. My very own Elena!!! (Tikhonova), I'm grateful to have had the time and privilege of learning the basics from you! And even when you left, you came to my rescue, as needed; THANK YOU!!! To the friends who became family, in the lab and at TAMU, thank you ALL for the love and support, prayers and fun times; you helped make this journey memorable!!

My personal persons… Pastor Ba, again I say THANK YOU!!! The amounts to love and support from you, from the very beginning to the very end! You've been wonderful! I'm grateful to have shared this journey, no matter the turbulence along the way. And to share in the crowning of this journey! Lol I thank God for answered prayers… To God's great and invincible defender, my one and only – really one of the best additions to my friends, family and pastor lists – Alex, you've been a blessing to me! Words can't express all I'd like to say but I know thank you would be a good start. I love you both so so much!! Soooo much! Thank you for everything...

So may the God of love, mercy and grace, bless and multiple each and every single one of you. May you be equipped for all you have to do. And may you know and believe in God – the Father, Son, and Holy Spirit – holding fast to His Word till His return. God's will be done in your lives, in Jesus' name, Amen.

I LOOOOOVE YOU!!!

Table of Contents

Dedication 4

Acknowledgements iv

List of Figures xi

Abstract xiv

I. Introduction 1

I.1 Multidrug Efflux 2

I.1.1 Membrane Fusion Proteins (MFPs) 4

I.1.2 Outer Membrane Proteins (OMPs) 6

I.1.3 Inner Membrane Proteins (IMPs) 9

I.2 Assembly and Mechanism of RND Pumps 12

I.3 Aims and Goals of Dissertation 17

II. Materials and Experimental Procedures 19

II.1 DNA Manipulations 19

II.1.1 List of Strains 19

II.1.2 List of Plasmids 20

II.1.3 List of Primers 23

II.1.4 Site-Directed Mutagenesis 24

II.1.5 OpmH Cloning 24

II.2 Minimal Inhibitory Concentration (MIC) Determinations 25

II.3 Protein Purification 25

II.3.1 AcrA 25

II.3.2 AcrB 27

II.3.3 TolC 28
II.3.4 TriA, TriB, TriC, TriABC, and TriAxBC and Variants 29
II.3.5 OpmH 30
II.4 Fluorophore Uptake Assays 31
II.5 Spontaneous Sulfide Crosslinking 32
II.6 Azithromycin Spot Assay 33
II.7 Protein Labeling with NANOGOLD® 33
II.8 Negative Staining Electron Microscopy (EM) 34
II.8.1 Sample Preparation and Image Acquisition. 34
II.8.2 EM Data Processing and Image Analysis. 35
II.9 Proteolysis 35
II.10 Pyrene Maleimide Labeling 36
II.11 Fluorescence Spectroscopy 37
II.12 Surface Plasmon Resonance 37
II.12.1 Thiol Coupling 37
II.12.2 Immobilization 38
II.12.3 Data Collection and Normalization 39
Chapter 1. Non-Equivalent Roles of TriA and TriB in Efflux 40
1.1 TriABC and TriAxBC are Expressed and Functional in *E. coli* GKCW101 (Δ9FhuA) 41
1.2 Nile Red is the Best Probe for Kinetic Studies 43
1.3 Optimization of Cell Densities for Nile Red Uptake Assays 44
1.4 There is No Competition Between Nile Red and Triclosan 46

1.5 TriA and TriB Have Non-Equivalent Roles in TriABC Functionality 47
1.6 TriA, but not TriB, is Essential for TriABC Efflux of Nile Red 48
1.7 Association with TolC Changes TriA Conformation 50
Chapter 2. Investigation of TriAB Interactions and Mechanism of Opening the Channel Protein 58
2.1 OpmH is an Essential Protein of Efflux-Deficient *P. aeruginosa* 58
2.2 OpmH Cysteine Variants Are Functional and Assemble into Complexes with TriABC 61
2.3 TriA and TriB Cysteine Variants Are Expressed and Functional 64
2.4 $OpmH_{E173C}$, $OpmH_{K182C}$, and $OpmH_{I392C}$ Form Disulfide Bonds with Both TriA and TriB 66
2.5 TriB Opens the OpmH Channel Aperture 70
Chapter 3. Structural Analysis of the TriABC Complex 75
3.1 The Open Conformation of TriAxBC Complex 75
3.1.1 TriABC Form a Stable Complex 75
3.1.2 RND TriC is Dynamic in Solution 76
3.1.3 TriA and TriB Assume Different Conformations in Solution. 76
3.2 $TriAxB_{R133C}C$ Maintains Wildtype Protein Conformations 78
Chapter 4. Assessment of AcrA-TolC Interactions by Fluorescence Spectroscopy 80
4.1 Development of Fluorescence Assay 80
4.1.1 Expression, Functionality, and Purification 84
4.1.2 Fluorescence Assays with Free Pyrene Maleimide 84
4.1.3 Pyrene Maleimide Labeling and Fluorescence Assays 85

4.1.4 Time Course Analysis of AcrA-TolC Interactions 88
4.2 Optimizing Fluorescence Assay for AcrA-TolC Interaction Studies 88
4.2.1 Stabilizing Protein-Protein Interactions by pH and Mg^{2+} 88
4.2.2 Reselection of Amino Acids 91
4.2.3 Inducing Disulfide Bonding 91
Chapter 5. Surface Plasmon Resonance Studies of EPI Interactions with Transporter Protein AcrB 95
5.1 Immobilization of AcrB and $AcrB_{D408A}$ and Binding Assay Development on the SensíQ® Pioneer 98
5.2 Immobilized AcrB and Its Non-Functional Mutant Bind EPIs. 103
5.3 Binding Affinities of EPIs Are Dependent on the Amount of AcrB Present. .. 104
5.4 Immobilization of AcrA, AcrB and TolC on the Biacore 3000. 106
5.5 Basilea EPIs Bind More Specifically to AcrB than to AcrA or TolC 107
5.6 AcrB-Inhibitor Interactions Model a Bivalent Analyte or Two-State Model .. 112
III. Conclusions 116
References 118

List of Tables

Table 1.0.1 Antimicrobial Susceptibility of *E. coli* GKCW101 (Δ9FhuA) Producing Plasmid Expressed TriAxBC Variants 42

Table 2.0.1 Arabinose-Dependent Antimicrobial Susceptibility of *P. aeruginosa* JWW9 (PAO1116 attTn7::ParaBAD-opmH$_{His}$) Producing Indicated Tri Complexes. 61

Table 2.0.2 Antimicrobial Susceptibility of JWW9 (OpmH$_{His}$) Cysteine Variants Containing the Plasmid Encoded TriABC 62

Table 2.0.3 TriAxBC Cysteine-Containing Mutants Are Functional..... 65

Table 2.0.4 MICs of Select OpmH Cysteine Mutants Co-Expressed with TriAxBC Cysteine Variants..... 67

Table 2.0.5 OpmH Cysteines Show Preference for TriABC Bonding..... 68

Table 4.0.1 Antimicrobial Susceptibility of *E. coli* ZK769 Cells Expressing TolC and YFRE. 82

Table 5.0.1 Basilea Pharmaceutica Efflux Inhibitors and Properties. 96

Table 5.0.2 Kinetic Parameters of Basilea EPI Binding to AcrB and Mutant 103

Table 5.0.3 AcrB-Dependent Substrate Binding Affinities..... 106

Table 5.0.4 Kinetic Parameters of AcrB-Inhibitor Interactions……..….113

Table 5.0.5 Kinetic Parameters of B3347 from Local Fitting……..…. 114

List of Figures

Figure I.0.1 Mechanisms of Bacterial Resistance 2

Figure I.0.2 Structure and Folding of Membrane Fusion Proteins (MFPs)..... 4

Figure I.0.3 Crystal Structure of the Outer Membrane Factor TolC 8

Figure I.0.4 *E. coli* RND Transporter, AcrB 11

Figure I.0.5 Docking of CusC to CusBA 14

Figure I.0.6 Proposed Models of RND Pump Assembly 15

Figure I.0.7 Proposed Mechanism of RND Transporters..... 16

Figure 1.0.1 Protein Structures of TriA and TriB 40

Figure 1.0.2 Expression Analysis of TriABC and TriAxBC..... 41

Figure 1.0.3 Fluorescence Uptake Analysis of NPN..... 45

Figure 1.0.4 Fluorescence Uptake Analysis of Hoescht-33342 45

Figure 1.0.5 Fluorescence Uptake Analysis of Nile Red 45

Figure 1.0.6 Calibrating Nile Red Uptake Assay on the TECAN Spark 10M..... 46

Figure 1.0.7 Triclosan and Nile Red Do Not Compete for Uptake..... 47

Figure 1.0.8 Nile Red Fluorescence and Rates of Uptake..... 48

Figure 1.0.9 TriAB, TriABC, TriAxBC Expression in *P. aeruginosa* GKCW122 50

Figure 1.0.10 TriAB, ABC, and AxBC Proteolysis in *P. aeruginosa* GKCW122 51

Figure 1.0.11 Proteolytic Profiles of TriAB..... 53

Figure 1.0.12 Proteolytic Profiles of TriAB in Aspartic Acid Variants of the Coiled-Coil Domain 55

Figure 1.0.13 Proteolytic Profiles of TriAB in Cysteine Variants of the Membrane Proximal Domain..... 56

Figure 2.0.1 TolC Crystal Structure 59

Figure 2.0.2 Arabinose Concentration-Dependent OpmH Expression 60

Figure 2.0.3 OpmH Cysteine Variants Assemble in Complex with TriABC 63

Figure 2.0.5 TriA and TriB Cysteine Mutants 64

Figure 2.0.4 TriA and TriB Cysteine Variants Are Expressed..... 64

Figure 2.0.6 TriAxBC and OpmH Cysteine Mutants Form Spontaneous Disulfide..... 66

Figure 2.0.7 OpmH Cysteine Variants Form Bonds with Both TriA and TriB 67

Figure 2.0.8 Quantified of TriAxB-OpmH Disulfide Bonding..... 68

Figure 2.0.9 TriAB-OpmH Assembly Models..... 69

Figure 2.0.10 Closed and Open Conformations of the TolC Periplasmic Aperture..... 70

Figure 2.0.11 TriB is Essential for Opening the OpmH Channel Protein..... 71

Figure 2.0.12 Proposed Mechanism of OMP Aperture Opening 73

Figure 3.0.1 TriAxBC-OpmH Protein Purification..... 75

Figure 3.0.2 Homotrimeric TriC Protein Structure 76

Figure 3.0.3 TriABC Structure Predictions..... 77

Figure 3.0.4 Gold-Labeled TriAxBC Has Same Conformation as the Wildtype..... 78

Figure 4.0.1 AcrA and TolC Protein Structures..... 81

Figure 4.0.2 AcrA and TolC Cysteine Mutant Expression and Protein Purification 83

Figure 4.0.3 Fluorescence Spectrum of Pyrene Maleimide 85

Figure 4.0.4 Alternate Labeling of $AcrA_{D149C}$ with Pyrene Maleimide 86

Figure 4.0.5 Concentration-Dependent Fluorescence Spectrum of PM Labeled $AcrA_{D149C}$, $TolC_{K383C}$, and $YFRE_{K383C}$. 88

Figure 4.0.6 $AcrA_{D149C}$-$TolC_{K383C}$ Do Not Interact at pH 6.0..... 89

Figure 4.0.7 Mg^{2+} Stabilizes $AcrA_{D149C}$-$TolC_{K383C}$ Interactions at pH 7.5 90

Figure 4.0.8 TolC/$YFRE_{K383C}$ Does Not Form Spontaneous Disulfides..... 92

Figure 4.0.9 $AcrA_{D149C}$-TolC/$YFRE_{K383C}$ Interactions Cannot Be Stabilized by Cu^{2+} .. 93

Figure 5.0.1 Phenylalanine Arginyl β-Napthylamide (PAβN)..... 95

Figure 5.0.2 Surface Plasmon Resonance (SPR)..... 96

Figure 5.0.3 SPR Chip Surface Chemistry for Protein Immobilization 97

Figure 5.0.4 AcrA, AcrB, and TolC Cysteine Variants for SPR Immobilization 98

Figure 5.0.5 Expression and Purification of AcrA, AcrB and TolC Mutants 99

Figure 5.0.6 Immobilization Sensogram of AcrB and mutant using Thiol Coupling .. 100

Figure 5.0.7 AcrB and Mutant Bind AcrA with Similar Affinities..... 101

Figure 5.0.8 Binding Curves and Scatchard Plots of Basilea Inhibitors with AcrB and AcrBD408A..... 102

Figure 5.0.9 Scatchard Representation of AcrB-Dependent Substrate Binding 105

Figure 5.0.10 Inhibitors Bind AcrA 109

Figure 5.0.11 Inhibitors Bind AcrB..... 110

Figure 5.0.12 Inhibitors Bind TolC 111

Figure 5.0.13 Global and Local Fitting of B3347 112

Abstract

Since the discovery of antibiotics, an ongoing race commenced between society's ability to develop drugs and resistant bacteria. The combat has led to many drug discoveries, but it has also led to different mechanisms of the pathogens to evade cell death. One major means of bacterial resistance is the association of membrane proteins to expel substrates from within the cell and out into the extracellular space. Some protein complexes are able to oust various drugs irrespective of structure or function of the antimicrobial; these are the multidrug resistance (MDR) efflux pumps. In the Gram-negative bacteria, these complexes are made up of an inner membrane transport protein (IMP), a periplasmic adapter protein (PAP) also commonly known as the membrane fusion protein (MFP), and an outer membrane protein (OMP). This assembled conduit acts as a canal to channel substrates from within the cytoplasm – substrates are repositioned outside the nearly impenetrable outer barrier.

Escherichia coli AcrAB-TolC is a constitutively expressed MDR pump. As one of the most studied systems, all three proteins have been crystalized, allowing for better understanding of the protein structures and properties. Many biochemical and structural experiments have aided predictions about protein-protein interactions and mechanisms of function of this protein complex. However, the homo-identity of all proteins in complex limits the isolation of roles and mechanistic characterization. The recently discovered TriABC-OpmH of *Pseudomonas aeruginosa* uniquely expresses two MFPs (TriA and TriB) and serves as a model system to study the assembly of efflux pumps and the function of MFPs in complex. In this study, we used the transporter protein AcrB to characterize kinetic parameters of efflux pump inhibitors (EPIs) provided by

Basilea Pharmaceutica. Next, we used the TriABC complex as the means of studying the MFP-OMP amino acid interfaces. We investigated the role and assembly of TriA/B with the partnering OMP. We confirmed that MFPs stabilize interactions with the outer membrane channel protein, and we also assigned MFPs the role of opening the channel protein. Results isolated the role of each MFP within the functional dimeric complex. Additionally, we present low-resolution structures of TriABC showing different conformations of the TriAB MFPs. *In vivo* proteolysis experiments validate the structural findings, while presenting an OMP-dependent conformational change within one MFP. Together, this study provides new insight into the mechanism of MDR efflux complex, inspiring innovative drug targets and new drug designs to reciprocate and combat resistance of bacterial cells.

I. Introduction

In recent years, a major threat to public health has stemmed from bacterial infections. Many antimicrobials have been discovered or synthetized over the decades to address infections caused by Gram-negative and Gram-positive bacteria alike. These therapeutics are categorized into different classes, grouping them by the target of action within the cell [10]. Despite the variety of drugs and broad spectrum activities of some, they are proving futile in the treatment of infections due to the cell's ability to acquire resistance to the treatments.

Bacterial cells have gained resistance to drugs by intrinsically mutating the drug binding site; degrading or modifying the antibiotic when it enters the cell; or preventing the entrance or diffusion of drugs across the cell wall [5, 10, 11]. If any drug should bypass these mechanisms of resistance, there are proteins within the cell membranes that allow extrusion of substrates across the inner and outer membranes (Figure I.0.1). Such resistance has led to increased dosages, as well as the use of drug cocktails to enable effective treatment of infections. However, cells continue to gain resistance to most administered therapeutics, irrespective of the structural or functional differences. Multidrug resistance (MDR) bacteria include Gram-negative pathogens like *Pseudomonas aeruginosa* and *Klebsiella pneumoniae, etc.* It is imperative that new drugs are designed that have different targets and binding sites, more than has been done before, to help combat infections by these microbes.

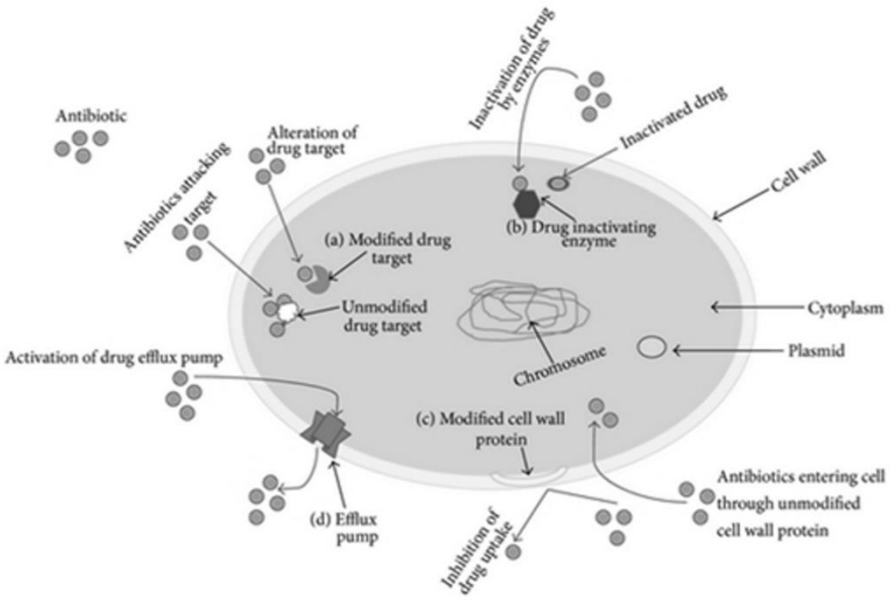

Figure I.0.1 Mechanisms of Bacterial Resistance
A. Cells modify intended target of the drug substrate, evading cell death. **B.** Intrinsic enzymes are produces to alter the drug. Drug may either be modified or degraded. **C.** Bacteria can change the cell wall composition to reduce diffusion or transport across the outer shell. **D.** Intrinsically expressed proteins of the cell membrane (and cell wall, in Gram-negative bacteria) actively expel drug substrate out of the cell and into the extracellular space.[5]

I.1 Multidrug Efflux

One major means of resistance is the use of multidrug efflux (MDE) pumps. Granted the components of MDEs are the same – an outer membrane channel protein, an inner membrane transporter protein, and periplasmic adapter proteins – the substrate specificities vary. These complexes are also distinguished by source of energy for pump functionality. ATP Binding Cassette (ABC) type transporters use the hydrolysis of ATP molecules as the energy needed for activation [10]. Secondary transporters of the Major Facilitator Superfamily (MFS) [12], Small Multidrug Resistance (SMR) [13], Multidrug and Toxic Compounds Extrusion (MATE) [14], Resistance Nodulation Cell Division (RND) [15], and the recently discovered Proteobacterial Antimicrobial

Compound Efflux (PACE) [16] families use either the transport of ions such as Na^+ or the proton motive force (PMF) to allow transport across the cell's membranes.

MDEs are composed of a transporter protein that is located in the inner membrane (IMP) – this uses energy to transport substrates out of the periplasm and cytoplasm; an outer membrane protein (OMP) acts as the channel through which molecules are expelled back outside the cell; and a flexible periplasmic protein (MFP) helps anchor and bridge the two proteins of either membrane [7, 10, 17]. In Gram-positive bacteria, where there is no need for an OMP, the inner membrane transporter allows substrates to cross the peptidoglycan layer and out into the extracellular space. In some instances MFPs are present, as would be seen in Gram-negative bacteria [7].

Pseudomonas aeruginosa is an opportunistic, Gram-negative pathogen that is notorious for its resistance to most antiseptics. *Pseudomonas aeruginosa* has more than 10 RND pumps [18], allowing for the expulsion of various drug substrates of varying classes.

I.1.1 Membrane Fusion Proteins (MFPs)

The periplasmic adapter protein is a sickle-shaped protein. Due to lipid-

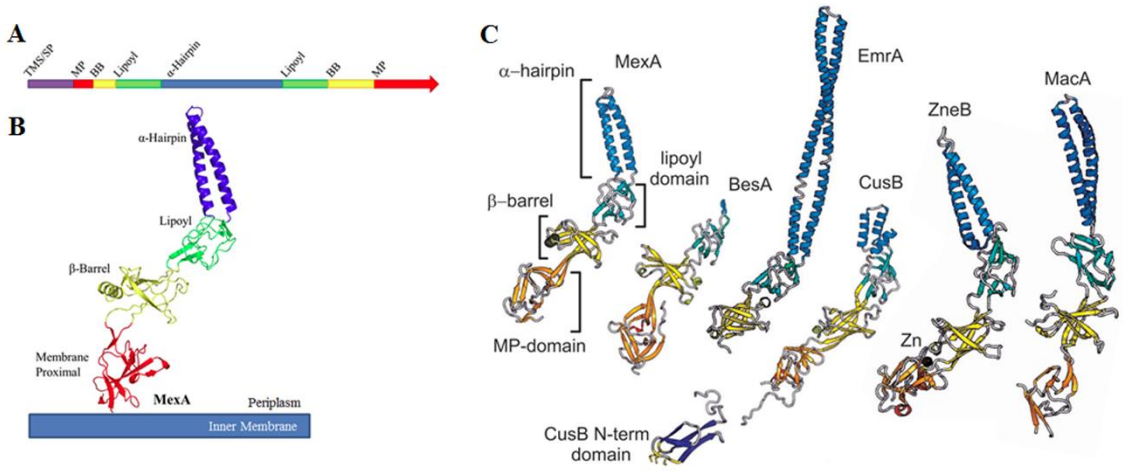

Figure I.0.2 Structure and Folding of Membrane Fusion Proteins (MFPs)
A. Linear representation of the membrane fusion proteins showing the distribution of the four domains (purple – transmembrane segment/signal peptide, red – membrane proximal domain, yellow – β-barrel domain, green – lipoyl domain, and blue – α-helical hairpin domain) in the N- and C-terminus. **B.** Crystal structure of MexA (PDB code: 2V4D). The domains of the protein are highlighted in colors corresponding to the linear diagram. **C.** Crystal structures of various MFPs depicting the variation in protein structures, especially at the α-helical domain. (Adopted from [7] and modified [9])

modification of the N-terminus cysteine or a transmembrane segment, MFPs are anchored to the inner membrane [9]. In studies where the N-terminus cysteine is replaced or truncated, the protein is more mobile [9, 19, 20]. MFPs fold in symmetry, where all four domains are formed by amino acid residues located in the N- and c-terminal halves of the protein sequence (Figure I.0.2A). In the middle of the two-fold symmetry is the α-helical domain, followed by the lipoyl and β-barrel domains; lastly, the protein folds into the membrane proximal domain (Figure I.0.2B). The anti-parallel helices of the α-helical domain has been found to vary in length from protein to protein, dependent on the species (Figure I.0.2C). The α-helical, coiled coil domain has been shown to assemble and align along the surfaces of OMPs to allow a stabilizing and functional

complex [21]. Transitioning into the lipoyl domain, the protein folds are made of β-strands. This domain, though its functional role has yet to be elucidated, is thought to also contribute to the stabilizing of an MFP-OMP complex. As the name implies, the β-barrel is made up of anti-parallel β-strands, but it also includes one α-helix. The fourth domain, the membrane proximal (MP) domain, follows the design of the previous domain. Made up of β-strands and one α-helix, the MP domain is the most flexible region due to the nature of the linker region between the two domains. The extent of this flexibility is evident in available crystal structures, where some lack the fourth domain [22].

Studies with various MFPs, including *E. coli* AcrA, have shed light on the role of the domains as well as interactions needed within a functional complex. Crosslinking studies mapped amino acid sites on MexA and AcrA to find binding sites to their partnering IMP and OMP [23, 24]. These studies showed that the β-barrel and MP domains interact with the IMP while the α-helices of MFPs interact with the OMP. SPR studies determined kinetic parameters of AcrA, EmrA, and MacA interactions with the universal channel, TolC [25]. Along with others studies, findings from Tikhonova *et al.* (2009) present the importance of the oligomeric state of MFPs within complex. The existing evidence shows that MFPs function in a trimer of dimers, forming hexameric barrels surrounding the OMF. Despite all the findings, there is much that remains to be learned about these flexible periplasmic proteins.

I.1.2 Outer Membrane Proteins (OMPs)

Localized in the bacterial cell wall, channel proteins of efflux pumps have been characterized as the Outer Membrane Factor (OMF) family [26]. The first of its family to be crystalized, *E. coli* TolC revealed a unique protein structure [27]. Since then, homologs have been found to model this protein folding [21, 28-30]. The specificity of an OMF to a transporter-MFP pair is based on interactions with the MFP. However, some OMFs, like the *E. coli* TolC protein, are promiscuous – TolC has been shown to assemble in many efflux pump complexes [31-33]. Thus, the basis of OMF recognition and specificity is still unclear.

TolC extends from the extracellular space, spans the outer membrane and continues well into the periplasmic space. This 140 Å long, channel-like protein is made up of a 12-stranded β-barrel and α-helical domain, and a mixed α/β-domain (also referred to as the equatorial domain) (Figure I.0.3A). Like other OMPs, the TolC β-barrel is a trimer embedded in the membrane; however, TolC exists as a homotrimer – each protomer contributes four β-strands. The right-handed β-strands of the barrel render TolC wide open while the lack of inward-folded extracellular loops makes the protein accessible to large volumes of solvent (Figure I.0.3C). At the periplasmic ends of the β-strands, proline-containing linkers initiate the change of orientation of the coil-coiled α-domain to make them left-twisted helices. The α-domain is made up of two long helices that span the nearly 100 Å into the periplasm and four shorter helices that stack up to make two long, pseudo-continuous helices that also span the length of the domain. At the interface of the short helices are strands and helices (of α/β structure mixture) that attain their fold via hydrogen bonding and van der Waals interactions with

side chains (Figure I.0.3B). Although there exists pseudosymmetry (in the α-domain) as two sets of coiled coils share similar sequences and interhelical interactions, one pair is more angularly inclined – 20° – towards the core of the protein. The dense packing of the three curved sets of coiled coils has been speculated to be the reason for the periplasmic opening of TolC exhibiting a "closed" conformation (Figure I.0.3D) [27, 34-36]. The periplasmic aperture of OMFs differs from protein to protein. Some are in a closed conformation, like in TolC and CusC, but others still are left ajar, as is found in the MtrE protein structure [30]. The closed conformation of the TolC aperture is held closed by salt bridge interactions between the residues Thr 152, Asp 153, Tyr 362, and Arg 367, as well as a second bottleneck composed of a network of aspartic acid residues (Asp 374) of the three protomers [37]. These closures prevent leakage across the protein channel. Regardless, the cavity of TolC is one of the largest known protein structures,

holding about 43000 Å^3 of solvent; it is capable of allowing passage of particles as large as 160 kDa.

OMFs get help from the assembled trimer of dimeric MFPs around the channel protein to prevent leakage of substrates into the periplasm or diffusion from the external media [7, 9]. MFPs are also key in the opening of the outer membrane channel, by the disruption of salt bridges[9]. However, the mechanism of opening is dependent on the transporter protein, which relays conformational changes to the MFP in order to open the OMF. Molecular details of the mechanism of channel opening is yet to be elucidated.

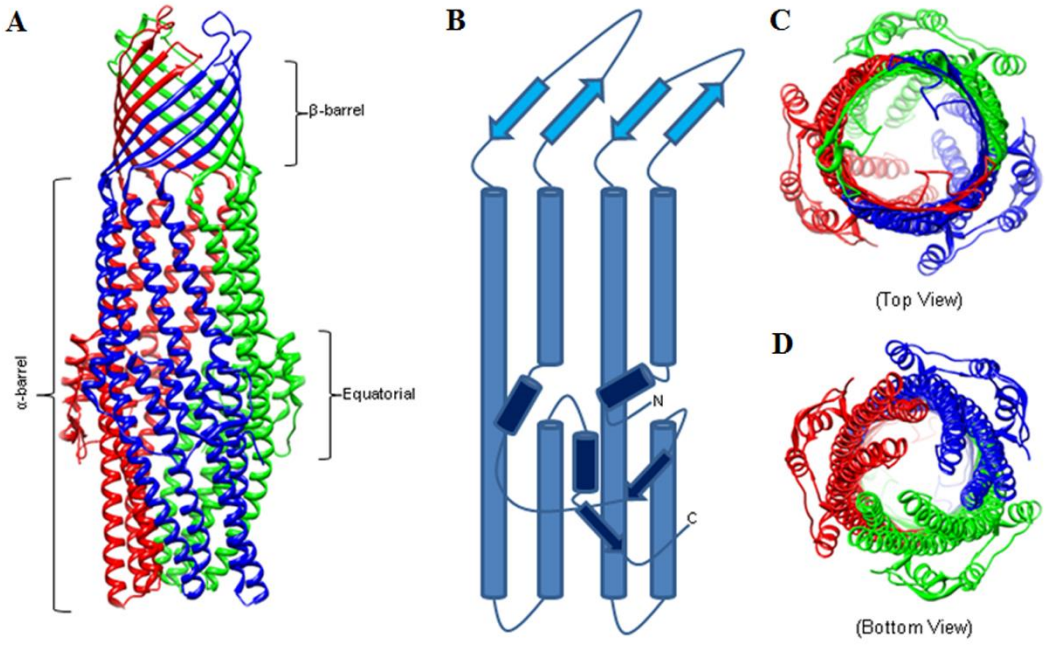

Figure I.0.3 Crystal Structure of the Outer Membrane Factor TolC
A. The homotrimeric, universal outer membrane channel (PDB code: 1EK9). **B.** Blueprint diagram of the architecture of OMFs. (Dark blue – the equatorial region, blue – α-helices of the protruding barrel domain, and light blue – β-strands of the barrel spanning the cell wall) **C.** The top and **D.** bottom views of TolC showing the open and wide cavity, that's "closed" at the periplasmic end. [7]

In addition to drug substrates, OMPs are also involved in the secretion of metals, as well as ions and other proteins across the outer membrane barrier. One such case is

the OMF CusC, together with the CusAB MFP and transporter pair in *E. coli*, which has been shown to export copper (I) and silver (I). These heavy metal ions bind and are transported to CusB by the fourth system component CusF [29]. Also serving as the exit channel for toxins and other proteins, OMFs have been well characterized by protein sequence, structure and function. However, it still remains to characterize the sequence of steps involved in the assembly of OMPs with their transporter-MFP counterparts. The interactions that allow for the dilation and opening of periplasmic aperture is yet to be understood. Neither have the interactions of the OMP-MFP or OMP-IMP interfaces that participate in a functional complex been fully elucidated.

I.1.3 Inner Membrane Proteins (IMPs)

Inner membrane transporters (IMPs) are categorized into families of proteins, as discussed above. Proteins of the RND superfamily have been identified to expel ions, dyes, antimicrobials, etc. A staple RND transporter is *E. coli* AcrB. AcrB is a proton antiporter used by cells to extrude small molecules out of the cell. Since it was first crystallized, there have been over 25 different structures presented [3]. As is common with MDE proteins, AcrB structure is one of symmetry. The N- and C-terminal ends contain the three domains of the protein – transmembrane, pore, and OMP docking domains (Figure I.0.4A). The mushroom-shaped AcrB is made up of 12 transmembrane (TM) α-helices. Stemming from TM1 and 2, then TM7 and 8, is a collection of β-strands and α-helices to make the pore and docking domains located in the periplasm[2]. Extending past the inner membrane into the cytoplasm and ~70Å into the periplasm, the full length of this protein is expected to be ~120Å. AcrB assembles

as a homotrimer, with the monomers linked by a protruding loop from a neighboring docking domain (Figure I.0.4B) [2]. Despite this, the protein does not function in a symmetric manner. This transporter protein has two - the distal and proximal - binding pockets within each of its three protomers. Each monomer has been shown to have different conformations – open, loose, or tight - as they relay a proton across the transmembrane domain and simultaneously translocate substrate from the periplasmic space outside the cell [38].

Biochemical and structural studies have shown that AcrB function asymmetrically within the cell [3, 39, 40]. The loose, open and tight conformations of the AcrB protomers describe the state of the binding pockets, within the pore domain, and the relative state of interaction with the substrate. A loose binding site is open and ready to capture substrate. Once substrate binds, the protein assumes the tight conformation and secures the hold on the molecule until expulsion through the inner

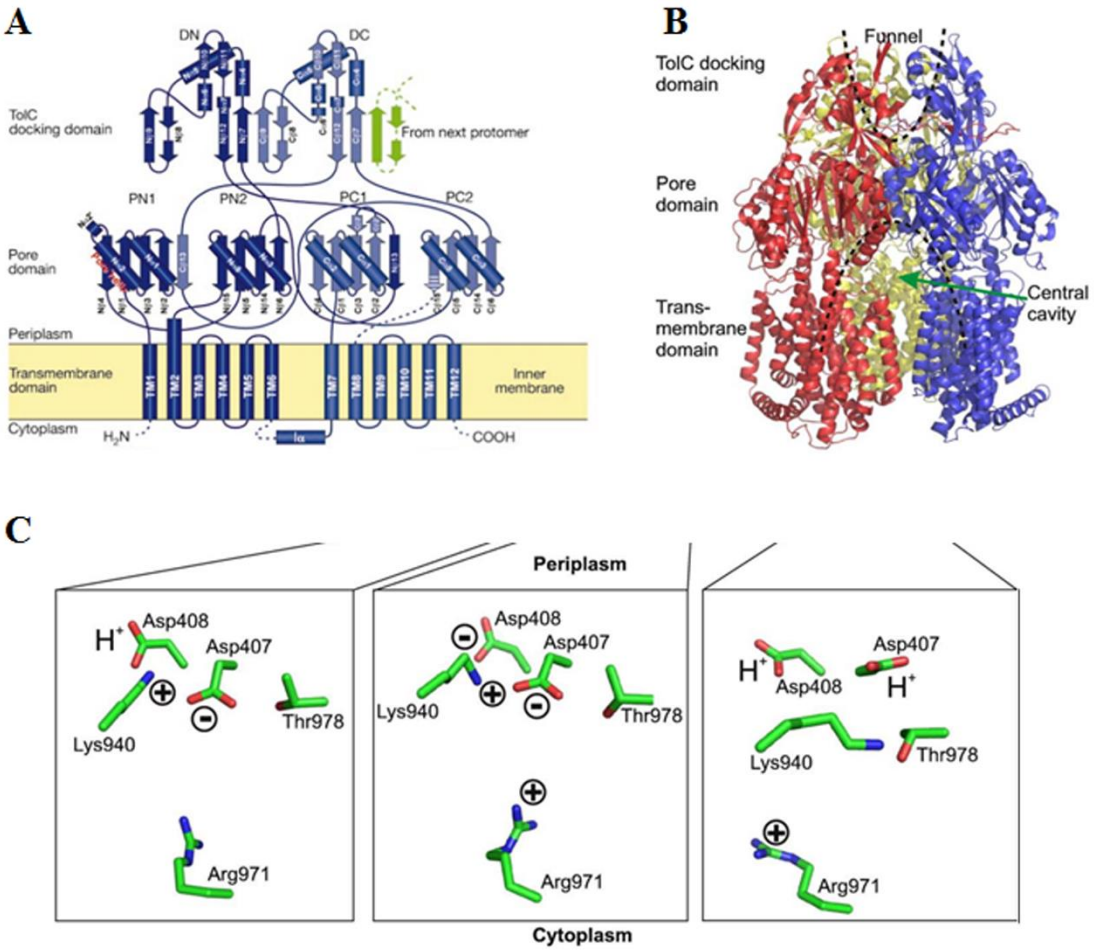

Figure I.0.4 *E. coli* RND Transporter, AcrB
A. Topology of the AcrB, mapping the α-helical helices and β-strands of the transmembrane, pore, and docking domains. **B**. Resolved crystal structure of the homotrimeric RND transporter (PDB code: 2HRT). **C**. Close-up analysis of the conformational changes within the transmembrane domain, as a proton is relayed across the membrane. Asp 407, Asp 408, and Lys 940 are the key residues within the domain as the protein transitions between the loose, tight and open states. (Adapted and modified from [2, 3])

pore and out the outer channel. The protein is then in the open transition and relaxes to take on the loose form again [3]. Each protomer of the protein undergoes these changes. The shape of the binding pockets is related to the conformational changes occurring in the transmembrane helices as the drug/proton antiport catalysis occurs. Asp 407 and 408 of TM4, and Lys 940 of TM10 have been identified as the key amino acid residues involved in the proton relay across the inner membrane (Figure I.0.4C)[3]. Despite the observations made over the years, the roles of RND transporters in the recruiting of its binding partners, especially the corresponding OMP, still remain unclear. This is also true of the additional roles within the tripartite complex such as the determination of substrate specificity and effects of conformational changes on the complex function.

I.2 Assembly and Mechanism of RND Pumps

In light of the structural knowledge about each component of the efflux pumps, various studies have sought to highlight bipartite interactions, as well as the full complex assembly and functionality. Co-crystallization with its partnering membrane fusion protein, the CusAB complex, presents information about the RND-MFP complex as would be present *in vivo*. The CusA transporter is located in the inner membrane, having the same architecture as AcrB [1, 41]. CusA has 12 transmembrane helices and a large periplasmic domain – the pore and docking domains – stemming from between TM1 and 2, and TM7 and 8. The CusB adapter protein also models most other membrane fusion proteins. Consisting of the four major domains – the membrane proximal, β-barrel, lipoyl, and α-helical hairpin domains – CusB differs in the α-hairpin domain, which is made up of three, short helices [41]. In this assembled model, the

membrane proximal domain and parts of the β-barrel domain are shown to cap the pore and docking domains of CusA. The third component of the tripartite complex, CusC, was recently crystallized and found to resemble the TolC structure [29]. 130 Å long, CusC is made up of a 12 stranded β-barrel and long α-helical domain and an equatorial domain. Docking the CusC [1] channel protein, two modes of assembly were proposed to illustrate the different states during the efflux of heavy metals (Figure I.0.5). In the first model, the end of the CusC α-barrel interacts with the α-helices of CusB. The second model, due to the large hexameric pore of CusB, presents CusC docked on top of CusA with the lipoyl domain of CusB at the CusA-CusC interface. The rest of the CusC α-barrel is wrapped by the CusB α-hairpin domain.

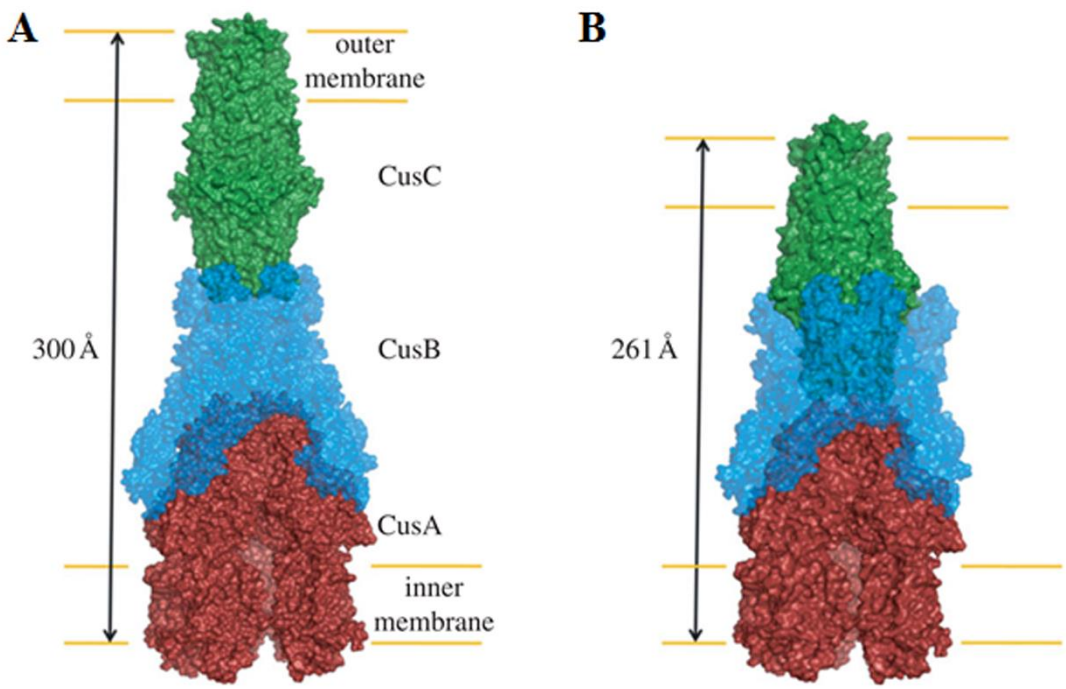

Figure I.0.5 Docking of CusC to CusBA
A. The α-helices of CusC docks on top of CusB, interacting at the distal ends. Coupled with the docked CusBA complex, this forms a conduit from the periplasm and out the bacterial cell. **B.** Based on the size of the CusB hexameric pore, the CusC channel protein can be enveloped within it. This allows for direct CusAC interactions at the transporter's docking domain. (Adapted from [1])

All three components of the AcrAB-TolC complex have been resolved [2, 22, 27], though there have not been any combinations of the proteins that have been co-crystallized. However, there have been many studies that present docked models, as the proteins would assemble *in vivo* [7, 9, 32, 42-45]. Based on the structural similarities of the α-helical domains of OMPs and MFPs, as is found in TolC and AcrA, some believe that there is a complete overlap of the proteins at this region [2, 23, 40, 45]. This is the favored docking model which supports the hypothesis that the TolC periplasmic end interacts directly with the top of the TolC docking domain of AcrB [8]. Another model of the tripartite assembly differs from the former in that the coiled coils of TolC and AcrA partially overlap [42]. In this model, direct AcrB-TolC interactions are broken, having no

direct contact. Instead, they are bridged together by the fusion protein. There is yet another model that suggests a tip-to-tip interaction of the OMP-MFP at the distal loops [46, 47]. In these models, we see a variability of the docking of the MFP to the transporter protein (Figure I.0.6). Some models present the lipoyl and β-barrel domains of the MFP as seated on the docking domain of the RND transporter, while the membrane proximal domain interacts with the pore domains. Other models present the membrane proximal domain aligned with the docking domains. All these models beg the question of the

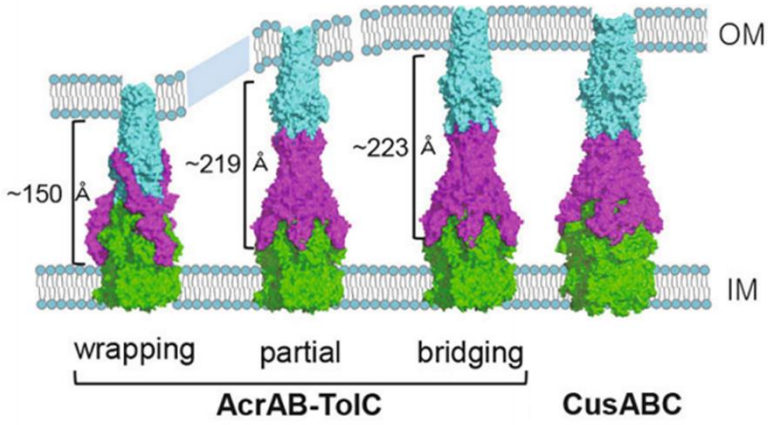

Figure I.0.6 Proposed Models of RND Pump Assembly
The OMF (cyan), transporter protein (green), and membrane fusion proteins (magenta) of the AcrAB-TolC tripartite complex, used to depict the different models of protein assembly. In the wrapping model, the structurally similar α-helical domains of TolC and AcrA are fully aligned. However, in the partial model, only regions below the equatorial domain align, one to another. In this model, the membrane proximal domain is located at the docking domain, rather than the pore domain. The bridging model, as observed in the CusABC complex, involves the tip-to-tip interactions of the OMP α-barrel and MFPs α-hairpins. Each model presents different measurements of the periplasmic space. (Modified [8])

flexibility and length between the membranes of the bacterial cell, seeing as each model presents different measurements (Figure I.0.6). Another point of controversy concerning assembled efflux pumps pertains to the stoichiometry of each component within the complex. Early research proposed and favored 3 RND:3 MFP:3 OMP ratios [2]. However, in subsequent research using crystallography and chimeric constructs, it has

been proven that a 3:6:3 ratio is the more plausible composition of RND efflux pumps within the bacterial cell [33, 41, 44].

Studies of complexes such as the *P. aeruginosa* MexAB-OprM or the *E. coli* AcrAB-TolC, MacAB-TolC, and the recently resolved CusABC systems have helped shed much light on the mechanism of RND efflux pumps (Figure I.0.7). The co-crystallization of CusBA introduces a stable, preassembled transporter-MFP complex. *In vivo*, this bipartite complex is assembled and ready to engage the outer membrane protein. Since *in vivo* proteolysis showed that AcrA undergoes conformational changes in the presence of TolC [48], we expect a change in the MFP structure during the transition from OMP recruitment to complex stabilization. Once the complex is assembled, the conformational changes within the membrane proximal domain of the MFP stimulates the transporter protein. Consequently, as the transporter protein relays protons into the cell, the OMP is opened and substrate is ejected out of the cell [7] (Figure I.0.7). All details of this mechanism are not known or confirmed. Assigned the roles of

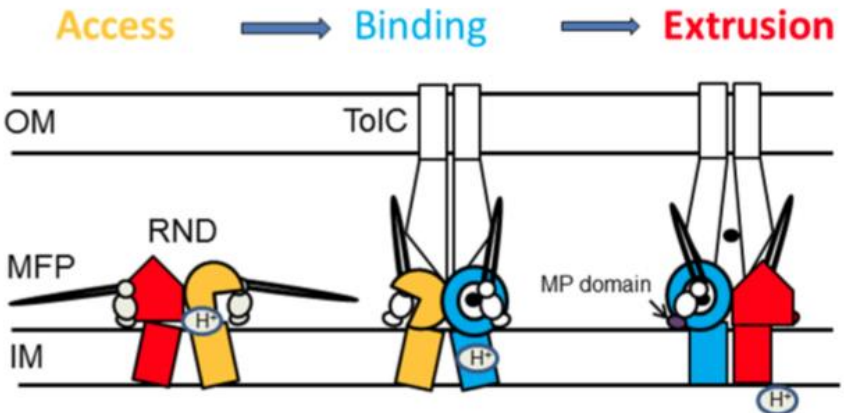

Figure I.0.7 Proposed Mechanism of RND Transporters
In the "Access" state, the preassembled transporter and membrane fusion protein pair is resting, ready-to-engage the outer membrane channel protein. In the "Binding" state, MFPs change conformation as they recruit and fully engage the OMP. The complex is now ready to expel substrates. Stimulation of the transporter protein by the MFP, in the "Extrusion" state, causes substrate expulsion coupled with proton influx. (Adapted from [7])

stabilizing the efflux pump, as well as bridging of the channel and transporter proteins, MFPs of these complexes require further investigation.

In the recently discovered *P. aeruginosa* RND pump, TriABC-OpmH there are two distinct MFPs, TriA and TriB [49]. The constitutively expressed OpmH is a homolog of the *E. coli* TolC. Together with the RND transporter, TriC, the TriABC-OpmH complex is a triclosan and SDS specific pump [33, 49] – triclosan is a substrate of various RND efflux pumps, including *Escherichia coli* AcrAB-TolC and *P. aeruginosa* MexAB-OprM [33, 50]. We created a covalently linked TriAB construct (TriAxB), where the MFPs were expressed as a single polypeptide. We found that TriAxB assembles as a hexameric oligomer, however, this construct form more stable complexes than the individually expressed TriAB [33]. More studies with this system, containing the hetero-hexameric MFP complex, can help further elucidate properties within RND efflux pumps.

I.3 Aims and Goals of Dissertation

Using this unique RND complex, TriABC-OpmH, as well as the broadly studied AcrAB-TolC, studies were implemented to resolve some of the unanswered questions of the field. We used biochemical methods such as mutagenesis, crosslinking, surface plasmon resonance (SPR), and fluorescence uptake assays. We sought to find out if the TriABC-OpmH complex assembles like other RND systems. Investigating the amino acid interactions at the MFP-OMP, as well as the MFP-IMP interfaces, we characterize the roles of the heterodimeric TriAB complex. We identify the MFP responsible for OMP recruitment, as well as the MFP responsible for stimulation of the transporter

protein. We further isolate the MFP responsible for opening the periplasmic aperture of the outer membrane channel protein. Coupling biochemical results with low-resolution protein structures, we highlight and propose the sequence events for complex assembly and mechanism of substrate expulsion.

Using the AcrAB-TolC system, we also tested the potential of efflux pump proteins as targets of inhibition. Synthesized inhibitors meant for the RND transporter, were used to determine kinetic parameters of said inhibitors and the AcrB transporter protein. We established the integrity of these inhibitors, proving their preferred binding to AcrB versus binding to AcrA and/or TolC.

II. Materials and Experimental Procedures

II.1 DNA Manipulations

II.1.1 List of Strains

Strain	Relevant Genotype	Source
JWW3	*Escherichia coli* K12 BW25113 Δ*ompT*::Km^r Δ*ompT*-scar Δ*acrAB*::Km^r *tolC*::Tn10	[33]
M6394	GC4468 Δ*acrB* Δ*acrD* Δ*acrEF*::spc^r Δ*emrB* Δ*emrY* Δ*entS*::cam^r Δ*macB* Δ*mdtC* Δ*mdtF*	[51]
GKCW101	M6394 *att*Tn*7*::mini Tn*7*T-*araC*-P_{BAD}-*fhuA* (FhuA ΔC/Δ4L_{His})	unpublished
GKCW102	BW25113 *att*Tn*7*::mini Tn*7*T-*lacI*^{q}-P_{TAC}-*fhuA* (FhuA ΔC/Δ4L_{His})	unpublished
GD102	BW25113 Δ*tolC-ygiBC*	[52]
GKCW104	GD102 *att*Tn*7*::mini Tn*7*T-*lacI*^{q}-P_{TAC}-*fhuA* (FhuA ΔC/Δ4L_{His})	unpublished
DH5α	*supE44* D*lacU169 hsdR17 rec*A1 *end*A1 *gyrA*96 *thi*-1 *rel*A1	
PAO1	*Pseudomonas aeruginosa* Wild type	[53]
PAO1116	PAO1 Δ*mexAB-oprM* Δ*mexCD-oprJ* Δ*mexEF-oprN* Δ*mexJK* Δ*mexXY* Δ*triABC*	[49]
GKCW122	PAO1 1116 *att*Tn*7*::mini-Tn*7*T- Gm^r-*lacI*^{q}-pLAC-*fhuADCD4L*	unpublished
JWW9	PAO1116 *att*Tn7:: mini-Tn7T-Tp^r-*araC*-P_{BAD}-*opmH* ($OpmH_{His}$)	[33]
JWW10	PAO1116 *att*Tn7:: mini-Tn7T-Tp^r-*araC*-P_{BAD}-*opmH* ($OpmH_{E173C, His}$)	This Study
JWW11	JWW10 Δ*opmH*::Gm^r	This Study
JWW12	PAO1116 *att*Tn7:: mini-Tn7T-Tp^r-*araC*-P_{BAD}-*opmH* ($OpmH_{K182C, His}$)	This Study
JWW13	JWW12 Δ*opmH*::Gm^r	This Study
JWW14	PAO1116 *att*Tn7:: mini-Tn7T-Tp^r-*araC*-P_{BAD}-*opmH* ($OpmH_{I392C, His}$)	This Study
JWW15	JWW14 Δ*opmH*::Gm^r	This Study
JWW16	PAO1116 *att*Tn7:: mini-Tn7T-Tp^r-*araC*-P_{BAD}-*opmH* ($OpmH_{V396C, His}$)	This Study

W4680AE	*Escherichia coli* K-12 *ΔacrAB::kan ΔacrEF::spe*	[54]
ZK796	*Escherichia coli* MC4100 *ΔtolC:: tet*	[55]
AG100AX	*Escherichia coli AG100 ΔacrAB::kan ΔacrEF::spe*	[54]

II.1.2 List of Plasmids

Plasmids	**Relevant Genotype**	**Source**
pBSPII (KS-/SK-)	Cb^r; broad-host-range cloning vector	[56]
pPS1824	Cb^r; pBSPII P_{lac}-*triABC*; Bla^r	[49]
pBSP-AxBC	Cb^r; pPS1824 expressing *triAxBC;*TriA and TriB are expressed as a fusion protein	[33]
pBSP-A_{R130D}xBC	Cb^r; expresses *triAxBC*; mutant *triA* ($TriA_{R130D}$)	This Study
pBSP-A_{G350C}xBC	Cb^r; expresses *triAxBC*; mutant *triA* ($TriA_{G350C}$)	This Study
pBSP-AxB_{R118D}C	Cb^r; expresses *triAxBC*; mutant *triB* ($TriB_{R118D}$)	This Study
pBSP-AxB_{G339C}C	Cb^r; expresses *triAxBC*; mutant *triB* ($TriB_{G339C}$)	This Study
pBAD33	Cm^r; expression vector; arabinose inducible promoter	[57]
pBAD33-ABC	Cm^r; expresses *triABC*; expresses Strep-tagged TriC	[33]
pBAD33-A_{R130D}BC	Cm^r; expresses triABC; mutant *triA* ($TriA_{R130D}$)	[33]
pBAD33-A_{G350C}BC	Cm^r; expresses *triABC*; mutant *triA* ($TriA_{G350C}$)	[33]
pBAD33-AB_{R118D}C	Cm^r; expresses *triABC*; mutant *triB* ($TriB_{R118D}$)	[33]
pBAD33-AB_{G339C}C	Cm^r; expresses *triABC*; mutant *triB* ($TriB_{G339C}$)	[33]
pBAD33-AxBC	Cm^r; expresses *triAxBC;* TriA and TriB are expressed as a fusion protein; expresses Strep-tagged TriC	[33]
pBAD33-AxB_{R133C}C	Cm^r; expresses *triAxBC*; mutant *triB* ($TriB_{R133C}$)	This Study
pBAD-A	Ap^r; expresses *triA*; 6-His tagged TriA	[33]
pBAD-B	Ap^r; expresses *triB*; 6-His tagged TriB	[33]
pBAD-C(His)	Ap^r; expresses *triC*; 6-His tagged TriC	[33]
pUC151B	Ap^r; expresses *acrAB*; 6-His tagged AcrB	[32]
pPS1283	Ap^r; Gm^r; pEX18ap-opmH-Gm	[58]

pTJ1	Ap^r; Tp^r; pUC18T-mini-Tn*7*T-Tp-*araC*-PBAD-MCS	*59*
pTJ1-opmH	Ap^r; Tp^r; expresses *opmH* ($OpmH_{His}$)	*33*
pTJ1-opmH-E176C	Ap^r; Tp^r; expresses *opmH* ($OpmH_{E173C, His}$)	This Study
pTJ1-opmH-K182C	Ap^r; Tp^r; expresses *opmH* ($OpmH_{K182C, His}$)	This Study
pTJ1-opmH-I392C	Ap^r; Tp^r; expresses *opmH* ($OpmH_{I392C, His}$)	This Study
pTJ1-opmH-V396C	Ap^r; Tp^r; expresses *opmH* ($OpmH_{V396C, His}$)	This Study
pTNS2	Ap^r; Helper plasmid expressing Tn7 transposase proteins TnsABCD	*60*
pBSP-A_{A116C}xBC	Cb^r; expresses *triAxBC*; mutant *triA* ($TriA_{A116C}$)	This Study
pBSP-A_{A134C}xBC	Cb^r; expresses *triAxBC*; mutant *triA* ($TriA_{A134C}$)	This Study
pBSP-A_{K138C}xBC	Cb^r; expresses *triAxBC*; mutant *triA* ($TriA_{K138C}$)	This Study
pBSP-A_{G139C}xBC	Cb^r; expresses *triAxBC*; mutant *triA* ($TriA_{G139C}$)	This Study
pBSP-A_{E145C}xBC	Cb^r; expresses *triAxBC*; mutant *triA* ($TriA_{E145C}$)	This Study
pBSP-AxB_{A104C}C	Cb^r; expresses *triAxBC*; mutant *triB* ($TriB_{A104C}$)	This Study
pBSP-AxB_{E122C}C	Cb^r; expresses *triAxBC*; mutant *triB* ($TriB_{E122C}$)	This Study
pBSP-AxB_{R126C}C	Cb^r; expresses *triAxBC*; mutant *triB* ($TriB_{R126C}$)	This Study
pBSP-AxB_{S127C}C	Cb^r; expresses *triAxBC*; mutant *triB* ($TriB_{S127C}$)	This Study
pBSP-AxB_{R133C}C	Cb^r; expresses *triAxBC*; mutant *triB* ($TriB_{R133C}$)	This Study
pBAD33-AxBC	Cm^r; expresses *triAxBC;* TriA and TriB are expressed as a fusion protein; expresses Strep-tagged TriC	*33*
pBAD33-AxB_{R133C}C	Cm^r; expresses *triAxBC*; mutant *triB* ($TriB_{R133C}$)	This Study
pBAD-C(His)	Ap^r; expresses *triC*; 6-His tagged TriC	*33*
pAcrA (His)	Ap^r; expresses *acrA*; 6-His tagged AcrA	*20*
$pAcrA_{D149C}$	Ap^r; expresses *acrA*; 6-His tagged AcrA; mutant *acrA* ($AcrA_{D149C}$)	This Study
$pAcrA_{G363C}$	Ap^r; expresses *acrA*; 6-His tagged AcrA; mutant *acrA* ($AcrA_{G363C}$)	*48*
pTolC (His)	Ap^r; expresses *tolC*; 6-His tagged TolC	*32*
$pTolC_{YFRE}$	Apr; expresses *tolC*; 6-His tagged TolC; mutant *tolC* ($TolC_{Y362F, R367E}$)	*61, 62*

$pTolC_{Q142C}$	Ap^r; expresses *tolC*; 6-His tagged TolC; mutant *tolC* ($TolC_{Q142C}$)	*63*
$pTolC_{A269C}$	Ap^r; expresses *tolC*; 6-His tagged TolC; mutant *tolC* ($TolC_{A269C}$)	*63*
$pTolC_{D374C}$	Ap^r; expresses *tolC*; 6-His tagged TolC; mutant *tolC* ($TolC_{D374C}$)	*63*
$pTolC_{K383C}$	Ap^r; expresses *tolC*; 6-His tagged TolC; mutant *tolC* ($TolC_{K383C}$)	This Study
$pYFRE_{Q142C}$	Ap^r; expresses $tolC_{YFRE}$; 6-His tagged TolC; mutant $tolC_{YFRE}$ ($YFRE_{Q142C}$)	*63*
$pYFRE_{A269C}$	Ap^r; expresses $tolC_{YFRE}$; 6-His tagged TolC; mutant $tolC_{YFRE}$ ($YFRE_{A269C}$)	*63*
$pYFRE_{D374C}$	Ap^r; expresses $tolC_{YFRE}$; 6-His tagged TolC; mutant $tolC_{YFRE}$ ($YFRE_{D374C}$)	*63*
$pYFRE_{K383C}$	Ap^r; expresses $tolC_{YFRE}$; 6-His tagged TolC; mutant $tolC_{YFRE}$ ($YFRE_{K383C}$)	This Study
$pAcrA_{G362C}$	Ap^r; expresses *acrA*; 6-His tagged AcrA; mutant *acrA* ($AcrA_{G362C}$)	*48 64*
$pAcrB_{S1043C}$	Ap^r; expresses *acrB*; 6-His tagged AcrB; mutant *acrB (*$AcrB_{S1043C}$)	*44*
$pAcrB_{D408A}$	Ap^r; expresses $acrB_{S1043C}$; 6-His tagged AcrB; mutant *acrB (*$AcrB_{D408A, S1043C}$)	This Study

	Forward 5' - 3'	Reverse 5' - 3'
AcrA		
Asp 149 Cys	CGATCAGGCTCTGGCTTGTGCGCAACAGGCG	CGCCTGTTGCGCACAAGCCAGAGCCTGATCG
AcrB		
Asp 408 Ala	CATCGGCCTGTTGGTGGATGCCGCCATCGTTGTGGTAG	CTACCACAACGATGGCGCCATCCACCAACAGGCCGATG
OpmH		
Glu 173 Cys	GCTGGACCAGGCCAACTGCCGCTTCGACGTGGGCC	GGCCCACGTCGAAGCGGCAGTTGGCCTGGTCCAGC
Lys 182 Cys	CGTGGGCCTTTCCGACTGCACCGACGTGCTCGAGG	CCTCGAGCACGTCGGTGCAGTCGGAAAGGCCCACG
Ile 392 Cys	CCAGAGTTCGCTGGAGGCCACCGAGTGCGGCTACCAGGTCGGC	GCCGACCTGGTAGCCGCACTCGGTGGCCTCCAGCGAACTCTGG
Val 396 Cys	CCGAGATCGGCTACCAGTGCGGCACCCcCAACATCGTCGACG	CGTCGACGATGTTGgGGGTGCCGCACTGGTAGCCGATCTCGG
TolC		
Lys 383 Cys	GCGACCACCACGTTGTACAACGCCTGCCAAGAGCTGGCG	CGCCAGCTCTTGGCAGGCGTTGTACAACGTGGTGGTCGC
TriA		
Ala 116 Cys	GCCCAGGCGGCGGTatgtGCGCAGCAGGCGC	GCGCCTGCTGCGCACATACCGCCGCCTGGGC
Ala 134 Cys	CCTCAACTACCAGCGCCAGAAGTGCCTGCTCCCCAAGGGCTACACC	GGTGTAGCCCTTGGGGAGCAGGCACTTCTGGCGCTGGTAGTTGAGG
Lys 138 Cys	GGCGCTGCTGCCCTGCGGATACACCAGCCAGAGC	GCTCTGGCTGGTGTATCCGCAGGGCAGCAGCGCC
Gly 139 Cys	GGCGCTGCTGCCCAAGTGCTACACCAGCCAGAGC	GCTCTGGCTGGTGTAGCACTTGGGCAGCAGCGCC
Glu 145 Cys	GCTACACCAGCCAGAGCtgtTACGACCAGGCGCTGG	CCAGCGCCTGGTCGTAACAGCTCTGGCTGGTGTAGC
TriB		
Ala 104 Cys	GCGCCAGCCAGGGaGACCTatgcAGCGCCGAGGCACAG	CTGTGCCTCGGCGCTGCATAGGTCTCCCTGGCTGGCGC
Glu 122 Cys	GCCCGGCGCCAGGAATGCCTGTTCGCCCGCAGCG	CGCTGCGGGCGAACAGGCATTCCTGGCGCCGGGC
Arg 126 Cys	GGAAGAACTGTTCGCGTGCAGCGTCACCGCCCAGGC	GCCTGGGCGGTGACGCTGCACGCGAACAGTTCTTCC
Ser 127 Cys	GGAAGAACTGTTCGCCCGCTGCGTCACCGCCCAGG	CCTGGGCGGTGACGCAGCGGGCGAACAGTTCTTCC
Arg 133 Cys	CGTCACCGCCCAGGCGtgtCTGGACGATGCGCGG	CCGCGCATCGTCCAGACACGCCTGGGCGGTGACG

II.1.4 Site-Directed Mutagenesis

All point mutations were introduced using either the Stratagene QuickChange-XL or Lightning site-directed mutagenesis kit, as recommended by the manufacturer. Briefly, the resulting PCR products were treated with DpnI, transformed into DH5α competent cells and plated on Luria Bertani (LB) agar containing ampicillin (100 µg/ml). For each mutant, at least two plasmids were purified and sequenced to assess the presence of the desired mutation. All mutations were verified by DNA sequencing at the Oklahoma Medical Research Foundation (OMRF) DNA Sequencing Facilities.

II.1.5 OpmH Cloning

All strains and plasmids constructed in this study are shown in tables above. Mutations were introduced into pTJ1-opmH using manufacturer's instructions (QuikChange Lightning, Agilent Technologies). Mutated mini Tn7 cassettes were integrated onto the chromosome of PAO1116 via co-electroporation with pTNS2 and selected on LB plates containing trimethoprim (15 µl/ml). Confirmed integrants were then subjected to mating with *E. coli* Sm10/pPS1283, upon mating haploid deletion strains were selected on LB media supplemented with 30 µg/ml gentamicin, 5% sucrose and 1% arabinose. PCR and sequencing (OMRF) were performed to confirm the native *opmH* gene had been deleted and that the cysteine mutant *opmH* gene was present under the control of the arabinose promoter.

II.2 Minimal Inhibitory Concentration (MIC) Determinations

Overnight cultures of *P. aeruginosa* or *E. coli* carrying indicated constructs were diluted 1 to 100 in LB broth supplemented with a selection marker grown at 37°C with shaking for 5 hours. MICs of antimicrobial agents were measured using the two-fold dilution technique in 96-well microtitre plates [65]. At an optical density at 600 nm (OD_{600}) of ~1.0, cells were inoculated at a density of $5x10^4$ cells per ml in LB in the presence of two-fold increasing concentrations of substrates under investigation. The cultures were incubated for 18-24 hours, and the lowest concentration that completely inhibited bacterial growth was designated the MIC. When required, protein expression was induced by adding 1.0 mM IPTG, 0.2% L-arabinose, or 1% L-arabinose to cell cultures at OD_{600} of ~0.3-0.5, and cells were further incubated at 37°C for 3 more hours till OD_{600} ~1.0-1.2.

II.3 Protein Purification

II.3.1 AcrA

For the purification of AcrA and its cysteine variants, W4680AE cells carrying the appropriate plasmid from fresh transformation were inoculated into 15 ml LB containing 100 µg/ml ampicillin. After 2 hours, 10 ml of cells were reinoculated into 1 L LB medium. The production of proteins was induced by the addition of isopropyl-1-thio-β-galactoside (IPTG), 0.1 mM final concentration, after 3 hours of growth then left to grow overnight. Cells were harvested by low speed centrifugation at 3,220 x g for 20 mins at 4°C then washed with 10 mM Tris-HCl (pH 8.0) and centrifuged. The pellets were resuspended in 10 mM Tris-HCl (pH 8.0), 5 mM ethylenediaminetetraacetate

(EDTA), 1 mM phenylmethylsulfonyl fluoride (PMSF) and 100 µg/ml lysozyme and incubated on ice for 30 mins. The cells were lysed thrice for 30-45 sec using an ultrasonicator (Branson). Unbroken cells were removed by low speed centrifugation at 3,220 x g for 30 mins. Cell membranes were isolated by high speed centrifugation at >100,000 x g for 1 hr at 4°C in Beckman Ti-45, then washed for an hour at >100,000 x g after resuspension in 20 mM Tris-HCl (pH 8.0), 100 mM NaCl, and 1 mM PMSF. The membrane pellets were resuspended in 20 mM Tris-HCl (pH 8.0), 500 mM NaCl, 1 mM PMSF, and 5 mM Imidazole then sonicated before adding n-dodecyl β-D-maltoside (DDM) to a final concentration of 2%. Membranes were solubilized overnight and centrifuged at >100,000 x g for 30 mins at 4°C then loaded onto a NTA column charged with 50 mM $CuSO_4$. Samples were washed in 20 mM Tris-HCl (pH 8.0), 500 mM NaCl, 1 mM PMSF, and 0.03% DDM buffer with a gradient of imidazole concentrations. For binding buffers with 5 mM, 25 mM, and 50 mM Imidazole, one fraction of 10-20 column volumes (CVs) was collected. Five fractions of 2 CVs were collected for binding buffer with 100 mM Imidazole. AcrA was eluted in 20 mM Tris-HCl (pH 8.0), 500 mM NaCl, 1 mM PMSF, 0.03% DDM, and 500 mM Imidazole – three fractions of 2 CVs. Purified proteins were dialyzed (one round with 10 mM EDTA) and stored in 20 mM Tris-HCl (pH 8.0), 500 mM NaCl, 1 mM PMSF, and 0.03% DDM until used in experiments. All collected fractions are separated by 10% SDS-PAGE gel electrophoresis and visualized by Coomassie Blue Staining.

II.3.2 AcrB

For the purification of AcrB and its cysteine variants, overnight cultures of AG100X cells carrying the appropriate plasmid was reinoculated (1:100) in 1 L LB containing 100 µg/ml ampicillin. The production of proteins was induced by the addition of isopropyl-1-thio-β-galactoside (IPTG), 1.0 mM final, after 4 hours of growth then left to grow an additional 3 hours. Cells were harvested by low speed centrifugation at 5,000 rpm for 20 mins at 4°C then the pellets were resuspended in 10 mM Tris-HCl (pH 8.0), 5 mM ethylenediaminetetraacetate (EDTA), 1 mM phenylmethylsulfonyl fluoride (PMSF) and 100 µg/ml lysozyme and incubated on ice for 30 mins. The cells were lysed thrice for 30-45 sec using an ultrasonicator (Branson). Unbroken cells were removed by low speed centrifugation at 3,220 x g for 30 mins. Cell membranes were isolated by high speed centrifugation at >100,000 x g for 1 hr at 4° in Beckman Ti-45, then washed twice for 1.5 hours at >100,000 x g in 20 mM Tris-HCl (pH 8.0), 500 mM NaCl, and 1 mM PMSF with and without 0.2% Triton X100, respectively. The membrane pellets were resuspended in 20 mM Tris-HCl (pH 8.0), 500 mM NaCl, 1 mM PMSF, 5 mM Imidazole and 2% n-dodecyl β-D-maltoside (DDM). Membranes were solubilized for 4 hours or overnight and centrifuged at >100,000 x g for 30 mins at 4°C then loaded onto a NTA column charged with 50 mM $CuSO_4$. Samples were washed in 20 mM Tris-HCl (pH 8.0), 500 mM NaCl, 1 mM PMSF, and 0.03% DDM buffer with a gradient of imidazole concentrations. For binding buffers with 5 mM, 20 mM, and 50 mM Imidazole, one fraction of 10-20 column volumes (CVs) was collected. Two fractions of 2.5 CVs were collected for binding buffer with 100 mM Imidazole. AcrB was eluted in 20 mM Tris-HCl (pH 8.0), 500 mM NaCl, 1

mM PMSF, 0.03% DDM, and 500 mM Imidazole – five fractions of 1 CV. Purified proteins were dialyzed (one round with 10 mM EDTA) and stored in 20 mM Tris-HCl (pH 8.0), 500 mM NaCl, 1 mM PMSF, and 0.03% DDM until used in experiments. All collected fractions are separated by 10 % SDS-PAGE gel electrophoresis and visualized by Coomassie Blue Staining.

II.3.3 TolC

In order to purify TolC and its cysteine variants, overnight cultures of ZK796 cells carrying the appropriate plasmid was reinoculated (1:100) into20 mL LB containing 100 µg/ml ampicillin. After ~1 hour, 10 ml of cells was reinoculated into 1 L LB medium. The production of proteins was induced by the addition of IPTG, 0.2 mM final, when OD_{600} is ~0.3-0.5, then left to grow overnight. Cells were harvested by low speed centrifugation at 5,000 rpm for 20 mins at 4°C then the pellets were resuspended in 20 mM Tris-HCl (pH 7.5), 5 mM $MgCl_2$, 1 mM phenylmethylsulfonyl fluoride (PMSF) and 0.05 mg/ml DNAse and incubated on ice for 30 mins. The cells were lysed by French press, thrice at 1000 psi. Unbroken cells were removed by low speed centrifugation at 3,220 x g for 30 mins. Cell membranes were isolated by high speed centrifugation at >100,000 x g for 1 hr at 4°C in Beckman Ti-45, then washed twice for 1.5 hours at >100,000 x g in 20 mM Tris-HCl (pH 7.5), 100 mM NaCl, 20 mM $MgCl_2$ and 1 mM PMSF with and without 0.5% Triton X100, respectively. The membrane pellets were resuspended in 20 mM Tris-HCl (pH 7.5), 100 mM NaCl, 1 mM PMSF, 5 mM Imidazole and 1% n-dodecyl β-D-maltoside (DDM). Membranes were solubilized for 5 hours or overnight and centrifuged at >100,000 x g for 30 mins at 4°C

then loaded onto a NTA column charged with 50 mM $CuSO_4$. Samples were washed in 20 mM Tris-HCl (pH 7.5), 100 mM NaCl, 1 mM PMSF, and 0.03% DDM buffer with a gradient of imidazole concentrations. For binding buffers with 5 mM, 20 mM, 50 mM and 10 mM Imidazole, one fraction of 10-20 column volumes (CVs) was collected. TolC was eluted in 20 mM Tris-HCl (pH 7.5), 100 mM NaCl, 1 mM PMSF, 0.03% DDM, and 500 mM Imidazole – four fractions of 1 CV. Purified proteins were dialyzed (one round with 10 mM EDTA) and stored in 20 mM Tris-HCl (pH 7.5), 500 mM NaCl, 1 mM PMSF, and 0.03% DDM until used in experiments. All collected fractions are separated by 10 % SDS-PAGE gel electrophoresis and visualized by Coomassie Blue Staining.

II.3.4 TriA, TriB, TriC, TriABC, and TriAxBC and Variants

In order to purify Tri proteins and cysteine variants, overnight cultures of JWW3 cells carrying the appropriate plasmid were reinoculated (1:100) into 1 L LB containing the appropriate resistance marker – 100 µg/ml ampicillin and/or 12.5 µg/ml chloramphenicol. When necessary, production of proteins was induced by the addition of 0.2% L-arabinose, when OD_{600} is ~0.3-0.5 then left to grow for 5 hours. Cells were harvested by low speed centrifugation at 5,000 rpm for 20 mins at 4°C then the pellets were resuspended in 20 mM Tris-HCl (pH 7.5), 5 mM $MgCl_2$, 1 mM phenylmethylsulfonyl fluoride (PMSF) and 0.05 mg/ml DNAse and incubated on ice for 30 mins. The cells were lysed thrice for 30-45 sec using an ultrasonicator (Branson). Unbroken cells were removed by low speed centrifugation at 3,220 x g for 30 mins. Cell membranes were isolated by high speed centrifugation at >100,000 x g for 1 hr at

4°C in Beckman Ti-45, then washed for 1.5 hours at >100,000 x g in 10 mM Tris-HCl (pH 7.5), 100 mM NaCl, and 1 mM PMSF. The membrane pellets were resuspended in 50 mM Tris-HCl (pH 7.5), 150 mM NaCl, 1 mM PMSF, 10 mM Imidazole and 2% n-dodecyl β-D-maltoside (DDM). Membranes were solubilized overnight and centrifuged at >100,000 x g for 30 mins at 4°C then loaded onto a NTA column charged with 50 mM $CuSO_4$. Samples were washed in 50 mM Tris-HCl (pH 7.5), 150 mM NaCl, 1 mM PMSF, and 0.03% DDM buffer with a gradient of imidazole concentrations. For binding buffers with 5 mM, 20 mM, and 40 mM Imidazole, one fraction of 10-20 column volumes (CVs) was collected. Tri proteins were eluted in 50 mM Tris-HCl (pH 7.5), 150 mM NaCl, 1 mM PMSF, 0.03% DDM, and 400 mM Imidazole – seven fractions of 0.5 CV. Purified proteins were dialyzed (one round with 10 mM EDTA) in 50 mM Tris-HCl (pH 7.5), 150 mM NaCl, 1 mM PMSF, and 0.03% DDM when ready to be used in experiments. All collected fractions are separated by 12 % SDS-PAGE gel electrophoresis and visualized by Coomassie Blue Staining.

II.3.5 OpmH

In order to purify Tri proteins and cysteine variants, overnight cultures of JWW3 cells carrying the appropriate plasmid was reinoculated (1:100) into 1 L LB containing the appropriate resistance marker – 100 µg/ml ampicillin and/or 12.5 µg/ml chloramphenicol. When necessary, production of proteins was induced by the addition of 0.2% L-arabinose, when OD_{600} is ~0.3-0.5 then left to grow for 5 hours. Cells were harvested by low speed centrifugation at 5,000 rpm for 20 mins at 4°C then the pellets were resuspended in 20 mM Tris-HCl (pH 7.5), 5 mM $MgCl_2$, 1 mM

phenylmethylsulfonyl fluoride (PMSF) and 0.05 mg/ml DNAse and incubated on ice for 30 mins. The cells were lysed thrice for 30-45 sec using an ultrasonicator (Branson). Unbroken cells were removed by low speed centrifugation at 3,220 x g for 30 mins. Cell membranes were isolated by high speed centrifugation at >100,000 x g for 1 hr at 4°C in Beckman Ti-45, then washed for 1.5 hours at >100,000 x g in 10 mM Tris-HCl (pH 7.5), 100 mM NaCl, and 1 mM PMSF. The membrane pellets were resuspended in 50 mM Tris-HCl (pH 7.5), 150 mM NaCl, 1 mM PMSF, 10 mM Imidazole and 2% n-dodecyl β-D-maltoside (DDM). Membranes were solubilized overnight and centrifuged at >100,000 x g for 30 mins at 4°C then loaded onto a NTA column charged with 50 mM $CuSO_4$. Samples were washed in 50 mM Tris-HCl (pH 7.5), 150 mM NaCl, 1 mM PMSF, and 0.03% DDM buffer with a gradient of imidazole concentrations. For binding buffers with 5 mM, 20 mM, 40 mM and 75 mM Imidazole, one fraction of 10-20 column volumes (CVs) was collected. OpmH protein was eluted in 50 mM Tris-HCl (pH 7.5), 150 mM NaCl, 1 mM PMSF, 0.03% DDM, and 400 mM Imidazole – five fractions of 1 CV. Purified proteins were dialyzed (one round with 10 mM EDTA) in 50 mM Tris-HCl (pH 7.5), 150 mM NaCl, 1 mM PMSF, and 0.03% DDM when used in experiments. All collected fractions are separated by 10 % SDS-PAGE gel electrophoresis and visualized by Coomassie Blue Staining.

II.4 Fluorophore Uptake Assays

E. coli GKCW101 cells carrying indicated constructs were inoculated into 5 ml LB medium with 100 µl/ml and grown at 37°C with shaking at 200 rpm to OD_{600}~0.3. At this optical density, cells were induced with 0.1% L-arabinose grown until the cells

reached OD_{600}~1.0. Cells were then pelleted at room temperature by centrifugation for 15 min. The pellet was resuspended and washed in 25 ml of the 50 mM KPO_4^{3-}, 1 mM $MgCl_2$, and 0.4% glucose (PMG) buffer. Pellet was resuspended to an OD_{600}~1.0 in PMG buffer and kept at room temperature during the course of the experiment. Uptake assays were performed in a Tecan Spark 10M micro-plate reader in a fluorescence mode. At 20, 000 Z-position and 100 gain, fluorescence intensities were measured for 10 minutes.

II.5 Spontaneous Sulfide Crosslinking

Overnight JWW9, JWW11, JWW13, and JWW15 cultures were reinoculated in 5 ml LB broth, supplemented with selection marker and 1% L-arabinose, at 1:100 dilutions and grown at 37°C. Cells were harvested after reaching OD_{600} ~1.0 (after about 6 hours) and washed in 1X phosphate buffer saline (PBS). Cell pellets were resuspended in 1 ml PBS with 2 mM n-ethyl-maleimide (NEM) and incubated for 5 minutes at room temperature; afterwards, cells were washed in PBS buffer. (At this stage, cells can be frozen for storage and later use.) Cell pellets were resuspended in 10 mM Tris-HCl (pH 8.0), 5 mM ethylenediaminetetraacetate (EDTA), and 100 µg/ml lysozyme and incubated on ice for 30 mins. The cells were lysed thrice for 30-45 sec using an ultrasonicator (Branson). Unbroken cells were removed by low speed centrifugation at 3,220 x g for 30 mins. Cell membranes were isolated by high speed centrifugation at >100,000 x g for 1 hr at 4° in Beckman TLA 55. Membranes were washed and resuspended in 50 µl 10 mM Tris-HCl (pH 8.0). Membrane proteins were quantified by the BSA Bradford Assay, and equal amounts were separated by SDS-

PAGE gel electrophoresis. Samples were transferred onto polyvinylidene fluoride (PVDF) membranes, and proteins are identified by immunoblotting. 5 µg total membranes were probed by anti-TriB serum [33], while 10 µg of proteins was used for detection by the anti-His antibody (Pierce).

II.6 Azithromycin Spot Assay

Overnight cultures of *P. aeruginosa* carrying the indicated constructs were diluted 1:100 in LB broth supplemented with 1% L-arabinose and 200 µg/ml and grown at 37°C with shaking at 200 rpm for 5 hours. Four ml of molten soft agar (50% LB, 50% LBA, supplemented with 1% arabinose), was inoculated with 300 µl of freshly grown culture and poured over LBA plates supplemented with 1% arabinose. Soft agar was allowed to solidify and spotted with four 10 µl spots of 0.15 µg/ml azithromycin in DMSO (1.5 µg per spot). Spots were allowed to absorb into agar for 15 minutes prior to incubation at 37°C for 18 hours. Zones of inhibition were recorded and are an average of 8 spots per strain were determined and shown. Standard error and Student's T-test with two-tailed unpaired parameters were calculated on samples using Excel. P values of 0.05 were considered statistically significant.

II.7 Protein Labeling with NANOGOLD®

Purified proteins were dialyzed into 50 mM Tris-HCl (pH 7.5), 150 mM NaCl, 1 mM PMSF, and 0.03% DDM, no imidazole. Thiol groups were reduced in the equal volume of tris(2-carboxyethyl)phosphine (TCEP) resin – the duration of reduction was based on recommended times given by the Thermo Pierce manual. Reduced protein

was eluted off the TCEP resin in 50 mM Tris-HCl (pH 7.5), 150 mM NaCl, 1 mM PMSF, and 0.03% DDM – five fractions of one column volume was collected in separate tubes. Proteins concentrations were estimated for each fraction by incubating in BioRad Protein Assay dye and measuring Abs at 595 nm. Peak fractions were combined then incubated with fresh monomaleimido NANOGOLD® (Nanoprobes) in 2 molar excess. Excess NANOGOLD® was removed from the sample using Nap™-5 Sephadex™ G-25 DNA Grade columns (GE Healthcare) and proteins were dialyzed into 50 mM Tris-HCl (pH 7.5), 150 mM NaCl, and 0.03% DDM.

II.8 Negative Staining Electron Microscopy (EM)

II.8.1 Sample Preparation and Image Acquisition.

EM studies were carried by Lucien Fabre and Isabelle Rouiller at McGill University, Canada. Purified TriC and TriAxBC samples (each 5 µL diluted to ~50 µg/ml) were applied onto negatively glow-discharged carbon-coated grids (400 mesh, copper grid) for 1 min. Excess liquid was removed by blotting with filter paper. Freshly prepared 1.5% uranyl formate (pH 5.0) was added (5 µl) for 1 min and then blotted dry. Digital micrographs were collected using a FEI Tecnai G2 F20 microscope operated at 200 kV and equipped with a Gatan Ultrascan 4k x 4k Digital CCD Camera. The images were recorded at defocus between 1.0−2.0 µm at a magnification of 134,010X at the camera and a pixel size of 1.12 Å.

II.8.2 EM Data Processing and Image Analysis.

Contrast transfer function parameters were determined using ctffind3 [66]. Protein particles were boxed using an in-house autoboxing software using an input template obtained by averaging ~100 particles randomly oriented. After extraction, particles were binned 2X for a final box size of 128x128 pixels and a resulting pixel size of 2.24 Å at specimen level. 84,288 particles were collected for EM reconstruction of TriC. These particles were initially submitted to Iterative Stable Alignment and Clustering (ISAC) 2D classification [67]. Further analysis was performed using 21,522 validated by this procedure. An initial reference map generated *de novo* using PRIME [68] and was used for ML3D classification and 3D refinement using Relion 1.3 [69]. 3D classification of the validated particles was initiated with 7 seeds and a tau of 4. Two of the classes obtained contained few particles and the corresponding particles were discarded. The handiness of the maps was visually determined one in respect of another and by comparison with the high resolution model. 16,336 and 11,393 particles were analyzed for TriAxBC and $TriAxB_{R133C}C$-•NANOGOLD® in a similar fashion. ML3D classification was performed using 4 seeds and a tau value of 4. The initial model was the TriC *de novo* volume filtered at 60 Å. This classification led to 4 identical classes for both data set. An additional refinement was performed including all the particles. All structures have a resolution estimated between 20 to 25 Å.

II.9 Proteolysis

For *in vivo* proteolysis, cells were grown to OD_{600} ~1.0 then harvested and washed twice in 20 mM Tris-HCl (pH 7.5) and 100 mM NaCl. Cell pellets were

resuspended in 200 µl 20 mM Tris-HCl (pH 7.5), 5 mM EDTA, and 20% sucrose then aliquoted and treated with increasing concentrations of trypsin. Samples were incubated for 1 hour in 37°C water bath. The reaction was stopped with sample buffer with 2-mercaptoethanol (βME), boiled for 5 minutes, and separated by SDS-PAGE gel electrophoresis. Proteins fragments were visualized by immunoblotting using anti-TriA and anti-TriB serums [33]. Purified proteins were treated the same as whole cells for proteolysis. Fragments visualized by silver staining or by immunoblotting with corresponding polyclonal rabbit antibodies.

II.10 Pyrene Maleimide Labeling

Purified AcrA was dialyzed into 20 mM Tris-HCl (pH 8.0), 500 mM NaCl and 0.03% DDM (AcrA Buffer A) while purified TolC proteins were dialyzed into 20 mM Tris-HCl (pH 8.0), 100 mM NaCl and 0.03% DDM (TolC Buffer A). Thiol groups were reduced in the equal volume of tris(2-carboxyethyl)phosphine (TCEP) resin – the duration of reduction was based on recommended times given by the Thermo Pierce manual. Five fractions of protein, one column volume, were collected in the respective Buffer A. Protein concentrations were estimated for each fraction by incubating in BioRad Protein Assay dye and measuring Abs at 595 nm. Peak fractions were combined then incubated with fresh pyrene maleimide in 20 molar excess. Excess pyrene was removed from the sample using Nap™-5 Sephadex™ G-25 DNA Grade columns (GE Healthcare) and dialyzed into 20 mM MES (pH 6.0), 0.03% DDM and 150 mM NaCl buffer for experiments.

II.11 Fluorescence Spectroscopy

Pyrene labeled proteins (0.5 – 1.0 ml) were used for fluorescence spectroscopy using the Shimadzu RF-5301 spectrofluorometer. After mixing labeled samples, pyrene was excited with light at 337 nm and the emission spectrum readout was used for analysis. If the two pyrene rings were within 10 Å of each other, a red shift emission peak at ~470 nm would be observed for the excimers. However, if the labeled positions were not within range for stacking, the singular molecules were observed at wavelengths of 375-395 nm [70]. At bandwidths of 3 nm, automatic response time, and super (1nm interval) scan speeds, pyrene molecules were excited at 337 nm and the emission light intensities were measured between 360 and 560 nm. Scan speed was reduced to slow in later experiments, when protocol was being optimized. For Quantitative experiments using free pyrene, the probe was excited at 337 nm and the emission intensities of the first of the twin peaks was measured at 376 nm – concentrations were set to mg/ml, bandwidths 5 nm, and response time was automatic. Time course experiments measured the emission of pyrene at 465 nm through 3 nm bandwidths. Readings were recorded every 2 seconds for 301 readings (10 minutes).

II.12 Surface Plasmon Resonance

II.12.1 Thiol Coupling

Purified AcrA and AcrB were dialyzed into 20 mM Tris-HCl (pH 8.0), 500 mM NaCl, 1 mM PMSF, and 0.03% DDM while purified TolC proteins were dialyzed into 20 mM Tris-HCl (pH 8.0), 100 mM NaCl and 0.03% DDM. Thiol groups were reduced, in equal volumes of protein and tris(2-carboxyethyl)phosphine (TCEP) resin,

immediately before the experiments. Collected fractions were checked for protein content and concentrations, the highest were used for immobilization.

II.12.2 Immobilization

For the SensíQ® Pioneer and Biacore 3000, new sensor chip surfaces (COOH5 and CM5, respectively) are cleaned with 20 mM CHAPS in 20 mM MES 6.0, 150 mM NaCl, and 0.03% DDM running buffer (RB) after the system had been primed twice with RB. Equal volumes of 0.4 1-Ethyl-3-(3-dimethylaminopropyl)carbodiimide (EDC) and 0.1 *N*-hydroxysuccinimide (NHS) are injected over the chip surface for 2 mins at 5-10 μl/min. The activated surface was immediately reacted with 2-(2-pyridinyldithio)ethaneamine (PDEA), 80 mM in 0.1 M $NaBO_3$ pH 8.5), to introduce a disulfide bond, for 4 mins at 5-10 μl/min. This disulfide is the position at which proteins of interest compete and bind to. Cysteine-containing proteins were diluted in 10 mM MES (pH 5.0) and 0.03% n-dodecyl β-D-maltoside (DDM) and injected on the surface in varying times and replicates at 5-10 μl/min. For the control surface, 10 mM MES (pH 5.0) and 0.03% DDM was injected to mock the protein surfaces. Unreacted chemistry was capped with cysteine in MES (pH 5.0) and 1 mM NaCl, and surfaces were washed with 40 mM CHAPS in Tris-HCl (pH8.0) to remove non-specific binding. Immobilized protein was calculated by subtraction the surface density post PDEA from the densities prior to cysteine capping.

II.12.3 Data Collection and Normalization

For protein-protein interactions and protein-inhibitor experiments, flow rates were set to 40-50 µl/min. In the case of inhibitor experiments, the running buffer was supplemented with 5% DMSO to match the conditions of solubilization. Samples were injected onto immobilized and control surfaces for 1 to 2 minutes at 40-50 µl/min. Quick injects of 40 mM CHAPS (pH 8.0) was use to clean surface as necessary – between concentration dependent injections and/or between different samples. Binding curves were normalized by aligning and subtracting control surface responses, as well as the sensogram of RB (with DMSO) corresponding to the EPI concentration. Fitting and kinetic parameters were determined from normalized sensograms, using Qdat© on the SensíQ® Pioneer, and BIAEvaluation 2.1© for the Biacore 3000 unit or Excel.

Chapter 1. Non-Equivalent Roles of TriA and TriB in Efflux

TriABC-OpmH of *P. aeruginosa* is a unique RND system with two independently expressed MFPs – TriA and TriB. Using this complex as the model of studying RND transporters, we sought to understand the role of TriA and TriB proteins within the assembled complex. We established that TriA and TriB can be covalently linked to express and assemble heterodimers within a functional complex [33]. We introduced point mutations in the coiled coil and membrane proximal (MP) domains of TriAB, based on amino acid residues in AcrA (Arg 128 and Gly 363)[48, 71], which caused a loss of complex function but did not affect complex assembly. We established that each MFP has independent roles within the complex. Using analogous aspartic acid ($TriA_{R130D}$ and $TriB_{R118D}$) mutants of the α-helical domain (Figure 1.0.1), we found that TriA is responsible for the recruitment and stabilization of the efflux pump by means of interactions with the OMF. Cysteine mutations in a conversed glycine position

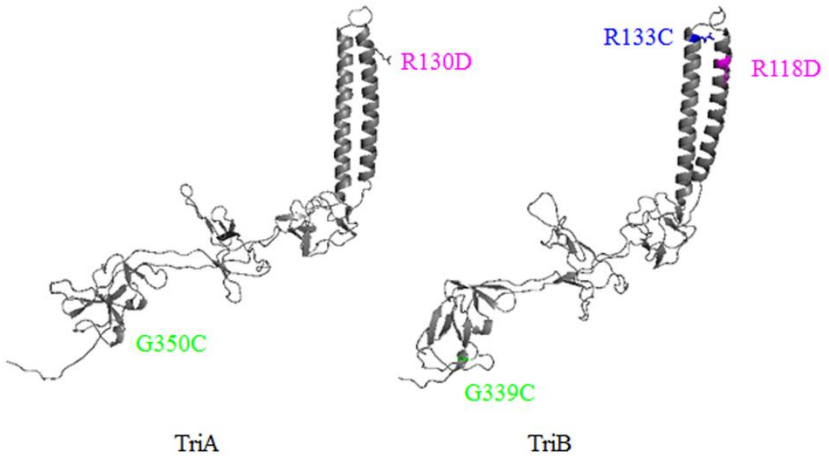

Figure 1.0.1 Protein Structures of TriA and TriB
Crystal structure of TriA and TriB based on MexA (PDB code: 2V4D) with highlighted amino acids used in mutagenesis. Mutations of the coiled coil (magenta) and membrane proximal domains (green) were used in uptake and proteolysis studies. TriB Arg 133 (blue) was labeled with NANOGOLD® and used for negative staining electron microscopy (EM)

($TriA_{G350C}$ and $TriB_{G339C}$) of the MP domain proved that TriB plays an important role in

interacting with the transporter, TriC, for a functional complex. In this study, we reconstituted the efflux activity of TriABC in *E. coli* cells and characterized the functional properties of TriA and TriB. We also find that TriABC takes on different conformations in the presence and absence of the outer membrane channel.

1.1 TriABC and TriAxBC are Expressed and Functional in *E. coli* GKCW101 (Δ9FhuA)

In order to test the functionality of TriABC complex we expressed these proteins in *E. coli* GKCW101 (Δ9FhuAΔC/Δ4L or Δ9FhuA) – a strain which lacks nine transporters that function with TolC, and has the outer membrane permeabilized (expressed FhuA proteins lacked their cork domain and 4 extracellular loops) (Krishnamoorthy et. al submitted). The permeability barrier of the Gram-negative bacterial cell wall limits the uptake of compounds into the cell, as well as masks the activity of efflux pumps. We used E. coli GKCW101 in order to reduce limiting factors at the outer membrane. We expressed the TriABC complex and its covalently linked variant, TriAxBC, in Δ9FhuA (Figure 1.0.2) and found that the cell's susceptibility to

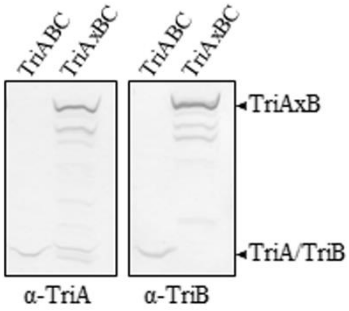

Figure 1.0.2 Expression Analysis of TriABC and TriAxBC
100 µg membrane fractions of GKCW101 cells, producing FhuA under the arabinose promoter, were analyzed by SDS-PAGE. Separated proteins were transferred onto PVDF membranes and analyzed by anti-TriA and anti-TriB immunoblotting.

SDS and triclosan decreased in the presence of this complex (Table 1.0.1). The measured minimal inhibitory concentrations (MICs) were comparable to that of the native, and polyspecific AcrAB.

Table 1.0.1 Antimicrobial Susceptibility of *E. coli* GKCW101 (Δ9FhuA) Producing Plasmid Expressed TriAxBC Variants

	SDS (μg/ml)		Triclosan (ng/ml)	
Variants	0% Arab	0.1% Arab	0% Arab	0.1% Arab
-	9	9	4	4
AcrAB	>2500	312	128	128
TriABC	>2500	312	>128	128
TriAxBC	>2500	156-312	64	64
A_{R130D}xBC	9	9	2-4	2
AxB_{R118D}C	312	78-156.6	64	32-64
A_{G350C}xBC	>2500	156-312.5	128	128
AxB_{G339C}C	19	19	4	8

We found that induction of the FhuA pore production by 0.1% L-arabinose affected the susceptibility to SDS, but not triclosan. The MICs of SDS in cells carrying TriABC encoding plasmids in the absence of FhuA was greater than 2.5 mg/ml, compared to 312 μg/ml when the pore was expressed from the chromosome. These values were 25-35 times higher than MIC of SDS in the efflux null strain. Cells producing TriAxBC were only marginally different in their susceptibility to SDS, in the presence of FhuA expression. The susceptibility of cells carrying the efflux null plasmid did not change in the presence or absence of FhuA. Although for TriAxBC MICs of triclosan was at least two times less than that of cells producing TriABC, neither were affected by the expression (or lack thereof) of the engineered outer membrane pore. MIC of triclosan (TriABC+ and TriAxBC+ cells) were at least 16 time higher than the MIC in efflux null cells. Yet again for the null cells in the presence or absence of FhuA, there was not a difference in MICs of triclosan. Thus, TriABC and TriAxBC are functional in Δ9FhuA cells in the presence and absence of the FhuA pore.

1.2 Nile Red is the Best Probe for Kinetic Studies

We next sought to identify a fluorescent probe, which could report on the efflux activity of the TriC transporter. To investigate and establish the kinetic parameters of the pump in the Δ9FhuA background, we used the fluorescence probes Hoescht 33342 (HT), n-phenyl-naphtylamide (NPN) and Nile Red (NR) in uptake assays to monitor real-time accumulation. Fluorescence of Hoechst would be observed when the probe binds to the target, DNA, within the cell. NPN and Nile Red are both highly fluorescent only when they bind to membrane lipids. Working in *E. coli*, we used AcrAB alongside TriABC as a positive control for the pilot experiments using the Biotek Synergy H1 Hybrid instrument to find optimal set up conditions for the assay. All three fluorescent probes are known to be excellent substrates of AcrAB-TolC [72-74]. Briefly, harvested cells of OD_{600} ~2.0 were washed and resuspended in 50 mM KPO_4^{3-}, 1 mM $MgCl_2$, and 0.4% glucose (PMG), and 100 µl of cells were added to equal volumes of two-fold dilutions of probes in PMG, formerly prepared in black microtiter plates. NPN was excited at 356 nm and emission of light at 460 nm was recorded for 10 minutes (Figure 1.0.3). The same was done for HT and NR which were excited at 355 nm and 552 nm, respectively; emitted light at 460 nm and 636 nm, respectively, were recorded for analysis (Figure 1.0.4 and 5). We found that uptake of the different fluorescence dyes led to different levels of accumulation within the cells; however, kinetic parameters could not be determined. As expected, we note that with all three probes, the efflux proficient cells accumulated less fluorophore than the efflux deficient cells, as indicated by their fluorescence intensities. Comparing the fluorescence intensities within the cells

after 10 minutes of exposure to probes (fourth panel of Figures 1.0.3-5), we find that NPN accumulation in Δ9FhuA (pTriABC) was twice less than efflux null cells unlike cells with AcrAB which reduced accumulation by 5 times (Figure 1.0.3). HT uptake in Δ9FhuA (pTriABC) was similar to efflux null cells, indicating that HT is not a good substrate of TriABC. However, Δ9FhuA (pAcrAB) was able to reduce uptake of HT by 5 times (Figure 1.0.4). In the case of Nile Red, TriABC producing cells decreased the amount of NR in the cells, similar to AcrAB efflux proficient cells (Figure 1.0.5). Due to the comparable efficiencies of AcrAB and TriABC to reduce Nile Red accumulation in the cell, we used this probe for subsequent studies.

1.3 Optimization of Cell Densities for Nile Red Uptake Assays

In order to further optimize the assay and to increase the range of probe concentrations used in the assay, we repeated experiments with different cell densities (Figure 1.0.6). In this experiment we used Δ9FhuA (pAcrAB) and Δ9FhuA (pBSPII). The results showed that at the highest

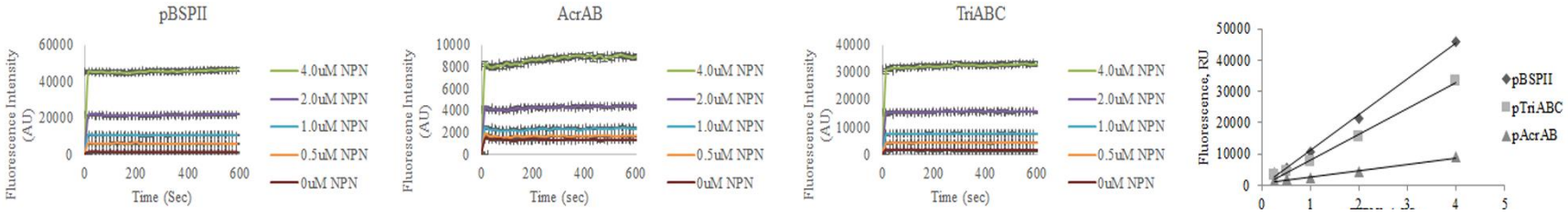

Figure 1.0.3 Fluorescence Uptake Analysis of NPN

Concentration dependent n-phenyl-naphtylamide (NPN) fluorescence uptake *E. coli* Δ9FhuA. Cells were grown to saturation then washed and diluted in the phosphate, magnesium, glucose (PMG) buffer to OD_{600} ~2.0. Equal volumes of cells and dye were mixed and measured for analysis.

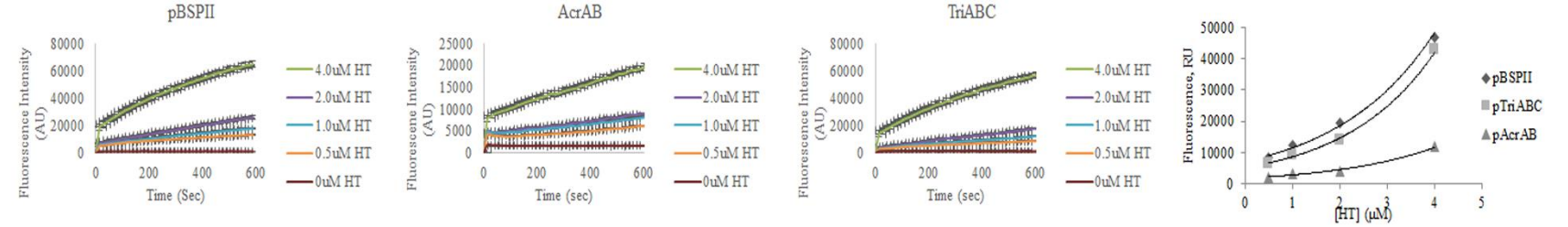

Figure 1.0.4 Fluorescence Uptake Analysis of Hoescht-33342

Hoescht-33342 (HT) concentration dependent fluorescence uptake in *E. coli* Δ9FhuA

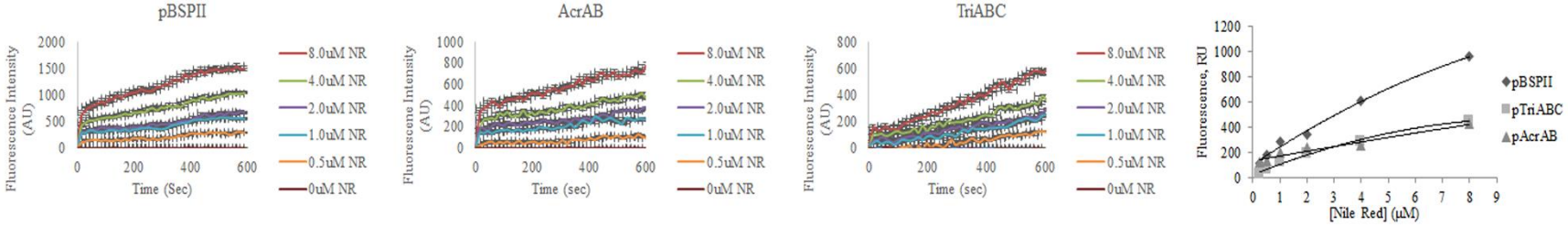

Figure 1.0.5 Fluorescence Uptake Analysis of Nile Red

Nile Red (NR) concentration dependent fluorescence uptake in *E. coli* Δ9FhuA

OD_{600} ~1.0 the signal was the highest but the difference in slopes of Nile Red uptake between efflux null cells and Δ9FhuA (pAcrAB) cells was the smallest. At OD_{600} ~0.1, efflux null cells showed a concentration dependent effect on emitted fluorescence, however, efflux proficient cells showed very low fluorescence signals. Thus the use of cells at OD_{600} ~0.5 was the best – within the range of Nile Red concentrations used, both AcrAB and efflux null cells produced fluorescent intensities above background levels. Cells at this optical density (OD_{600} ~0.5) was used for subsequent experiments. We confirmed the efficiency of AcrAB and TriABC in the Δ9FhuA cells to lower the accumulation of substrate. We also expressed the covalently linked TriAxB, with TriC, and found that is also effective in reducing of intracellular accumulation of Nile Red in the permeabilized cells (data not shown).

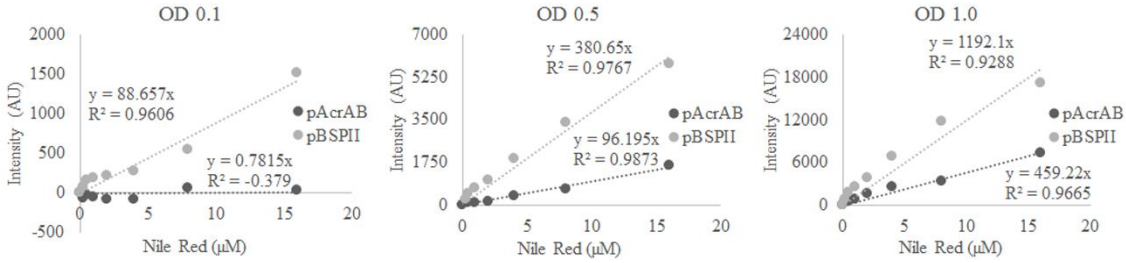

Figure 1.0.6 Calibrating Nile Red Uptake Assay on the TECAN Spark 10M
Cells were grown to OD_{600} >2.0, washed, then diluted in the phosphate, magnesium, glucose (PMG) buffer to OD_{600} ~0.2, 1.0 or 2.0. Equal volumes of cells and Nile Red were mixed and measured for analysis. Cell at 0.1 densities were not effective in showing uptake activities in AcrAB-expressed cells. At OD_{600} ~0.5, plus and minus efflux cells were better visualized, and more separated than at densities of 1.0. The moderate fluorescence intensities also make this the best choice for subsequent experiments.

1.4 There is No Competition Between Nile Red and Triclosan

To investigate the effects of triclosan on NR accumulation and expulsion, we measured uptake of 4 μM Nile Red in the presence of increasing concentrations of triclosan. We observed no difference in NR uptake even at concentrations 8 times

higher than the MIC of triclosan in efflux-null cells (4 ng/ml) (Figure 1.0.7). Results show that there is no competition between triclosan and NR at the binding pockets of TriC prior to efflux from the cells.

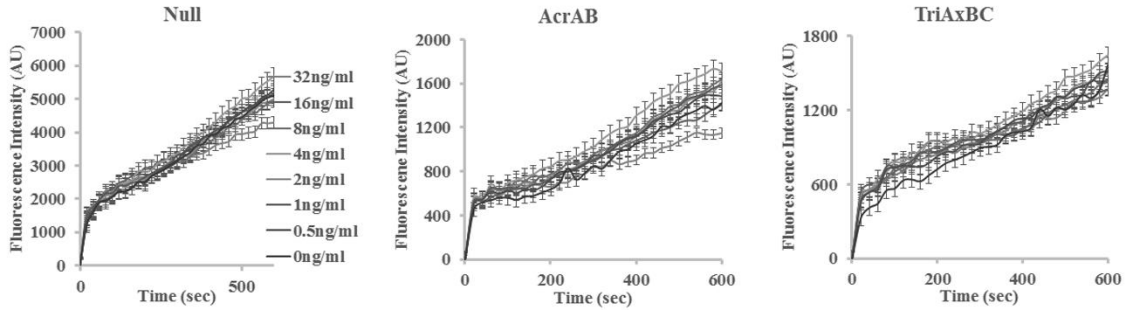

Figure 1.0.7 Triclosan and Nile Red Do Not Compete for Uptake
In the presence of 4 μM NR, a triclosan titration was used to test potential competition between substrate and probe. 2-fold concentration increases of triclosan, exceeding measured MIC of triclosan in efflux null cells, was not sufficient to cause notable changes in uptake of NR.

1.5 TriA and TriB Have Non-Equivalent Roles in TriABC Functionality

Previously, we used unique aspartic acid and cysteine mutations in the coiled-coil and membrane proximal domains, respectively, of TriA and TriB to establish the roles of each MFP within the functional complex (Figure 1.0.1) [33]. Our results suggested that TriA is responsible for the recruitment of the OMP and stabilization of the tetrapartite complex, while TriB is responsible for the interactions with the transporter, TriC. We employ the same mutants within this experiment to characterize how mutations in TriA and TriB within the complex affect efflux activity (Figure 1.0.8). MICs of triclosan and SDS in the Δ9FhuA cells confirmed the importance of $TriA_{R130}$ and $TriB_{G339}$ in the TriABC complex (Table 1.0.1). Cells expressing these mutants were nonfunctional. Comparing the analogous mutants in the partner MFP, $TriA_{G350C}$xBC was fully functional. However, TriAxB_{R118D}C showed up to 4 times lower MICs of SDS in the presence and absence of the FhuA expression; triclosan MICs were the same

as wildtype TriAxBC. Thus, we confirm the role of the conserved arginine in the TriA, but not TriB, coiled-coil domain for complex functionality. Similarly, we show that the membrane proximal mutation $TriB_{G339C,}$ but not $TriA_{G350C}$, affects TriABC efflux proficiency.

1.6 TriA, but not TriB, is Essential for TriABC Efflux of Nile Red

To examine the effects of mutations on complex functionality *in vivo*, TriAxBC variants were used in NR uptake assays. We found that despite the differences between the $TriA_{R130D}$xBC and TriAxB_{R118D}C, as well as $TriA_{G350C}$xBC and TriAxB_{G339C}C mutants in MIC measurements, uptake experiments did not show results consistent with the MIC phenotypes. In agreement with MIC measurements, $TriA_{R130D}$xBC is defective in the efflux of fluorescence probe, Nile Red. TriAxB_{G339C}, however, did not follow the

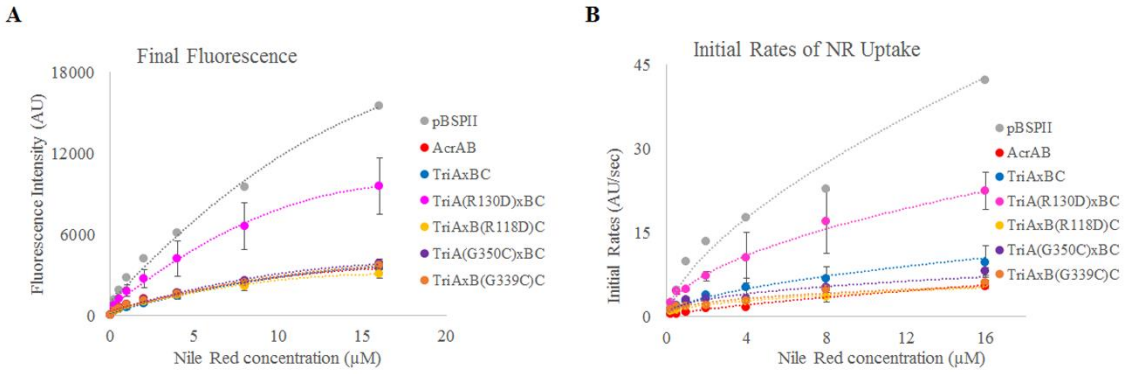

Figure 1.0.8 Nile Red Fluorescence and Rates of Uptake
A. Final fluorescence of NR uptake after 10 minutes exposure to cells. Efflux null cells increasingly acquire NR into the cell as NR concentrations increase. TriAxBC and its functional variants show an ability to efflux NR, reducing amounts of dye within the cell. The same was true for TriAxB_{G339C}C, although MICs showed it to be functional, the cells were efficient in ridding itself of NR. The non-functional mutant $TriA_{R130D}$xBC, however, was less efficient in expelling NR thus showing increased fluorescence, though not the same as efflux null cells. **B.** Initial rates of NR uptake into the cells were calculated using MATLAB. With increased NR concentrations, rates of uptake increased.

same patterns, but rather proved to efficiently efflux Nile Red as the wildtype TriAxBC and other functional mutants (Figure 1.0.8A).

Data was fit using MATLAB, into the equation $y=a_1 + a_2 (1 – e^{-k2x})$, where a_1 is the initial fluorescence intensity of NR, a_2 is the intensity at the end of the desired range of activity, k_2 is the rate of uptake, and x is the initial time. Applying our data to this equation, this yielded initial rates of Nile Red uptake in Δ9FhuA cells expressing TriAxBC and its cysteine and aspartic acid variants. In general, as the concentration of Nile Red increased so did the initial rates of uptake (AU/sec). The pattern of increase suggests that at higher concentrations of Nile Red the rates achieve saturation (Figure 1.0.8B). As was observed with the uptake efficiency, the rates of uptake for cells expressing $TriAxB_{R118D}C$, $TriA_{G350C}xBC$ and $TriAxB_{G339C}C$ were comparable to that of wildtype TriAxBC and AcrAB (Figure 1.0.8B). Initial rates of NR uptake in cells expressing $TriA_{R130D}xBC$ were similar to that of efflux-null cells at low concentrations of NR. However, at concentrations greater than 4 μM NR, the rates of Nile Red accumulation in Δ9FhuA ($pTriA_{R130D}xBC$) cells reduced.

Together, we find that TriA and TriB have different roles in the function of TriABC. The α-helical domain of TriA, but not TriB, is essential for a functional complex. Conversely, the membrane proximal domain of TriB, but not TriA, was essential for resistance to triclosan and SDS. However, we found that the $TriB_{G339C}$ mutant of the MP domain, although non-functional in the expulsion of triclosan and SDS, showed activities similar to wildtype in the efflux of NR. This result indicates that although a loss of function is observed in cells expressing this mutant, the assembly of the complex was not compromised. Having shown the lack of competition between

triclosan and NR, we can conclude that the mechanism of NR efflux is different from that of triclosan though both molecules target cell membrane lipids.

1.7 Association with TolC Changes TriA Conformation

As described in Section 1.5, we established that the non-identical MFPs of TriABC assume different roles within the functional complex. Co-purification results showed that mutations in the coiled-coil domains of TriA and mutations in the membrane proximal domain of TriB abolished interactions with the outer membrane channel protein, TolC [33]. Next, we sought to investigate the conformational state of the TriA/TriB proteins, in the presence and absence of the OMF. For this purpose, we used *in vivo* proteolysis to highlight what is observed in the cells. *P. aeruginosa* GKCW122,

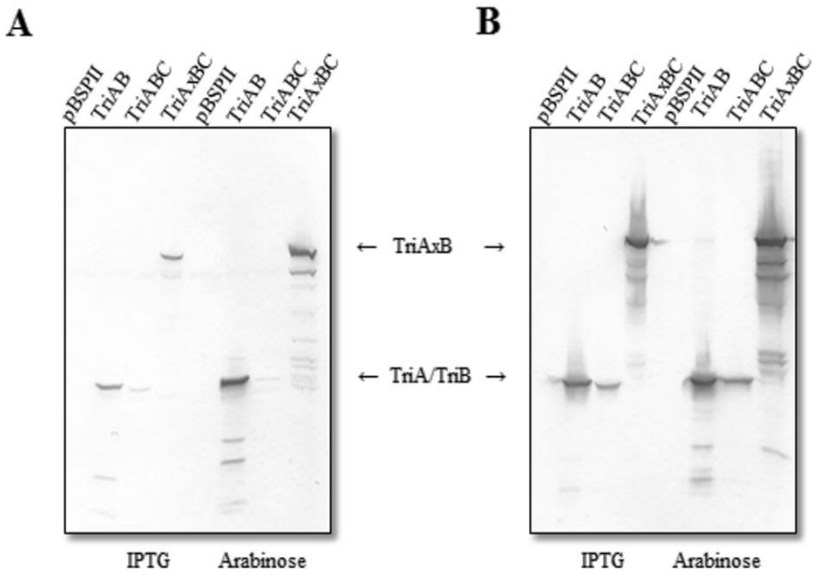

Figure 1.0.9 TriAB, TriABC, TriAxBC Expression in *P. aeruginosa* GKCW122
Whole cell expression of 1e8 cfu cells. Tri proteins were expressed in cells with permeabilized membranes. FhuA expression was dependent on 1 mM isopropyl β-D-1-thiogalactopyranoside (IPTG) or 0.5% L-arabinose induction. Proteins were separated by SDS-PAGE and visualized by A. anti-TriA and B. anti-TriB antibody serum.

a strain lacking six major efflux pumps and with the cell wall permeabilized by the

cork-free FhuA protein, was transformed with TriAB, TriABC and TriAxBC from pBSPII plasmids (Figure 1.0.9*).* In both the independently expressed MFP constructs and the covalently linked variant, TriB showed a higher expression than the TriA counterpart (Figure 1.0.9). In preliminary experiments, we found that smaller amounts of proteins were present when TriAB was expressed in conjunction with FhuA production under isopropyl β-D-1-thiogalactopyranoside (IPTG) control versus the arabinose inducible FhuA expression. Therefore, we used the arabinose-inducible FhuA for pilot experiments.

Cells were grown at 37°C until OD_{600} ~1.0, FhuA expression was induced with 0.5% L-arabinose at OD_{600} ~0.3-0.5, and cells were harvested by centrifugation. Aliquots of cells were treated with trypsin at final concentrations of 0.1, 1.0, 10, and 50 μg/ml. Samples were separated by SDS-PAGE gel electrophoresis and visualized by anti-TriA/B immunoblotting (Figure 1.0.10). In the absence of the TriC pump, TriA

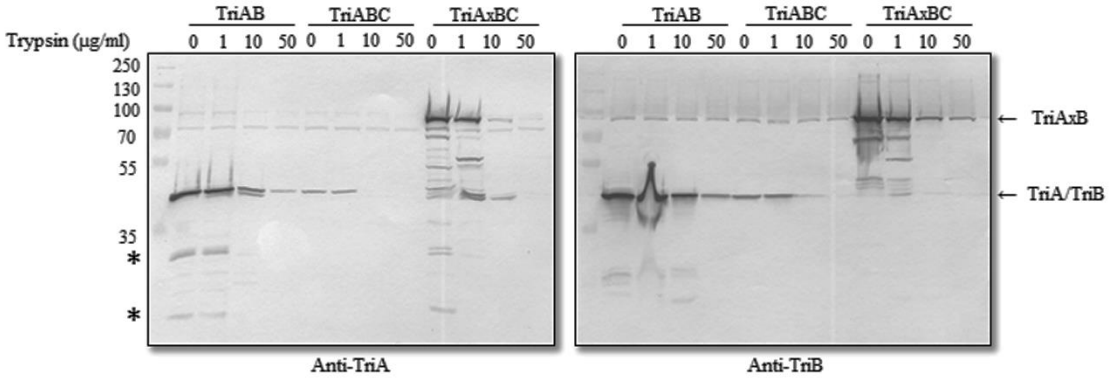

Figure 1.0.10 TriAB, ABC, and AxBC Proteolysis in *P. aeruginosa* GKCW122
In vivo trypsin protease digest of Tri proteins in the presence of cork-free FhuA (under the arabinose promoter).

and TriB proteolytic fragments can be seen in samples treated with up to 10 μg/ml trypsin. Although the amounts of unprocessed TriA and TriB decreased, no digested fragments were observed in samples treated with 50 μg/ml trypsin indicating a faster

processing of the proteins into smaller fragments that cannot be detected. There were no digestion fragments for either MFPs, in the presence of TriC (Figure 1.0.10). This could be due to the lower expression levels of the proteins prior to digestion.

Much like the TriAB construct, TriAxBC digested fragments were only evident in samples treated with 1 and 10 µg/ml trypsin. Neither TriA nor TriB fragments were observed in 50 µg/ml trypsin although the amount of whole length TriAxBC decreased. In samples treated with 1 µg/ml trypsin, we note different digestion profiles of TriA and TriB from the covalently linked construct. TriA digestion showed traces of fragments smaller than the ~40 kDa, the relative size of the individual adapter proteins. An experiment with 0.1 µg/ml trypsin further highlighted these bands (data not shown). The same digest profile was not observed for the TriB.

In order to better cross examine the conformations of the TriAB proteins, when in assembly with TriC, the proteins were expressed in GKCW102 (Δ*tolC fhuA*+) and GKCW104 (*tolC*+ *fhuA*+) (data not shown). Proteins were expressed from pBAD33-TriABC (± pBAD-TriC$_{His}$). As previously discussed [33], TriC expression is not observed in this background thus the pBAD-TriC$_{His}$ was used to supplement production of the transporter protein when needed. Using the above proteolysis protocol, *in vivo* TriAB digest was analyzed in the presence and absence of TriC and TolC. Purified TriABC and TriAxBC proteins were also analyzed for comparison (Figure 1.0.11). Proteins were treated with 0.1, 1.0, and 10 µg/ml trypsin. As shown on Figure 1.0.11A, TriA was susceptible to digestion by trypsin in the absence of TriC, regardless of the presence or absence of TolC (Figure 1.0.11A). TriB, however, was protected from protease activity in either cases (Figure 1.0.11B). In the presence of the TriC pump, TriA digest was

partially protected when TolC was not present (Figure 1.0.11C). The opposite was true for TriB. Though it was now subject to digest, unlike in the absence of TriC, the presence of TolC ever so slightly protected the protein from the effects of trypsin (Figure 1.0.11D).

In vitro proteolysis of TriABC showed that TriA, but not TriB, was hydrolyzed (Figure 1.0.11A, B). The same was true for the fused TriAxBC. Treating the proteins

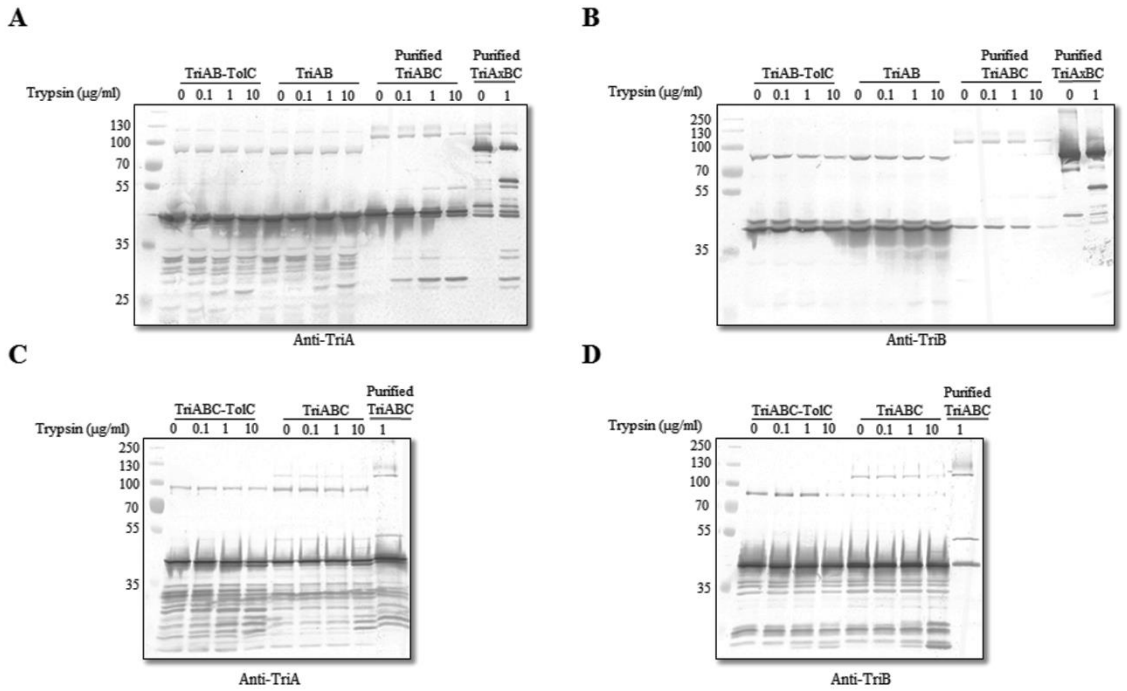

Figure 1.0.11 Proteolytic Profiles of TriAB
Whole cells (GKCW102 and GKCW104) expressing TriAB and purified TriABC and AxBC were treated with increasing concentrations of trypsin. TriA (**A**) and TriB (**B**) fragments were visualized by anti-TriA and anti-TriB antibody immunoblotting, respectively. **C.** TriA and **D**. TriB fragments of GKCW102 and GKCW104 cells expressing TriABC were resolved by immunoblotting

with 1 µg/ml trypsin, TriA was showed more fragments in its profile while TriB did not show any digest small than ~40 kDa. This is consistent with in the *in vivo* studies, proving that TriB has a different folding and conformation than its partner, protecting it from digest even in the TriAxB fused construct

AcrA Arg 128 is a conserved residue that affects the function of AcrAB-TolC [71]. We introduced an aspartic acid mutant at the analogous positions in TriA and TriB (Figure 1.0.1), and found that the conserved amino acid in TriA but not TriB, is essential in the TriABC-TolC complex [33]. Using proteolysis, we wanted to find out the effects of the point mutation on the protein conformation in the presence and absence of TriC and TolC. Using the same procedure as before, mutants were treated with trypsin in the presence and absence of OMF TolC. $TriA_{R130D}$, co-expressed with TriB and TriC, was digested by trypsin when the channel protein was not expressed, more so than wildtype TriABC (Figure 1.0.12A, upper panel). In the presence of TolC, increased trypsin concentration did not yield as many fragments as $TriA_{R130D}BC$ alone. This showed a protection of TriA by the TolC. This avoidance of digestion was observed in the TriB proteins that were co-expressed with $TriA_{R130D}$ and TriC. The expression, or lack thereof, of TolC did not change this TriB digest profile (Figure 1.0.12A, lower panel). $TriAB_{R118D}C$ showed similar results. In the presence of TolC, TriA was still protected from digestion by trypsin (Figure 1.0.12B, upper panel). However, though it is vulnerable to processing, TriA in $TriAB_{R118D}C$ showed a different profile than

wildtype TriABC. TriB, in $TriAB_{R118D}C$, also shows less susceptibility to trypsin digest

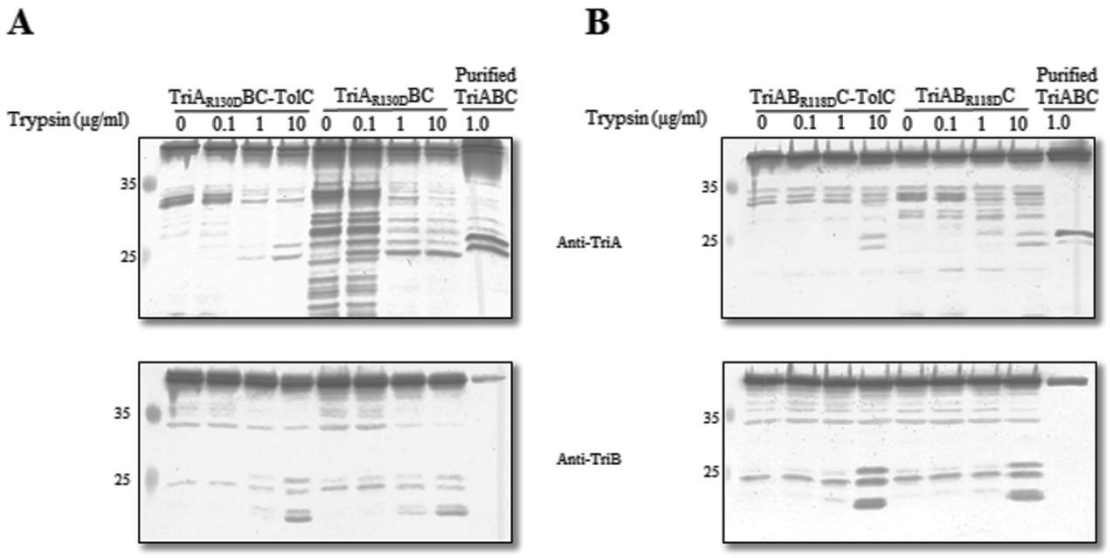

Figure 1.0.12 Proteolytic Profiles of TriAB in Aspartic Acid Variants of the Coiled-Coil Domain
A. TriA and TriB fragments of TolC plus and minus cells producing $TriA_{R130D}$ mutants.
B. Same as A for cells producing $TriB_{R118D}$ mutants

in the presence and absence of TolC (Figure 1.0.12B, lower panel). Aside the change in profile of TriB in the presence of the $TriA_{R130D}BC$ and $TriAB_{R118D}C$ coiled-coil mutants versus in the wildtype, the overall lack of difference in degradation profile further confirms that the TriB accessibility to trypsin is independent of the presence of TolC. Our results suggest that TriA interactions with TolC change the MFP conformation – digestion profiles changed in the presence or absence of TolC. However, TriB conformations did not change in the presence or absence of the channel protein.

In the similar experiments with the point mutations in the membrane proximal domains – $TriA_{G350C}BC$ and $TriAB_{G339C}C$ – we find that once again the overall digest profile of TriA and TriB differed one from the other. In experiments with cells expressing $TriA_{G350C}BC$-TolC, TriA was highly susceptible to protease cleavage (Figure 1.0.13A, upper panel) but TriB was not as sensitive (Figure 1.0.13A, lower

panel). Without the TolC channel protein, TriA and TriB were both less sensitive to cleavage (Figure 1.0.13A). In cells expressing $TriAB_{G339C}C$-TolC, TriA was slightly less susceptible to protease than wildtype (Figure 1.0.13B, upper panel). Without TolC,

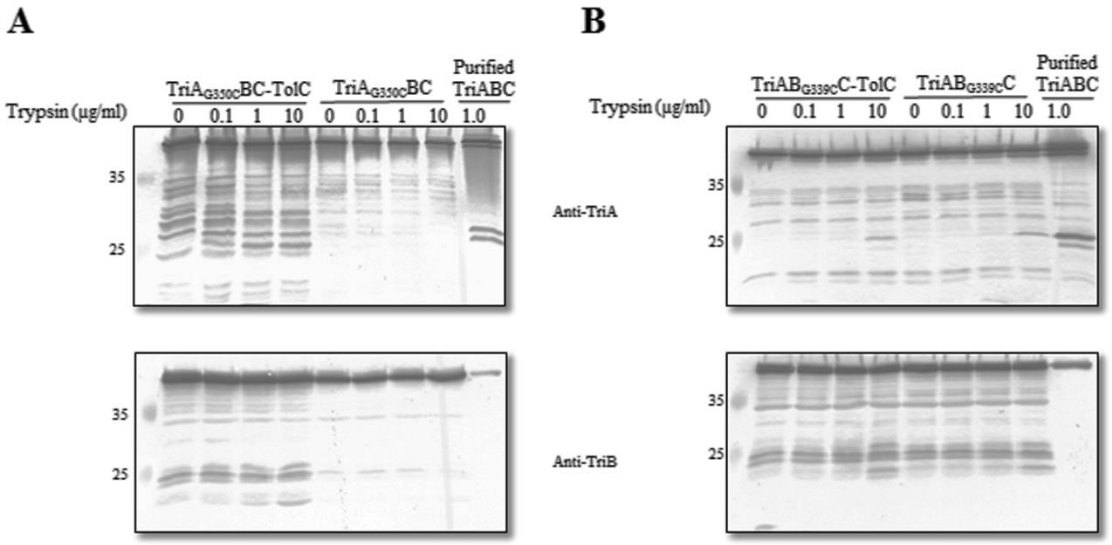

Figure 1.0.13 Proteolytic Profiles of TriAB in Cysteine Variants of the Membrane Proximal Domain
A. TriA and TriB fragments of TolC plus and minus cells producing $TriA_{G350C}$ mutants.
B. Same as A for cells producing $TriB_{G339C}$ mutants

however, the TriA proteolytic profile was the same as wildtype. TriB was the same as the wildtype, even in the absence of TolC (Figure 1.0.13B, lower panel). Once again we note that the TriB protein, which is more essential for interactions with the transporter TriC, is subject to trypsin digest regardless of TolC expression. The exception was with $TriA_{G350C}BC$ expression without TolC. TriA, however, was affected by the presence or absence of TolC (Figure 1.0.13B, upper panel). Also, the digest profiles were different in the essential and non-essential mutant backgrounds, indicating different conformations of TriA.

Taken together, we show that TriA and TriB proteins assume independent, non-equivalent roles within the bacterial cell. The α-helical domain of TriA helps stabilize

interactions with the OMP, while the TriB membrane proximal stabilizes interactions with TriC. TriA proves to be important in the complex activity – as seen from the MIC measurements and efflux of Nile Red. However, we find that although the essential amino acid in TriA (TriAR130) changes complex functionality, it does not affect assembly – rates of NR uptake were lower that efflux null cells, indicating the presence of an assembled, partially active complex in the cell. Protease digest results also differentiate the MFPs. TriA and TriB differ in conformations, however, the TriA protein changes conformation in the presence and absence of TolC. This data supports the role of TriA as the stabilizer of the complex with the OMP, but also presents this protein as the one responsible for the recruitment of the OMF protein.

Chapter 2. Investigation of TriAB Interactions and Mechanism of Opening the Channel Protein

The unique TriABC-OpmH efflux pump of *Pseudomonas aeruginosa* provides a powerful model by which mechanisms of efflux pumps can be studied. Unlike previously studied efflux pump systems, there are two different MFPs in this complex [33, 49]. As we described above, TriA and TriB have two distinct roles within the complex with TolC (Figure 2.0.1) and its *P. aeruginosa* homolog OpmH. TriA is essential for stabilization of the complex and interactions with TolC/OpmH, while TriB is important for interactions with the transporter, TriC [33]. In either cases, we had yet to assign the interfaces of OMF-MFP or MFP-IMP interactions. In this study, we used disulfide bonding to position TriA and TriB on OpmH, as would be seen in the functional complex. Aside showing a symmetric arrangement of the MFPs in complex, we assign the TriB protein the responsibility of the opening of the outer membrane protein, OpmH.

2.1 OpmH is an Essential Protein of Efflux-Deficient *P. aeruginosa*.

TriABC-OpmH efflux complex is functional in the strain PAO1116 (Δ*mexAB-oprM* Δ*mexCD-oprJ* Δ*mexEF-oprN* Δ*mexJK* Δ*mexXY* Δ*triABC*) lacking six efflux pumps [33]. The deleted *triABC* genes were supplemented by the expression of the proteins from a plasmid, in order to complement the chromosomally expressed OpmH. In order to purify and identify the OMF protein, a 6-Histidine tag was added to the OpmH protein sequence. At the same time, we sought to move the *opmH* gene into a different position on the chromosome and bring it under a promoter control (Section

II.1.1). We used the *att*Tn7 site for insertion onto the chromosome and brought the *opmH* gene under control of the arabinose-inducible promoter. In this process, we found that deletion of the original *opmH* could not be achieved lest we have the second copy integrated at the *att*Tn7 site. As shown on Figure 2.0.2, the *P. aeruginosa* JWW9

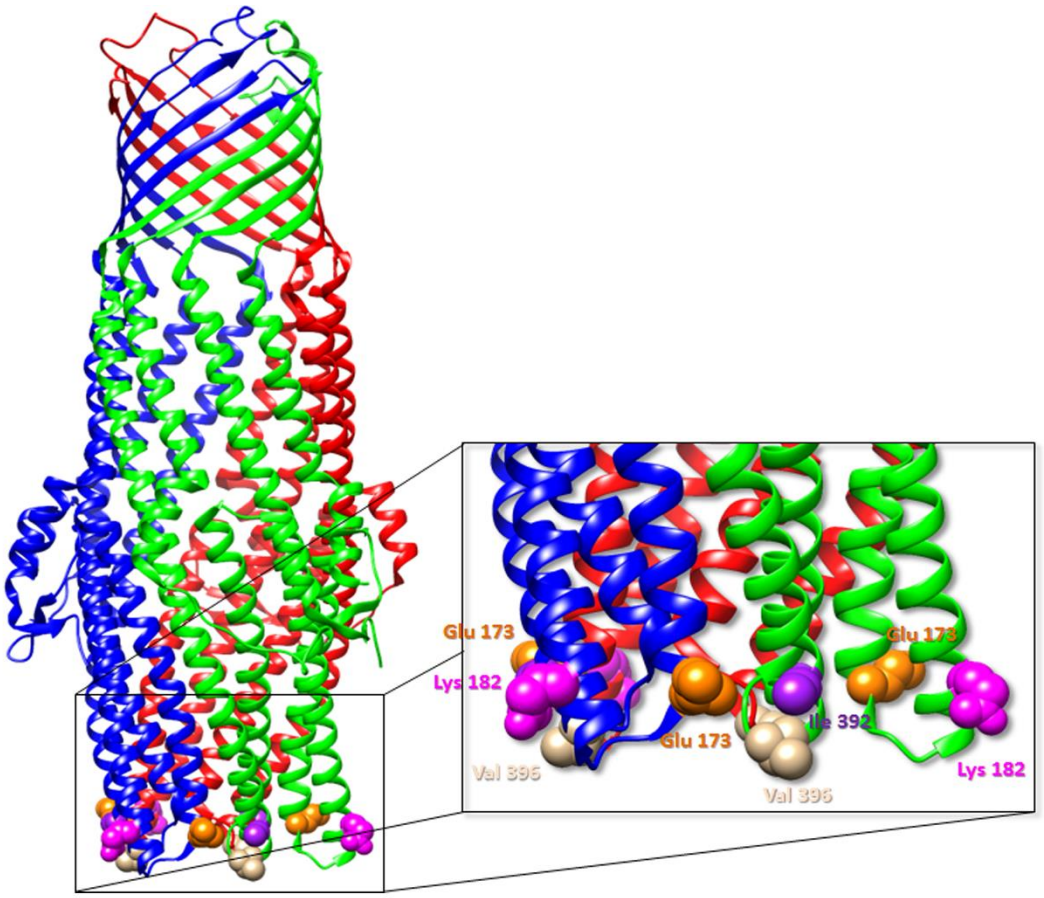

Figure 2.0.1 TolC Crystal Structure
The trimeric TolC crystal structure (PDB code: 1EK9) with the corresponding OpmH Glu 173 and Lys 183 mutation of loop 1, and Ile 392 and Val 396 of the inclined helices marked in varying colors. Labeled mutations are the correlating amino acids in the TolC structure.

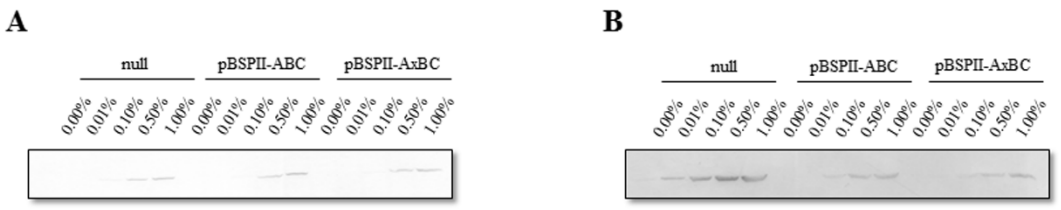

Figure 2.0.2 Arabinose Concentration-Dependent OpmH Expression
Overnight cultures of OpmH cells were reinoculated in varying concentrations of LB-arabinose and allowed to grow to OD_{600} ~1.0. **A.** $1x10^8$ cfu of whole cells and **B.** 100 ng of membranes were separated by SDS-PAGE electrophoresis. Samples were transferred on PVDF membranes and visualized by immunoblotting using anti-His antibody.

strain produced $OpmH_{His}$ upon induction with L-arabinose and the protein production was dependent on the concentration of arabinose used (Figure 2.0.2).

Overnight cultures of JWW9 cells with plasmid encoded TriABC or the covalently linked TriAxBC [33] in LB with 100 μg/ml carbenicillin and 1% L-arabinose were washed and reinoculated into fresh LB supplemented with 100 μg/ml carbenicillin, and varying amounts of arabinose and allowed to grow. After 5 hours of incubation cells were used to test the antibiotic susceptibility, as well as to check the amount of protein production. We found that MICs of triclosan and SDS increased as arabinose concentrations increased (Table 2.0.1). However, MICs for SDS reached a plateau at 0.1% arabinose, while that of triclosan plateaued at 0.5% arabinose. Under the same conditions, whole cells and membrane fractions were examined by immunoblotting with anti-His antibodies (Figure 2.0.2). In the whole cell, $OpmH_{His}$ was not detected until 0.5% arabinose was used to protein expression (Figure 2.0.2A). In the membrane fractions, however, the expression of OpmH depended on whether or not TriABC was also present (Figure 2.0.2B). When OpmH was expressed alone,

0.01% arabinose was sufficient to see the protein. In the presence of TriABC or TriAxBC, traces of OpmH was first detected upon induction with 0.1% arabinose.

Table 2.0.1 Arabinose-Dependent Antimicrobial Susceptibility of *P. aeruginosa* JWW9 (PAO1116 attTn7::ParaBAD-opmH$_{His}$) Producing Indicated Tri Complexes.
(SDS and Triclosan concentrations are in µg/ml)

	0% Arab		0.01% Arab		0.1% Arab		0.5% Arab		1.0% Arab	
	SDS	Triclosan	SDS	Triclosan	SDS	Triclosan	SDS	Triclosan	SDS	Triclosan
pBSPII	19	2-4	19	4	78	16	312	32	312	32
pBSPII-ABC	312-625	16-32	625-1250	16-32	2500+	32	>2500	64	>2500	64
pBSPII-AxBC	312	16	625	16	>2500	32	>2500	>128	>2500	>128

Considering the overall levels of OpmH was lower, it could be reasoned that the presence of TriABC regulates the amount of OpmH present within the cell.

2.2 OpmH Cysteine Variants Are Functional and Assemble into Complexes with TriABC

To identify and study the OMF-MFP interface interactions, we introduced unique cysteines into the OpmH proteins. Sites subjected to the mutagenesis were based on computational analysis using the GREMLIN web server [75, 76]. OpmH amino acid residues Glu 173, Lys 182, Ile 392, and Val 396 (Figure 2.0.1) were predicted to interact with certain TriA and TriB side chain residues at probabilities greater than 90%. Like the wildtype protein, OpmH cysteine variants were not easily integrated onto the chromosome at the *att*Tn7 site lest the original gene was first present then deleted after successful insertion of the mutant. We introduced cysteine mutations pTJ1-opmH. PCR and sequencing were performed to confirm the native *opmH* gene had been deleted and that the *opmH* cysteine mutant gene was present under the control of the arabinose promoter. DNA sequencing showed that aside OpmH$_{V396C}$, integration of the cysteine

OpmH variants was successful. $OpmH_{V396C}$ proved to be the wildtype OpmH without the intended cysteine mutation. In fact, it was the only construct which continually evaded selection post mating; we repeatedly selected for the wildtype/$OpmH_{V396C}$ diploid or a wildtype OpmH at the *att*Tn7 site. Thus we concluded that $OpmH_{V396C}$ is a non-functional mutant. Since OpmH is essential for the cell, wildtype OpmH could not be deleted off the chromosome and replaced by a non-functional construct. This also indicates the importance of the Val 396 amino acid for a functional TriABC-OpmH complex.

We next analyzed the functional phenotype of the remaining mutants by measuring MICs of triclosan and SDS and found that all cysteine variants showed the same phenotype as wildtype OpmH (Table 2.0.2).

Table 2.0.2 Antimicrobial Susceptibility of JWW9 ($OpmH_{His}$) Cysteine Variants Containing the Plasmid Encoded TriABC
(SDS and Triclosan concentrations are in µg/ml)

	null		TriABC		TriAxBC	
Variants	SDS	Triclosan	SDS	Triclosan	SDS	Triclosan
OpmH	156.6-312.5	16-32	>2500	>128	>2500	>128
$OpmH_{E173C}$	156.6	32	>2500	>128	>2500	>128
$OpmH_{K182C}$	156.6	16	>2500	>128	>2500	>128
$OpmH_{I392C}$	156.6	16	>2500	>128	>2500	>128

Using co-purification studies, we determined whether the OpmH-Cys mutants assemble the complete TriABC-OpmH complex. For this purpose, $OpmH_{His}$ and its cysteine variants were co-expressed with the plasmid-borne TriABC or TriAxBC. We purified $OpmH_{His}$ using Cu-NTA affinity chromatography and equal amounts of

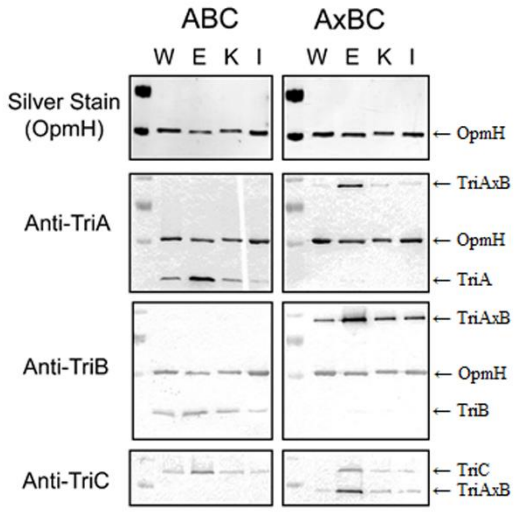

Figure 2.0.3 OpmH Cysteine Variants Assemble in Complex with TriABC
Immunoblotting analysis of 100 ng $OpmH_{His}$ variants (shown by silver staining) purified from cells producing TriABC or TriAxBC complexes. Co-purification of TriA, TriB, and TriC with $OpmH_{His}$ (W), $OpmH_{E173C\text{-}His}$ (E), $OpmH_{K182C\text{-}His}$ (K), or $OpmH_{I392C\text{-}His}$ (I), were detected by immunoblotting with anti-TriA, anti-TriB, and anti-TriC antibodies respectively.

wildtype and mutant proteins were separated by SDS-PAGE gel electrophoresis.

We found that TriA, TriB, and TriC were all copurified with wildtype OpmH and its cysteine variants. Amounts of protein pulled down were fairly equivalent, save the $OpmH_{E173C}$ mutant which more strongly bound TriABC and TriAxBC (Figure 2.0.3). Located at the tip of the first loop (α-helices 3 and 4) of OpmH, with its amino acid side chain facing the interprotomer groove, the higher levels of TriABC association with $OpmH_{E173C}$ foreshadows a highly stable complex formation with this mutant. Thus, substitution at the interprotomer groove is important for the complex stabilization as H3-H4 interacts with the TriA/TriB membrane fusion proteins.

2.3 TriA and TriB Cysteine Variants Are Expressed and Functional

Based on the Gremlin web server analysis, three TriA and three TriB amino acid residues were identified as putative interacting partners of OpmH at the sites discussed above (Figure 2.0.4). In TriA, Ala 134, Lys 138, and Gly 139 were predicted to interact



Figure 2.0.5 TriA and TriB Cysteine Variants Are Expressed
Immunoblotting analysis of membrane fractions isolated from JWW9 cells producing indicated TriABC complexes and their variants. 100 ng of total membrane proteins were separated by SDS-PAGE and analyzed by immunoblotting with anti-TriA or anti-TriC antibodies.

with the OpmH residues at greater than 90% probability. The equivalent TriB residues are Glu 122, Arg 126, and Ser 127. All six of these residues are found at either the

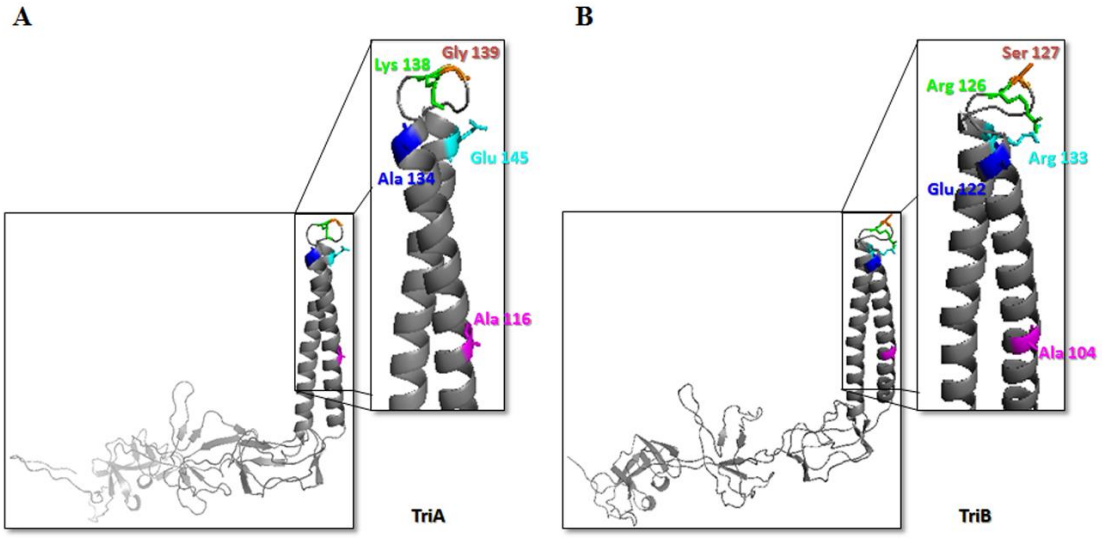

Figure 2.0.4 TriA and TriB Cysteine Mutants
Modeled structures of TriA (**A**) and TriB (**B**) based on the crystal structure of MexA (PDB code: 2V4D) with highlighted amino acids used in crosslinking studies. Residues were based on Gremlin web server analysis, and the equivalent mutants in TriA and TriB are noted in the same color.

higher end of the coiled-coil domain of the MFPs or in the loop between the two α-helical segments (Figure 2.0.4).

Using site directed mutagenesis, we introduced the desired cysteine residues into the covalently linked TriAxB [33] per the manufacturer's manual. Using isolated cell membranes, protein expression was assessed. We found that TriAxBC mutants were expressed at similar levels as the wildtype (Figure 2.0.5). Once again, we analyzed the phenotypic effects of the engineered cysteines on the complex functionality. We found that none of the mutants affected the cell's susceptibility to SDS or triclosan (Table 2.0.3).

Table 2.0.3 TriAxBC Cysteine-Containing Mutants Are Functional
Relative antimicrobial susceptibility of *P. aeruginosa* JWW9 ($OpmH_{His}$) producing TriAxBC cysteine variants with mutations in the coiled coil domain

Variants	SDS	Triclosan
AxBC	>8	>4
A_{A116C}xBC	>8	>4
A_{A134C}xBC	>8	4
A_{K138C}xBC	>8	4
A_{G139C}xBC	>8	4
A_{E145C}xBC	>16	4
AxB_{A104C}C	>8	>4
AxB_{E122C}C	>8	4
AxB_{R126C}C	>8	4
AxB_{S127C}C	>8	4
AxB_{R133C}C	>8	>4

Using the results of the AcrA-TolC crosslinking studies [23], we engineered two more cysteine residues to test the specificity of protein-protein interactions within the complex. $TriA_{A116C}$xB and $TriAxB_{A104C}$, located midway of the first coiled-coil helix of the respective MFP, as well as $TriA_{E145C}$xB and $TriAxB_{R133C}$, positioned nearby the tip of the coiled-coil domains were used as controls (Figure 2.0.4). All control mutants

were expressed (data not shown) and fully functional compared to the wildtype (Table 2.0.3).

2.4 $OpmH_{E173C}$, $OpmH_{K182C}$, and $OpmH_{I392C}$ Form Disulfide Bonds with Both TriA and TriB

We next sought to determine and assemble there OpmH-TriA/B interface interactions. We co-expressed OpmH cysteine variants, on the chromosome, with each of the TriA and TriB cysteine mutants (expressed from plasmids) to observe spontaneous disulfide bonding. Equal amounts of total membrane proteins were analyzed by SDS-PAGE gel electrophoresis and visualized by immunoblotting using anti-TriB or anti-His antibody serum to visualize (Figure 2.0.6).

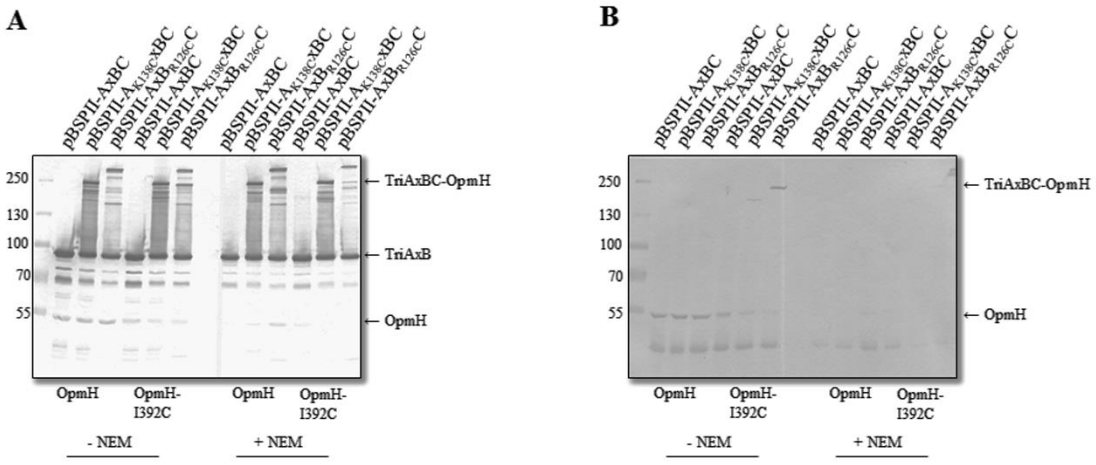

Figure 2.0.6 TriAxBC and OpmH Cysteine Mutants Form Spontaneous Disulfide Wildtype OpmH and $OpmH_{I392C}$ were individually co-expressed with pTriAxBC cysteine mutants. One set of cells was pretreated with NEM prior to cell lysis. 10 μg of membrane proteins were separated by SDS-PAGE and immunoblotting was used to identify protein bands. Cross-examining anti-TriB (**A**) and anti-His (**B**) immunoblots confirmed disulfide formation between cysteines.

In the subsequent experiments, all cells were treated with 5 mM NEM and incubated for 5 minutes. We were better able to identify high molecular bands with the His-tagged OpmH. Superimposing the results of crosslinking visualized with anti-TriB and anti-

His antibodies, we found that the high molecular band seen in the anti-His westerns are also present in the anti-TriB gels, confirming the complex formation of TriAxB with

Table 2.0.4 MICs of Select OpmH Cysteine Mutants Co-Expressed with TriAxBC Cysteine Variants
(SDS and Triclosan concentrations are in μg/ml)

	SDS	Triclosan
OpmH - pBSPII	312.5	16-32
OpmH - pBSPII-AxBC	>2500	>128
$OpmH_{E173C}$: pBSPII-A_{K138C}xBC	>2500	>128
$OpmH_{I392C}$: pBSPII-A_{A134C}xBC	>2500	>128
$OpmH_{I392C}$: pBSPII-AxB_{R126C}C	>2500	>128

OpmH (data not shown). Cysteine pairs that showed spontaneous disulfide formation were further analyzed for potential toxicity to the cell as well as for the effects on the cell's susceptibility to triclosan and SDS. Results show that disulfide formation does not affect the functionality of the TriAxBC-OpmH efflux pump (Table 2.0.4).

Immunoblotting analysis of the full set of TriA/B mutants – the predicted positions, as well as the chosen controls – interacting with OpmH showed that

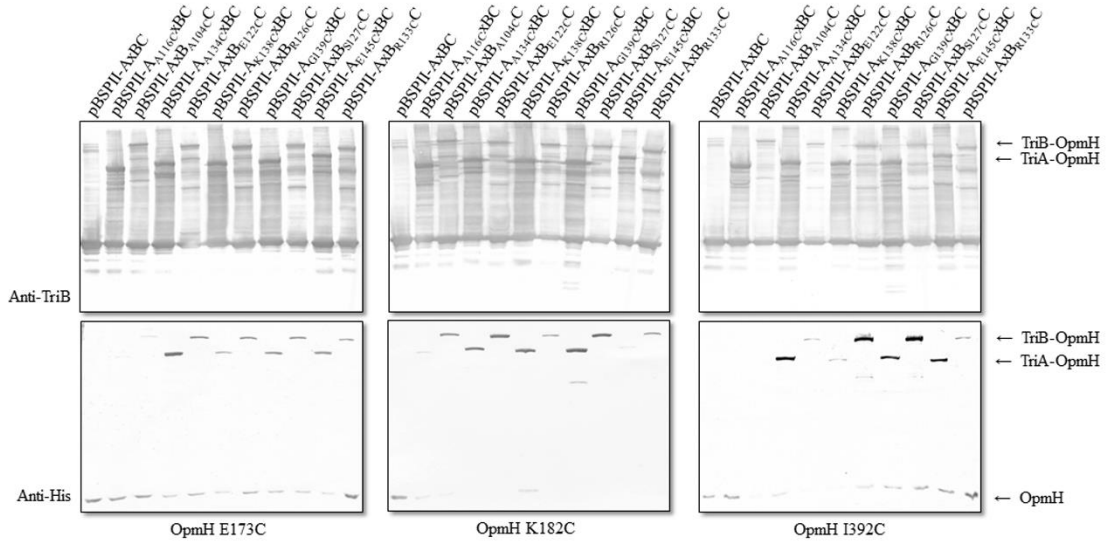

Figure 2.0.7 OpmH Cysteine Variants Form Bonds with Both TriA and TriB
Cysteine variants of TriA and TriB were co-expressed with OpmH cysteine strains in the presence of 1% L-arabinose. Pretreated with 5 mM NEM, cell membranes were harvested and 10 μg of total membrane proteins were separated by SDS-PAGE electrophoresis. Immunoblotting with anti-TriB and anti-His antibodies show binding of OpmH mutants to both MFPs of the efflux complex.

$OpmH_{E173C}$, $OpmH_{K182C}$, and $OpmH_{I392C}$ formed disulfide bonds to both the TriA and TriB proteins at the correlating positions (Figure 2.0.7). As shown on Figure 2.0.6, the mobility of TriA-OpmH differed from that of TriB-OpmH. Using the results of three independent experiments, we quantified the intensities of visualized bands from the

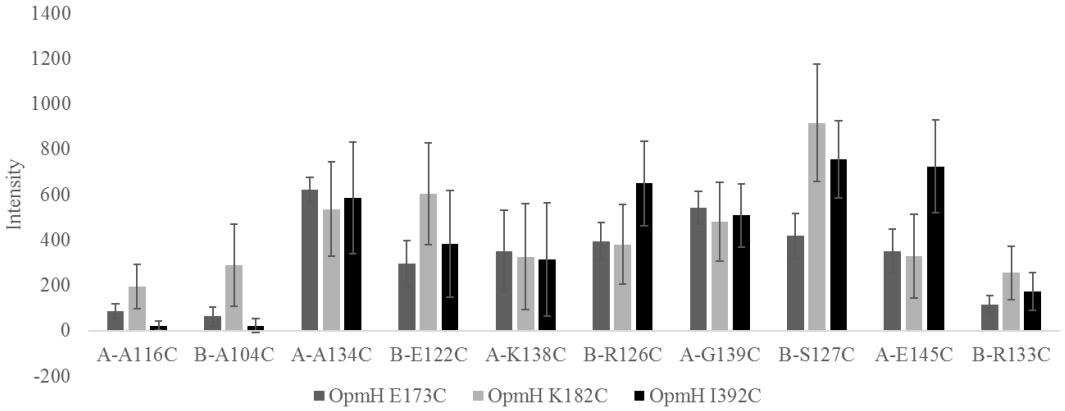

Figure 2.0.8 Quantified of TriAxB-OpmH Disulfide Bonding
Immunoblot results of three independent spontaneous disulfide bond formation experiments were compiled and analyzed. Anti-His westerns were scanned and bands were quantified using BioRad's Quantity One.

anti-His developed immunoblots (Figure 2.0.8). Determining the ratios of TriA/B bound to OpmH, we assigned the preferred MFP mutant at each OpmH cysteine location (Table 2.0.5).

$OpmH_{E173C}$ showed preferred binding to TriA, the most significant (greater than 95% confidence level) with $TriA_{A134C}$xBC and $TriA_{E145C}$xBC. These mutants showed preferred interactions with $OpmH_{E173C}$ 2 and 3 times, respectively, more than

Table 2.0.5 OpmH Cysteines Show Preference for TriABC Bonding

*p-Value <0.05 **p-Value <0.1

OpmH E173C		OpmH K182C		OpmH I392C	
A-A116C	1.36	B-A104C	1.48	B-A104C	1.04
A-A134C	2.08*	B-E122C	1.12	A-A134C	1.52
B-R126C	1.12	B-R126C	1.16	B-R126C	2.06
A-G139C	1.29	B-S127C	1.90*	B-S127C	1.49**
A-E145C	3.01*	A-E145C	1.29	A-E145C	4.17*

complexes with analogous cysteine substitutions in TriB. $OpmH_{K182C}$ favored binding to TriB, but most significantly with $TriAxB_{S127C}C$ which was twice more favored than the corresponding mutant in TriA ($TriA_{G139C}xBC$). $OpmH_{I392C}$ did not show a clear inclination of binding to TriA or TriB, however, the most significant pairing came from the control position at TriA Glu 145. Of the predicted amino acid sites, TriB Ser 127 showed significant binding to $OpmH_{I392C}$, but it was within 90% confidence (Table 2.0.5).

Based on these results, we can conclude that $OpmH_{E173}$ which is located on the H3-H4 pair of the OMF exclusively prefers interactions with TriA. Facing the intraprotomer groove of the protein, $OpmH_{K182C}$ also has a strong preference to TriB of the TriAxB construct. However, located on the second, dynamic helical loop of OpmH, and also facing the intraprotomer groove, we find that Ile 392 can interact with either TriA or TriB. Putting these together, we find that although the TriAxB-OpmH complex can assemble in a symmetric fashion, as would be expected, it is also capable of

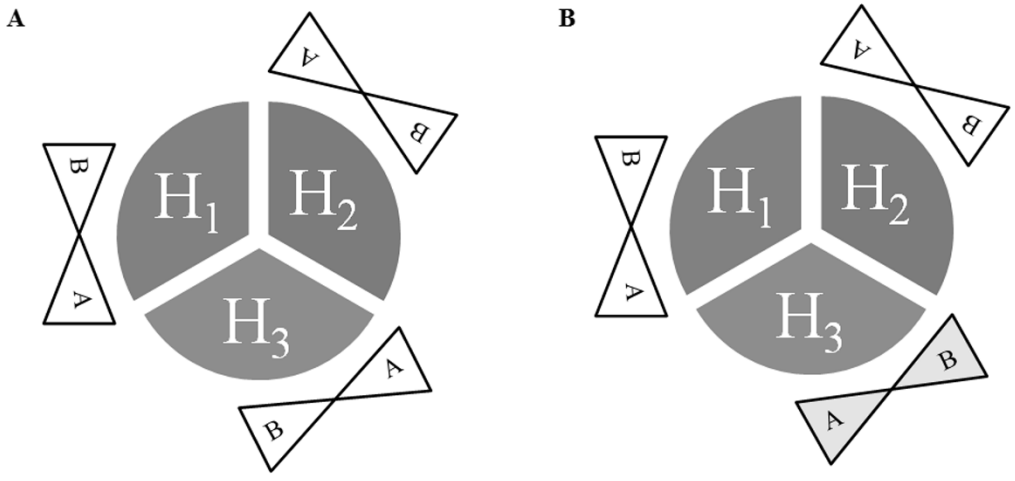

Figure 2.0.9 TriAB-OpmH Assembly Models
A. TriAB assembled in the expected, symmetrical arrangement about the outer membrane protein, OpmH. **B**. Based on our crosslinking studies, at least one inter-protomer groove is occupied by TriB thus presenting an asymmetric assembly of proteins.

arranging itself asymmetrically (Figure 2.0.9). However, due to the non-equivalent roles of TriA and TriB, as well as the covalently linked TriAxB, the asymmetric assembly is unlikely.

2.5 TriB Opens the OpmH Channel Aperture

Salt bridge interactions at the periplasmic end of OMFs have been found to render these channel proteins closed in the resting state [7]. Based on the structure similarities to TolC, we conclude that in the case of OpmH there is also a dilation of the

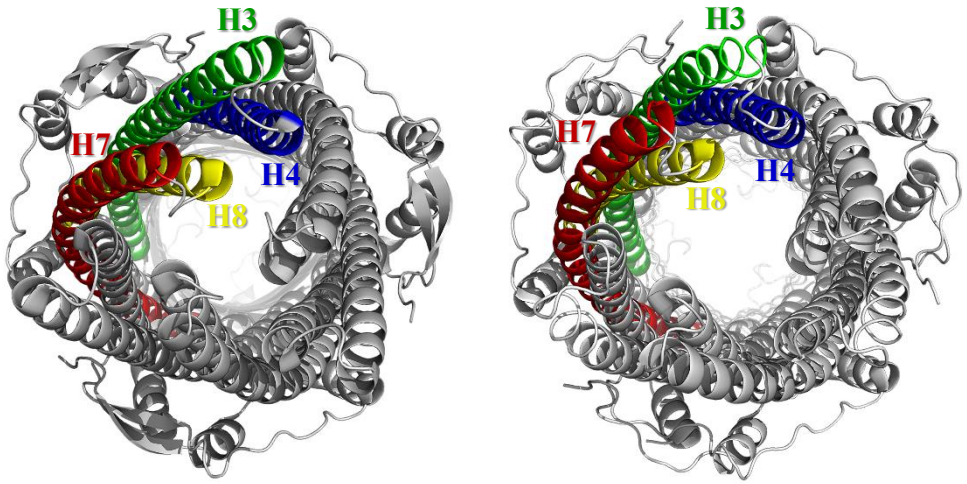

Figure 2.0.10 Closed and Open Conformations of the TolC Periplasmic Aperture Bottom view of the outer membrane channel protein. The α-helices of loop 1 (H3 and H4) and lop 2 (H7 and H8) are indicated in both structural conformations.

α-helices of the periplasmic barrel to open the protein for substrate extrusion [77] (Figure 2.0.10). To test this, we analyzed the cysteine mutants of TriA and TriB in pairs with OpmH cysteines in azithromycin susceptibility assays. Bacterial lawns of cells with combinations of cysteine mutants were spotted with azithromycin and grown overnight. If mutations in the plasmid-borne TriAB dilate the periplasmic aperture of OpmH, expressed on the chromosome, the zone of inhibition will increase in comparison to

wildtype OpmH-wildtype TriABC interactions. We used azithromycin instead of vancomycin because the parental PAO1116 strain is sensitive to the macrolide azithromycin but is resistant to vancomycin (unpublished data). Zones of inhibition were measured in mm and the averages of three independent experiments are reported (Figure 2.0.11). We used wildtype OpmH in combination with the TriA or TriB cysteine mutants as well as the combinations of $OpmH_{Cys}$ with the TriAxB mutants. Further analysis of the results by t-tests determined the significance of measured zones, comparing all samples to the wildtype TriAxBC-OpmH combination.

We found that of the TriAxB cysteine mutants, $TriA_{G139C}$ had a significantly decreased zone of inhibition of azithromycin compared to the wildtype pair. When expressed in conjunction with $OpmH_{E173C}$, we found that $TriAxB_{R126C}$ allowed the cell to increase its susceptibility to azithromycin. In the case of $OpmH_{K182C}$, it was the

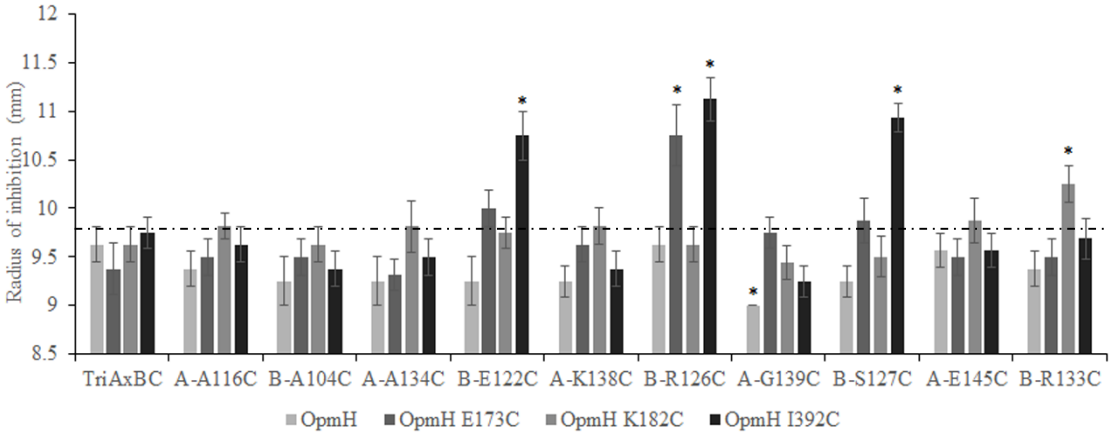

Figure 2.0.11 TriB is Essential for Opening the OpmH Channel Protein
Zones of inhibition on bacterial lawns, expressing the double cysteine mutants, spotted with1.25 µg of azithromycin were measured and reported. TriB mutants proved more capable of opening the OpmH channel. $OpmH_{I392C}$ showed significant opening of channel and increased susceptibility to drug in the presence of three different TriB cysteine mutants, indicating the role and placement of the MFP in a functional TriABC-OpmH complex.
*p-Value <0.05 (A total of 8 zones were used for analysis.)

control mutant $TriAxB_{R133C}$ that showed an increased cell resistance to the drug. Unlike

the other two cysteine positions, $OpmH_{I392C}$ was very biased to the three predicted amino acid positions of TriB ($TriB_{E122}$, $TriB_{R126}$, and $TriB_{S127}$). These $OpmH_{I392C}$ - $TriB_{Cys}$ interactions were significant, and showed increased zones of azithromycin inhibition.

In the crosslinking studies we found that $OpmH_{E173C}$, of the interprotomer groove, has a bias for TriA association, however, we find that in this experiment it was the $TriB_{R126C}$ that showed significant interactions. The correlation of $OpmH_{K182C}$, which faces the intraprotomer groove, having significant interactions with TriB held true in this experiment. We also found a strong and consistent preference of $OpmH_{I392C}$ interactions and effects in the presence of TriB cysteine mutants. It can be said that though $OpmH_{I392C}$ can interact with both MFPs, it is the interactions of TriB in the interprotomer groove of OpmH that allows for the opening of the OpmH aperture. Thus the association of TriA in this H4-H8 groove, as seen in the previous experiment, is a transient interaction. Previously, we determined the role of TriB as being essential in its interactions with transporter TriC for a functional complex [33]. Coupling that with these findings, we can further reason that the relay of conformational changes within the TriC protein allows the TriB protein to engage and open the OpmH aperture. TriA remains the anchor and stabilizer of the complex, not significantly playing a role in the opening of the channel to allow extrusion of substrates.

Altogether, we find that OpmH is an essential protein of the cell, which cannot be removed or replaced, even with a non-functional variant. Mapping the distal α-barrel

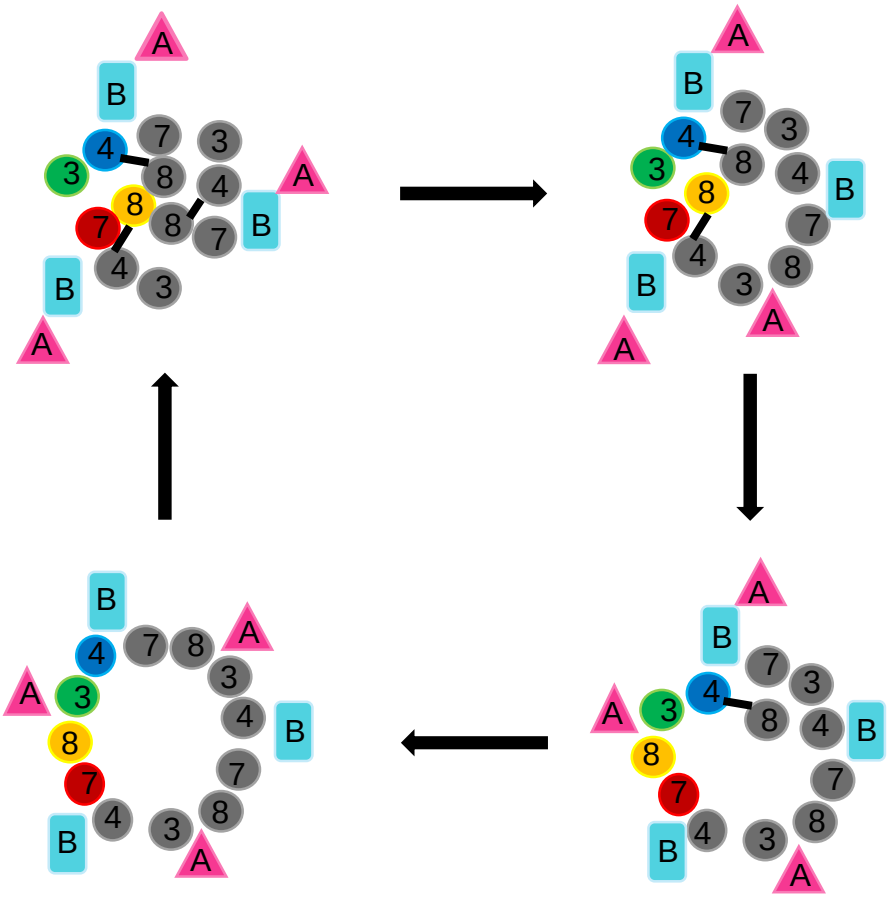

Figure 2.0.12 Proposed Mechanism of OMP Aperture Opening
TriB initially recruits and docks on the OMP OpmH. TriA undergoes conformational changes to bind OpmH and stabilize the complex. Stimulation of TriC, by TriB, caused the opening of the periplasmic aperture as substrate is expelled against proton influx.

of OpmH and the loops of TriAB with unique cysteines, we determined that TriA and TriB can both occupy the inter- and intraprotomer grooves of the channel protein. Despite the evidence from crosslinking studies pointing to potential asymmetric assembly of the TriAB proteins around OpmH, the non-equivalent roles of the proteins weaken this hypothesis and suggests a symmetric assembly of TriAB in the hexameric complex. Together with azithromycin spot assay results, these results show that TriA

stabilizes the complex with OpmH. Specifically, TriA interacts with OpmH at the interprotomer grooves, aligned to the "static" helices of the α-barrel. Thus TriB is mostly found in the intraprotomer groove. In the intraprotomer groove, TriB interacts with the dynamic helices of OpmH to render the aperture open for substrate expulsion. We propose that in the mechanism of substrate efflux by TriABC, TriB recruits and engages OpmH in complex. TriA undergoes a conformational change to associate with the OMP and stabilize the complex while TriB stimulates the transporter TriC and opens the periplasmic aperture for substrate extrusion (Figure 2.0.12).

Chapter 3. Structural Analysis of the TriABC Complex

Thus far, genetic manipulations in TriABC-OpmH have been based on the AcrAB-TolC complex. The broadly studied AcrAB-TolC has presented many structural and biochemical insights of each protein, as well as complexes of the partnering proteins. In order to verify that the structures of TriABC-OpmH follow this model, we purified individually expressed proteins, as well as protein complexes, to determine protein and complex structures for this unique RND pump system. In collaborations with the Jurgen Sygusch and Isabelle Rouiller labs, we used small angle x-ray scattering (SAXS) and negative staining EM, respectively, to analyze the structures of TriC, TriAxBC and TriAxBC-OpmH.

3.1 The Open Conformation of TriAxBC Complex

3.1.1 TriABC Form a Stable Complex

Purified proteins were prepared as described in Methods. Proteins were of about 90-95% purity, yielding varying concentrations of proteins from 1 L cultures (Figure 3.0.1). To better identify the TriA and TriB proteins within complex, we introduced unique cysteines in the α-helical domains of TriA (Glu 145) and TriB (Arg 133), both in

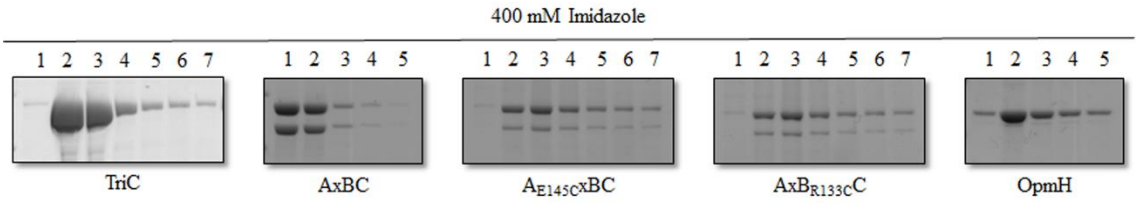

Figure 3.0.1 TriAxBC-OpmH Protein Purification
Equal volumes of purified proteins in elution buffer collected from the Cu-NTA affinity columns were analyzed by 10% SDS-PAGE gels. Fractions of proteins were eluted in 50 mM Tris-HCl (pH 8.0) buffer, 150mM NaCl, 0.03% n-Dodecyl β-D-Maltopyranoside (DDM), 1 mM phenylmethylsulfonyl fluoride (PMSF), and 400mM Imidazole. All samples were visualized by Coomassie Blue Staining.

the stabilized, covalently link TriAxB construct, and labeled with nanoprobe for structural analysis. We found that the wildtype TriAxB and its cysteine variants form stable complexes in solution with the transporter, TriC (Figure 3.0.1).

3.1.2 RND TriC is Dynamic in Solution

TriC in solution was found to be a homogeneous trimer. TriC particles (Figure 3.0.2A) were analyzed and found to resemble the *E. coli* AcrB, having the three domains characteristic for RND transporters (Figure 3.0.2B). Results also show that TriC is dynamic in solution. One conformation illustrated what would be the inner cavity between the protein trimers (Figure 3.0.2B).

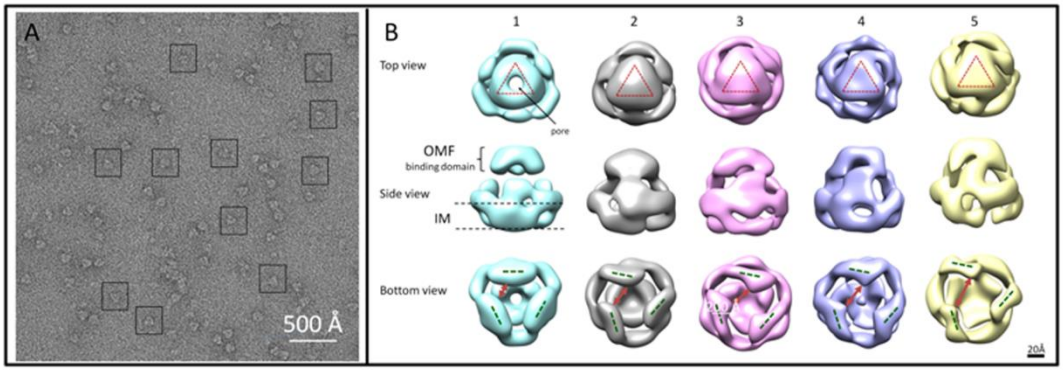

Figure 3.0.2 Homotrimeric TriC Protein Structure
A. Negative staining EM of TriC. Boxes represent TriC particles that are seen and used for analysis. **B.** Five different TriC structure constructions, showing the *i.* docking domain (red triangle), *ii.* the pore domain with cavities that allude to binding pockets, and *iii.* the transmembrane domain (green dotted line). The structure show that TriC is dynamic outside of the cell membrane. One construction (1) shows the inner cavity through the protein, but all constructions (1-5) show different measurements between the transmembrane domains (red arrow).

3.1.3 TriA and TriB Assume Different Conformations in Solution.

Images of the TriAxBC complex illustrated features unique to the complex. Unlike the MacA protein which was crystallized and shown to form a hexameric tunnel

[47], the α-helices of TriAB are not shown to assemble in this rigid structure. Three α-helical pairs of TriAB were found to be in a folded conformation, one on top of the other (Figure 3.0.3A). This structure was found to rest on the docking and pore domains of the TriC protein (Figure 3.0.3C). In order to resolve the identity and placement of the MFPs, unique cysteines were engineered – $TriA_{E145C}xBC$ and $TriAxB_{R133C}C$ – and labeled each with NANOGOLD® particles. Briefly, purified

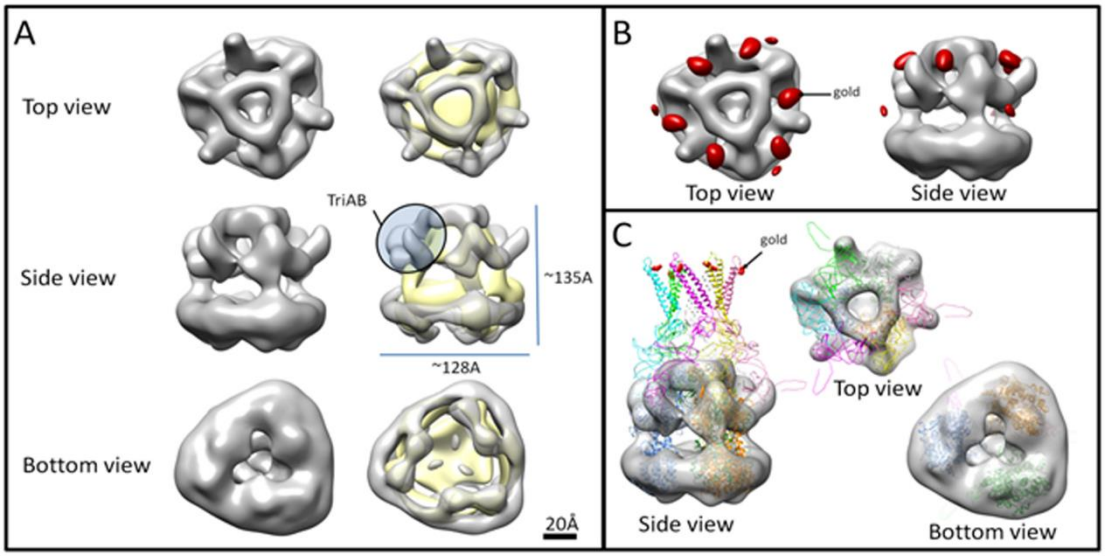

Figure 3.0.3 TriABC Structure Predictions
A. TriABC construction from samples, superimposed onto the TriC (yellow) EM map. TriAB are seen collapsed about what would be the pore and docking domains of TriC. **B.** Gold particles of labeled $TriB_{R133C}$ are localized in 9 different regions. **C.** Docking of a TriABC model (cartoon representation) unto the projected EM map.

proteins were incubated with tris(2-carboxyethyl)phosphine (TCEP) to reduce disulfide bonds. Recovered protein was mixed with freshly prepared NANOGOLD® in 2 molar excess and incubated at room temperature for 2 hours. Excess gold was removed by using Nap™-5 Sephadex™ G-25 DNA Grade columns (GE Healthcare). Labeled $TriAxB_{R133C}C$ proved successful in allowing the visualization of the α-helices that could not be identified otherwise. However, localization of gold in nine different regions of the reconstituted structure (Figure 3.0.3B) did not allow us to isolate the MFP identities

within the folded conformation. SAXS results are in agreement with the negative stain EM imaging of TriAxBC, as seen in these experiments (data not shown). Also, low yields and lack of homogeneity of purified TriAxBC-OpmH in solution resulted in a lack of any structural models for the complex.

3.2 TriAxB$_{R133C}$C Maintains Wildtype Protein Conformations

To confirm the use of the NANOGOLD®-labeled TriAxB$_{R133C}$C is representative of the wildtype TriAxBC structure, purified proteins were subject to trypsin protease digests. Briefly, equal amounts of protein were treated with 0.1, 1.0, or 10 µg/ml trypsin and incubated at 25° C for 1 hour. Samples were mixed with sample buffer, without a reducing agent, boiled and separated by SDS-PAGE. Protein bands were visualized by silver staining (Figure 3.0.4). 1 µg/ml trypsin with wildtype

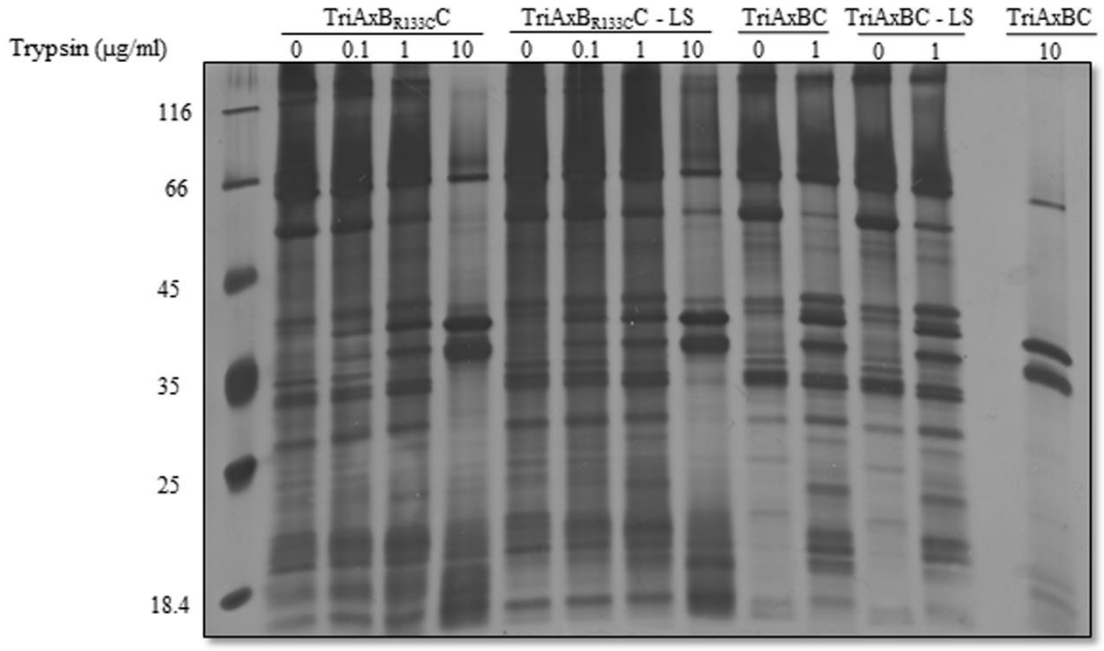

Figure 3.0.4 Gold-Labeled TriAxBC Has Same Conformation as the Wildtype Purified proteins were treated with trypsin showed no observable difference between wildtype and mutant. Crosslinked with sulfosuccinimidyl 6-(3'-(2-pyridyldithio)propionamido)hexanoate (LC-SPDP) prior to proteolysis, TriAxB$_{R133C}$C-LS, again did not suggest a different conformation than the wildtype.

TriAxBC produced several major bands indicating the truncation of the protein, likely into the individual monomers. The digestion profile of TriAxB$_{R133C}$C was identical to that of the wildtype. To test if we could induce and lock the TriAxB$_{R133C}$C mutant with disulfide bonds, to help with the structural caveats from SAXS and negative staining EM, TriAxB$_{R133C}$C purified proteins were treated with sulfosuccinimidyl 6-(3'-(2-pyridyldithio)propionamido)hexanoate (LC-SPDP) prior to trypsin digest. There was no observable difference between the wildtype and mutant proteins (Figure 3.0.4). Neither was there a change in profile compared to the non-crosslinked samples. Thus resolved structural conformations from this mutant were a good representation of wildtype TriAB.

In conclusion, we show that the TriABC proteins are stable in solution and share structural similarities to homologous proteins of their respective families. TriC assembles into a homotrimer, resembling the structure of AcrB. Though the TriAB fusion proteins fold like MexA in predictive models, this study shows that in the absence of TolC the two proteins do not maintain the funnel-like structure of the α-helical domain and assume different conformations, as was seen in our proteolysis studies (in a previous chapter). Nonetheless, we see that the TriAB dimers dock unto TriC, as has been seen in AcrAB complex models, thus results show that TriABC-OpmH assembles into a complex representative of RND efflux proteins

Chapter 4. Assessment of AcrA-TolC Interactions by Fluorescence Spectroscopy

The constitutively expressed Resistance Nodulation Division (RND) efflux pump complex of *Escherichia coli*, AcrAB-TolC, is one of the most studied tripartite systems. AcrB is an inner membrane transporter protein. A proton antiporter, AcrB provides the energy needed for the complex functionality. TolC is an outer membrane factor (OMF) providing a tunnel exit for substrate extrusion across the asymmetric bacterial cell wall into the extracellular space. Interacting with these two proteins in the periplasm is the membrane fusion protein (MFP), AcrA. In this study we sought to reconstitute the assembly of AcrAB-TolC tripartite complex *in vitro* by investigating the interactions at the AcrA-TolC interface; we used fluorescence spectroscopy as our tool of studies. Using pyrene maleimide, we expect an excited pyrene molecule, in close proximities with an unexcited pyrene, to form an excimer which emits fluorescence at a higher wavelength (~470 nm) than the excited monomeric pyrene (~375-395 nm) [70]

4.1 Development of Fluorescence Assay

We introduced unique cysteine residues in AcrA and TolC using site-directed mutagenesis (Figure 4.0.1). The trimeric TolC protein has three major domains – the β–barrel which spans the outer membrane, the α–barrel domain which extends deep into the periplasmic space, and the equatorial domain which is midway around the α–barrel. At the extracellular side, between the beta sheets of the β–barrel are two asymmetric, flexible loops; we engineered a mutant on the larger of the two loops, $TolC_{A269C}$ (Figure

4.0.1B). Granted each protomer of the α–barrel is made up of two sets of a continuous and semi-continuous coiled strand pairs, one pair is inclined 20° towards the core of the periplasmic opening. The outward-facing TolC Lys 383 was shown to interact with AcrA Asp 149 [23], thus we used this amino acid in our studies. We also used $TolC_{Q142C}$, located at the outer tip of the "straight" strand pairs, to check the specificity of TolC interactions with AcrA (Figure 4.0.1B). Lastly, aside the constriction created at the periplasmic end of the TolC barrel by the inclined helical pairs, there is a second bottleneck for substrates created by the networking of Asp 374 of the three monomers.

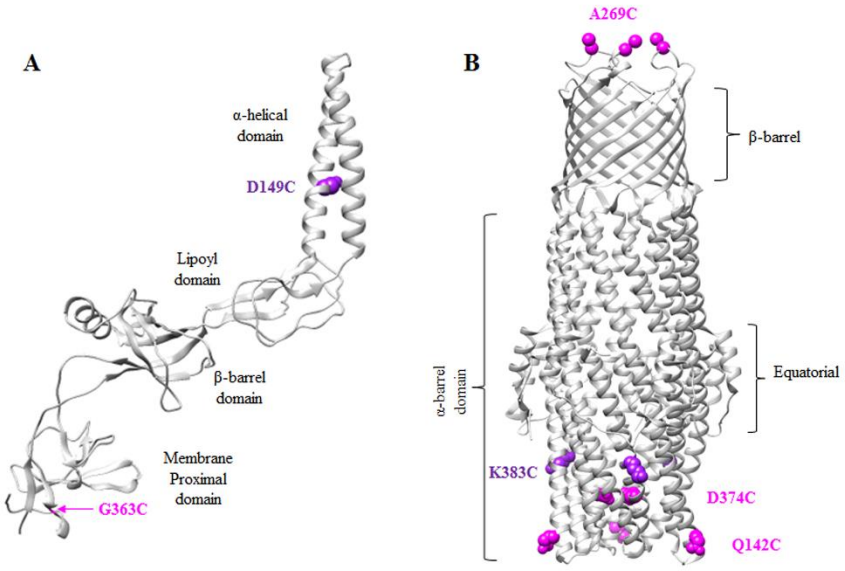

Figure 4.0.1 AcrA and TolC Protein Structures
A. Crystal structure of AcrA based on MexA (PDB code: 2V4D), model was generated using Phyre2 web portal [4]. Asp 149 (purple) is located in the α-helical domain of the protein while Gly 363 (magenta) is in the flexible membrane proximal domain. **B**. The trimeric TolC crystal structure (PDB code: 1EK9) with the (magenta) Q142C, A269C, D374C, and (purple) K383C mutations.

We introduced the same mutations of wildtype TolC and its "open", $TolC_{YFRE}$ variant. YFRE is a double-substituted TolC mutant, Tyr 363 to Phe and Arg 367 to Glu, to disrupt the salt bridge and hydrogen bond networking in the bottleneck of the periplasmic tunnel of TolC, leaving the protein opening ajar [61]. We used

TolC/YFRE$_{D374C}$ as another means of detecting the efficiency of pyrene labeling and detection of ring stacking. Unlike the TriAB-OpmH studies, we would characterize the interactions at the MFP-OMP interface as well as the integrity of these interactions within the dynamic complex.

The periplasmic membrane fusion protein, AcrA, is made up of the four domains – the α-hairpin, lipoyl, β-barrel, and membrane proximal domains (Figure 4.0.1A) [20, 22]. Although the overall structure is flexible, thanks to the short linker regions, the membrane proximal domain has proved to be the most unsteady. The highly flexible construction is shown in the crystal structure of AcrA, which excludes this fourth domain [22]. We used AcrA Asp 149 of the coiled-coil region and Gly 363 in the membrane proximal domain (Figure 4.0.1A) as site for mutagenesis. AcrA$_{D149C}$ was found to interact with TolC in a crosslinking study [23]. AcrA$_{G363C}$ has been shown to be essential for the functional activity of AcrAB-TolC [48]. It was later shown that the purified AcrA$_{G363C}$ was better able to retain interactions with AcrB and TolC than wildtype AcrA in the surface plasmon resonance (SPR) assays [44].

Table 4.0.1 Antimicrobial Susceptibility of *E. coli* ZK769 Cells Expressing TolC and YFRE.

	MIC (μg/mL)				
Substrate	**pTrc**	**TolC**	**TolC$_{K383C}$**	**YFRE**	**YFRE$_{K383C}$**
Puromycin	2	64	64	32	32
Chloramphenicol	0.8	3.2	3.2	3.2	3.2
Erythromycin	1	64	64	16	16
Novobiocin	1	32	32	16	16
SDS	9.76	>10,000	>10,000	>10,000	>10,000

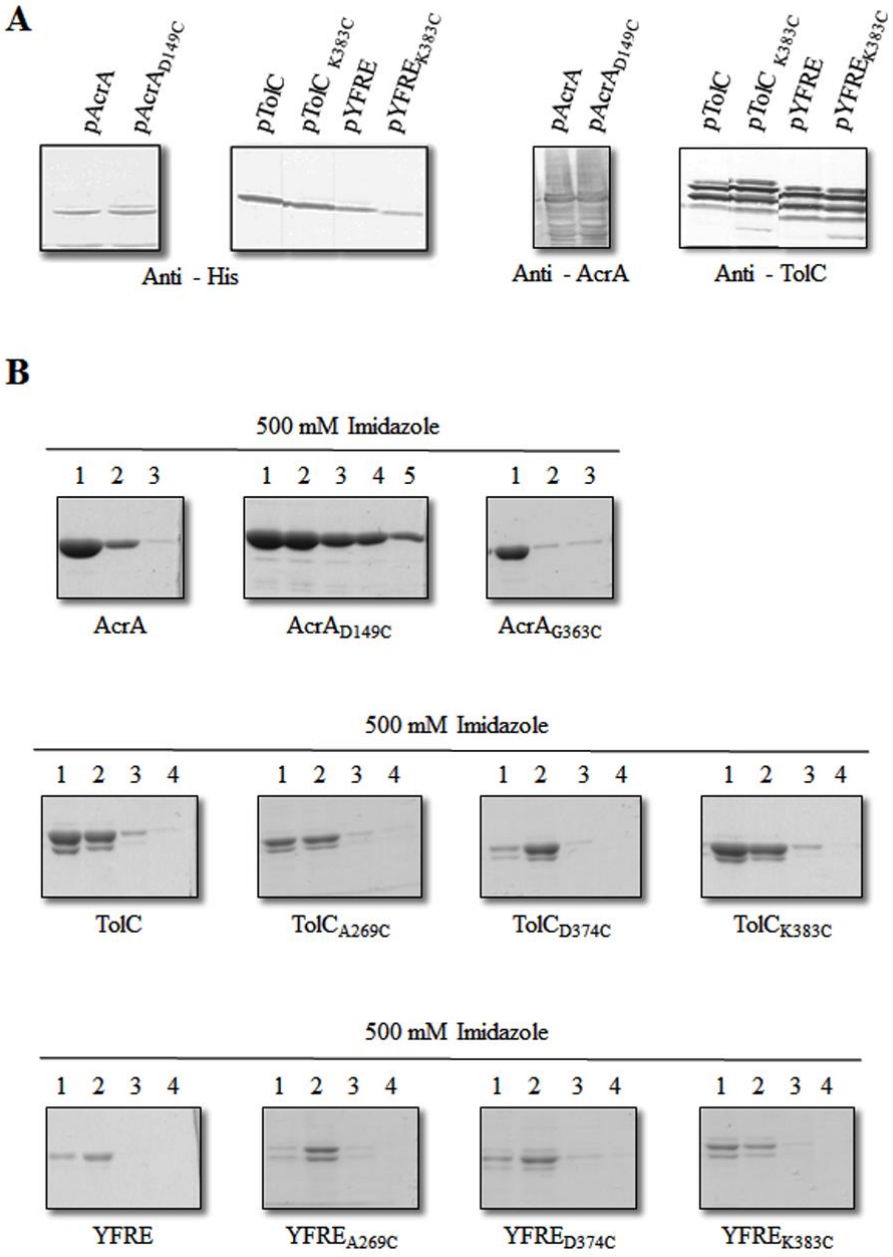

Figure 4.0.2 AcrA and TolC Cysteine Mutant Expression and Protein Purification
A. Whole cells (5e+07 cells) expressing AcrA and TolC cysteine mutants were analyzed by SDS-PAGE electrophoresis followed by transfer onto a PVDF membrane and incubation with anti-His, anti-AcrA, or anti-TolC antibodies. All mutants are expressed to the similar levels as was the wildtype. **B.** Equal volumes of purified proteins in elution buffer collected from the Cu-NTA affinity columns were analyzed by 10% SDS-PAGE gels. Fractions of AcrA were eluted in 20 mM Tris-HCl (pH 8.0) buffer, 500mM NaCl, 0.03% n-Dodecyl β-D-Maltopyranoside (DDM), 1 mM phenylmethylsulfonyl fluoride (PMSF), and 500mM Imidazole. The TolC proteins were eluted in 20 mM Tris-HCl (pH 7.5) buffer, 100mM NaCl, 0.03% (DDM), 1 mM (PMSF), and 500mM Imidazole. All samples were visualized by Coomassie Blue Staining.

4.1.1 Expression, Functionality, and Purification

Isolated cell membranes visualized by immunoblotting showed that expression of the mutants AcrA and TolC were similar to that of the wildtype proteins (Figure 4.0.2A). The effects of the cysteine mutations in TolC on its function was tested by measuring the MICs. We found that the Lys 383 to Cys mutation in TolC does not affect the susceptibility of cells to antibiotic substrates (Table 4.0.1).

For the *in vitro* studies, wildtype proteins and cysteine variants were overexpressed by induction with isopropyl β-D-1-thiogalactopyranoside (IPTG), under the lac operon. The 6-histidine tagged proteins were bound and eluted off Cu-NTA affinity chromatography columns. AcrA was eluted in 20 mM Tris-HCl (pH 8.0) buffer, 500mM NaCl, 0.03% n-Dodecyl β-D-Maltopyranoside (DDM), 1 mM phenylmethylsulfonyl fluoride (PMSF), and 500mM Imidazole. TolC proteins were eluted in the same buffer (pH 7.5), except 100 mM NaCl was used. Elution fractions were separated by SDS-PAGE and visualized by Coomassie Brilliant Blue staining (Figure 4.0.2B). All proteins were at least 90% pure.

4.1.2 Fluorescence Assays with Free Pyrene Maleimide

The honeycomb-shaped pyrene modified with a maleimide group addition (Figure 4.0.3A) allows for more selectivity in reactions with thiol groups and eliminates cross-reaction with histidine and methionine [78]. Previously, it has been reported that in organic solvents, as the concentration of pyrene is increased, the expected decrease in monomer fluorescence was replaced by a unique quenching. This quenching occurs when an excited pyrene molecule, in close proximities with an unexcited pyrene, forms

an excimer which emits fluorescence at 470 nm [70]. To determine fluorescence intensity emitted by pyrene, when excited with light at 337 nm, we varied the amount of sample exposure to light by using different bandwidth openings (data not shown). We also investigated the effects of buffer pH on fluorescence activity. We found that at 5 nm bandwidth, there was an increase in fluorescence intensity as buffer pH was increased

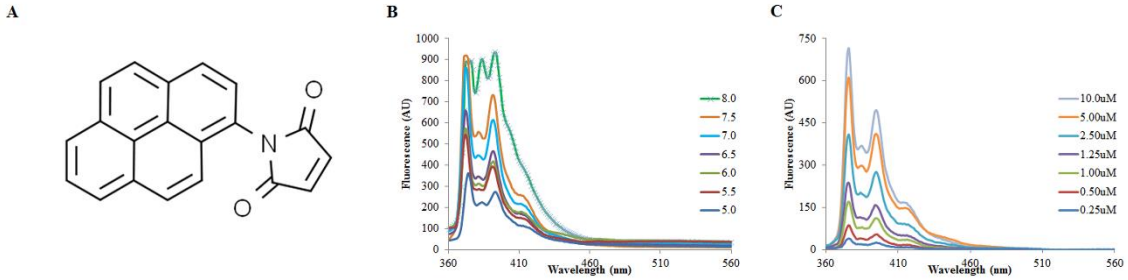

Figure 4.0.3 Fluorescence Spectrum of Pyrene Maleimide
A. The honeycomb-shaped pyrene molecule modified with a maleimide group. **B.** Emission spectrum of 20 μg/mL (67.3 μM) pyrene maleimide (PM) at varying pH buffer conditions. PM was excited at 337 nm and the intensities were measured through a 5 nm bandwidth. **C.** Concentration-dependence fluorescence of free PM in 20 mM Tris-HCl (pH 7.5), 150 mM NaCl, 0.03% DDM. Experiments were done at room temperature with 5 nm bandwidths.

from 5.0 to 7.5 (Figure 4.0.3B). Using the same specifications, we then investigated the concentration-dependent of pyrene fluorescence intensities in buffer pH 7.5. Fluorescence intensities increase as the concentration of pyrene increased (Figure 4.0.3C).

4.1.3 Pyrene Maleimide Labeling and Fluorescence Assays

In order to label the purified $AcrA_{D149C}$ and $TolC_{K383C}$ proteins with pyrene, the thiol groups were reduced in the presence of tris(2-carboxyethyl)phosphine (TCEP) resin, then incubated with fresh pyrene maleimide (Figure 4.0.3A) in 20 molar excess. Excess pyrene was removed and proteins were dialyzed into the buffer containing 20 mM MES (pH 6.0), 0.03% DDM and 150 mM NaCl for experiments.

To find optimal experimental conditions, the emission spectra between 360-560 nm of the individually labeled proteins were collected at different protein concentrations. We also mixed AcrA and TolC in varying ratios and measured fluorescence intensities. However, no red-shift peaks, as would be expected for $AcrA_{D149C}$ and $TolC_{K383C}$ interaction, were detected (data not shown).

We calculated the ratios of PM present in the protein samples by defining the

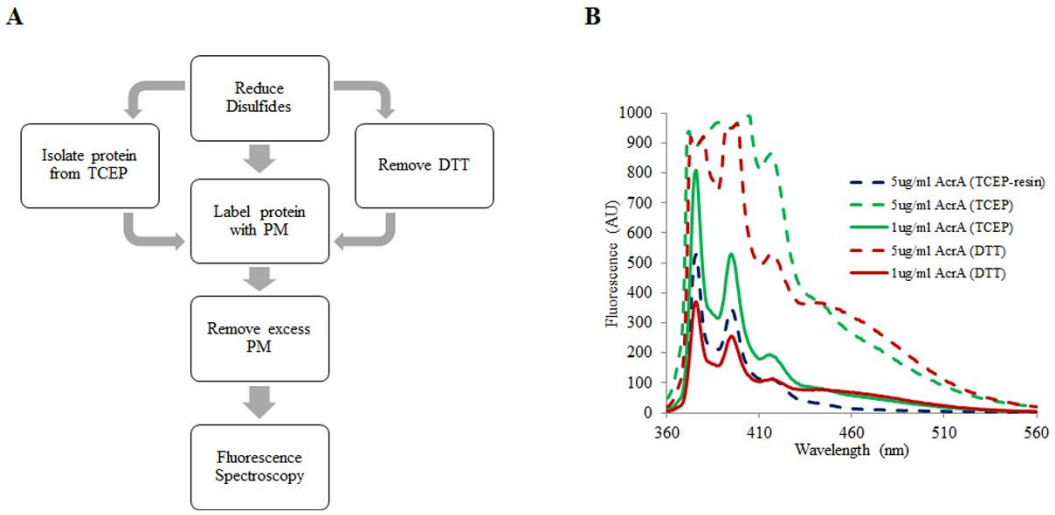

Figure 4.0.4 Alternate Labeling of $AcrA_{D149C}$ with Pyrene Maleimide
A. Three aliquots of purified $AcrA_{D149C}$ were subject to different reducing conditions prior to labeling with PM. Two sample sets were subject to TCEP resin or 50 mM TCEP. The third sample aliquot was reduced by 50 mM DTT and subject to gel filtration prior to PM labeling. All three protein sets were then labeled with 10 molar excess PM, dialyzed to remove excess PM from the reaction, then used in experiments. **B.** Emission spectrum of $AcrA_{D149C}$-PM excited at 337 nm, bandwidth of 5 nm, and in 20 mM MES (pH 6.0), 150 mM NaCl, and 0.03% DDM.

area of fluorescence intensities then determining the amount of fluorescence intensities between 375-395 nm, and we compare the values to a calibration curve of free PM fluorescence intensities (data not shown). Results show that there was excess PM in the protein samples. Therefore, we tested alternate ways of labeling the proteins (Figure 4.0.4A). In addition to reducing protein samples in TCEP resin, we prepared two additional samples: one batch was reduced by 50 mM dithiolthreitol (DTT), the excess

of which was removed by Nap™-5 Sephadex™ G-25 DNA Grade columns (GE Healthcare). The other batch was reduced by addition of 50 mM TCEP solution to reduce disulfide bonds. All three sets of sample preparation were labeled with 10 molar excess PM instead of 20 molar excess. The excess pyrene was removed by Nap™-5 Sephadex™ G-25 DNA Grade columns, all samples were dialyzed and used for experiments. Fluorescence emission spectrum (Figure 4.0.4B) and calculations of PM-AcrA ratios, showed that at pH 6.0 $AcrA_{D149C}$ incubation within TCEP resin was the best reducing and labeling procedure, granted there was still excess PM in relation to amount to AcrA (data not shown).

Despite the fact that AcrA-TolC binding interactions has been proven at pH ~6.0 [44], we did not see any indication of protein-protein interactions by expected red-shift fluorescence peak at ~470 nm. We tested proteins labeled by different protocols, as well as the fluorescence emission pattern of AcrA-TolC at higher pH (pH 7.5) and with a smaller bandwidth (3 nm) for light entrance and exit. At this pH, the AcrA and TolC proteins retain their positive and negative charges, respectively. Prior to experiments, we investigated the appropriate means of labeling each protein and found that $AcrA_{D149C}$ was most efficiently labeled with PM under non-reducing conditions, $TolC_{K383C}$ was best labeled after reduction of thiols in TCEP resin, and $YFRE_{K383C}$ was best labeled when thiols were reduced in 50 mM TCEP (Figure 4.0.5).

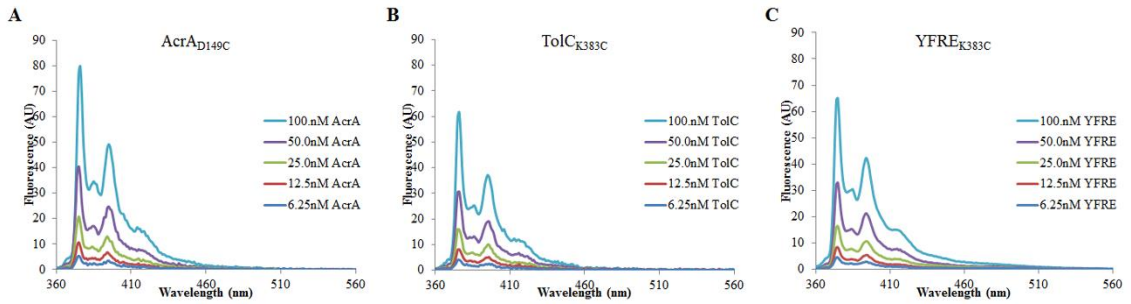

Figure 4.0.5 Concentration-Dependent Fluorescence Spectrum of PM Labeled AcrA$_{D149C}$, TolC$_{K383C}$, and YFRE$_{K383C}$.
Samples were in 20 mM Tris-HCl (pH 7.5), 150 mM NaCl, and 0.03% DDM, excited at 337 nm, with bandwidths of 3 nm. Protein samples were treated in various ways prior to PM labeling, the best methods are shown. **A.** AcrA$_{D149C}$ thiols were not reduced prior to PM labeling, **B.** TolC$_{K383C}$ was reduced in TCEP resin, and **C.** YFRE$_{K383C}$ was best labeled after reduction by 50 mM TCEP, with no dialysis before labeling.

4.1.4 Time Course Analysis of AcrA-TolC Interactions

Hypothesizing that reaction time in the established fluorescence assay was not enough to observe what could be a transient reaction, we sought to investigate the effect of time. We set up our experiments the same as before: we analyzed individually labeled proteins, as well as mixed labeled AcrA$_{D149C}$ and TolC$_{K383C}$. Emission intensities were measured at 465 nm every 20 seconds for 10 minutes. Results showed no observable difference of all reactions (data not shown).

4.2 Optimizing Fluorescence Assay for AcrA-TolC Interaction Studies

4.2.1 Stabilizing Protein-Protein Interactions by pH and Mg^{2+}

SPR studies of AcrA-TolC [25] showed that the protein-protein interactions were best investigated at pH 6.0. We initially performed experiments of AcrA$_{D149C}$ and TolC$_{K383C}$ under these conditions but there were no observed protein-protein interactions by an excimer peak formation on the fluorescence spectrum (Figure 4.0.6A, C). To

promote more stable protein-protein interactions, producing more stable pyrene stacking, AcrA-TolC samples were supplemented with Mg^{2+}.

It has been shown that the presence of Mg^{2+} does not change conformations of proteins, but it is able to affect protein stability [79]. Titrating AcrA and TolC, in buffer conditions of pH 6.0, we also added 1 mM Mg^{2+} to produce more stable protein interactions. Fluorescence emission spectrum of both experiments proved futile (Figure

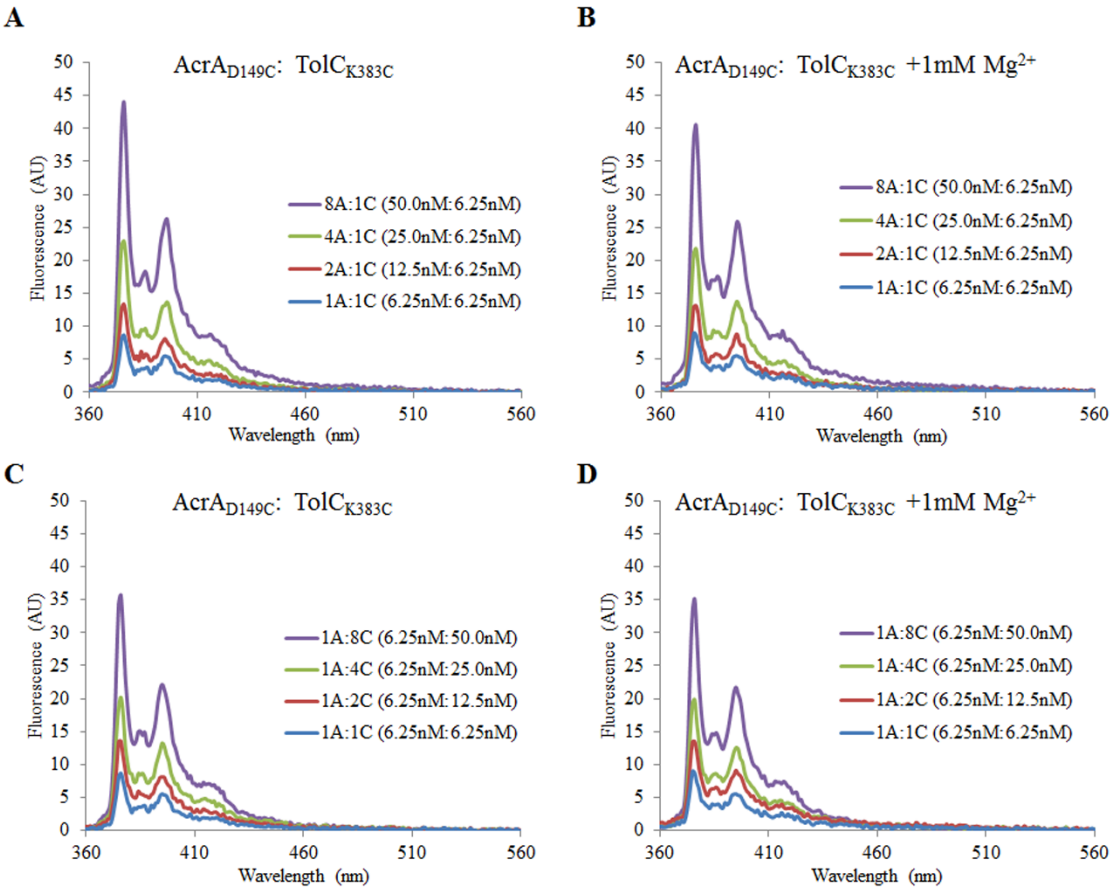

Figure 4.0.6 AcrA$_{D149C}$-TolC$_{K383C}$ Do Not Interact at pH 6.0
In combination studies of AcrA$_{D149C}$ and TolC$_{K383C}$, labeled purified proteins were mixed at ratios indicated and used for experiments. All samples were in 20mM MES (pH 6.0), 150 mM NaCl, and 0.03% DDM. Pyrene was excited at 337 nm, and bandwidths were set at 3 nm. Titrating AcrA$_{D149C}$ to TolC$_{K383C}$ (**A**), we did not see any peaks for excimer formation so 1 mM $MgCl_2$ (**B**) was used to stabilize potential interactions. We also titrated TolC$_{K383C}$ to AcrA$_{D149C}$ in the absence (**C**) and presence (**D**) of Mg^{2+}. We again did not observe red shift peaks at 470 nm to indicate protein-protein interactions.

4.0.6B, D), there was not any indication of pyrene-pyrene stacking under these conditions.

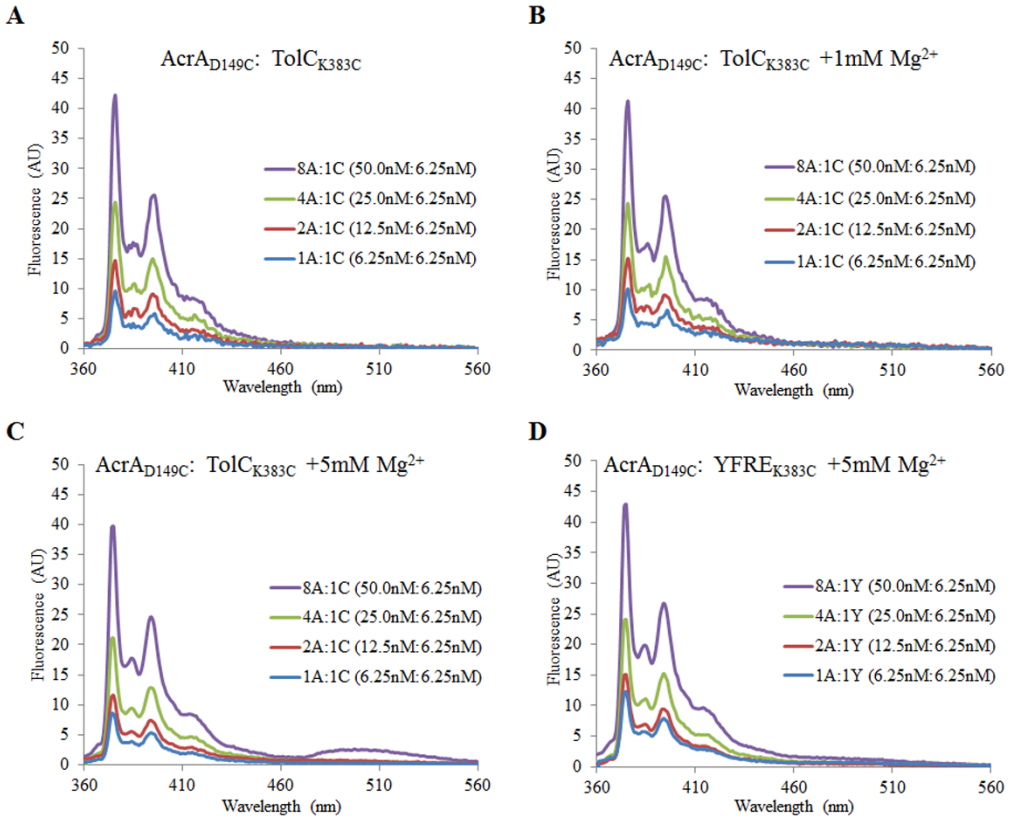

Figure 4.0.7 Mg^{2+} Stabilizes AcrA$_{D149C}$-TolC$_{K383C}$ Interactions at pH 7.5
A. Titrating pyrene labeled AcrA$_{D149C}$ to TolC$_{K383C}$ in 20 mM Tris-HCl (pH 7.5), 150 mM NaCl, and 0.03% DDM, the fluorescence spectra of pyrene emission did not show interactions between the proteins. **B.** Stabilizing interactions with 1 mM $MgCl_2$ had no effect. **C.** Increasing Mg^{2+} concentration to 5 mM produced a second peak in the fluorescence spectrum. **D.** The same result was not observed for AcrA$_{D149C}$ with YFRE$_{K383C}$.

Exploring the effects of buffer condition on ionic strengths and protein interactions, we increased buffer pH conditions to 7.5 where AcrA was less positively charged and TolC proteins were more negatively charged (Figure 4.0.7A). Repeating the AcrA$_{D149C}$-TolC$_{K383C}$ protein pair interaction studies, we titrated AcrA amounts to TolC and induced interactions by supplementing the reaction buffer with 1 mM Mg^{2+} (Figure 4.0.7B) and did not obverse changes in the emission spectrum. Increasing

induction to 5 mM Mg^{2+} proved effective; we saw a new peak in our results at ~490 nm (Figure 4.0.7C). Investigating the consistency of the $AcrA_{D149C}$-$TolC_{K383C}$ interactions, as would be found in the cell, we used the open, $YFRE_{K383C}$, TolC. Using the same experimental conditions, we found that interactions of $AcrA_{D149C}$-$YFRE_{K383C}$ were not stabilized in the presence of 5 mM Mg^{2+} (Figure 4.0.7D). Results were not reproducible.

4.2.2 Reselection of Amino Acids

The experiments described above inferred that the chosen sites were not close enough for the monitoring of interactions by fluorescence spectroscopy using pyrene maleimide. In order to further prove the effectiveness of PM for labeling and as a probe for studying protein-protein interactions, we selected different amino acid residues in AcrA and TolC. For AcrA, we used $AcrA_{G363C}$, an amino acid residue in the membrane proximal domain (Figure 4.0.1A). For TolC/YFRE we mutated Ala 269 of the extracellular loops, and Gln 142 and Asp 374 of the α-barrel domain (Figure 4.0.1B). When labeled with pyrene at these positions, the proteins were to induce pyrene-pyrene stacking more readily. We did not see excimer formation in any of these experiments (data not shown).

4.2.3 Inducing Disulfide Bonding

The trimeric TolC periplasmic aperture is interlocked by hydrogen bonds and salt bridges involving the interactions the amino acid residues Thr 152, Asp 153, Tyr 362, and Arg 367 [37]. This ~4 Å opening is the first of two bottlenecks of the TolC

structure. The second, tighter bottleneck is found higher up in the α-barrel domain, and consists of three Asp 374 – one from each monomer of TolC [62]. Considering that such a constriction might not allow for effective labeling of pyrene maleimide at Asp 374, we checked all mutants for spontaneous disulfide formations.

Purified AcrA and TolC cysteine variants were labeled with PM per earlier established protocols. 150 ng of boiled protein was separated by 10% SDS-PAGE gel electrophoresis, in the absence of reducing agents, and visualized by silver staining (Figure 4.0.8). We found that except for $TolC_{K383C}$ and $YFRE_{K383C}$, all other mutants formed oligomers in the presence and absence of pyrene. This result was inconsistent

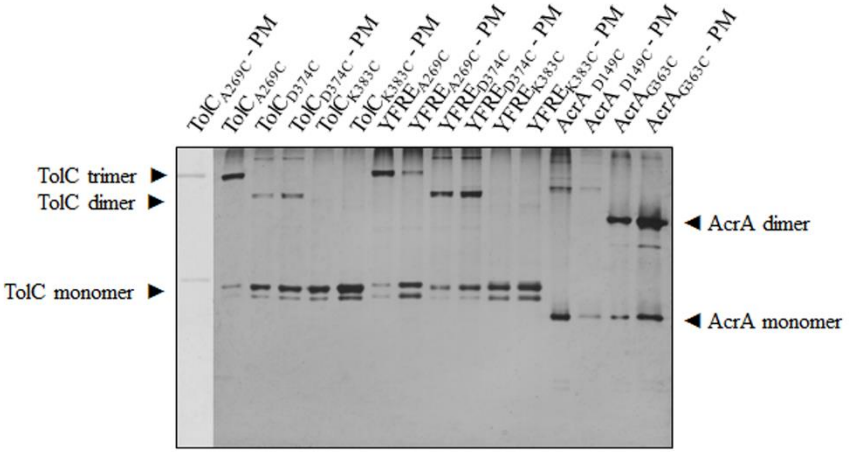

Figure 4.0.8 $TolC/YFRE_{K383C}$ Does Not Form Spontaneous Disulfides
150 ng of boiled pyrene labeled or free protein samples were separated by 10% SDS-PAGE gel electrophoresis in the absence of reducing agents. The gel was visualized by silver staining.

with the fluorescence spectra which did not show the red shift characteristic in the case of $AcrA_{D149C}$, $AcrA_{G363C}$, $TolC/YFRE_{A269C}$, and $TolC/YFRE_{D374C}$.

Since we see dimerization on the gels but not by fluorescence, we tested whether $AcrA_{D149C}$ and $TolC/YFRE_{K383C}$ could form disulfide bonds by gel electrophoresis. To help promote disulfide bonding between the two cysteine modified proteins, we incubated proteins with 50 μM $CuCl_2$ after reducing thiols in the presence of TCEP. In the absence of reducing agents, we found that we were able to induce disulfide bond in $TolC_{K383C}$ and $YFRE_{K383C}$ samples containing Cu^{2+} (Figure 4.0.9A, B). Titrating AcrA and TolC/YFRE in the presence of Cu^{2+}, we were able to identify high molecular weight oligomers. Treating these samples with DTT, we found that the observed oligomers were not AcrA-TolC interactions – the protein profiles were the same as seen before (Figure 4.0.9C, D).

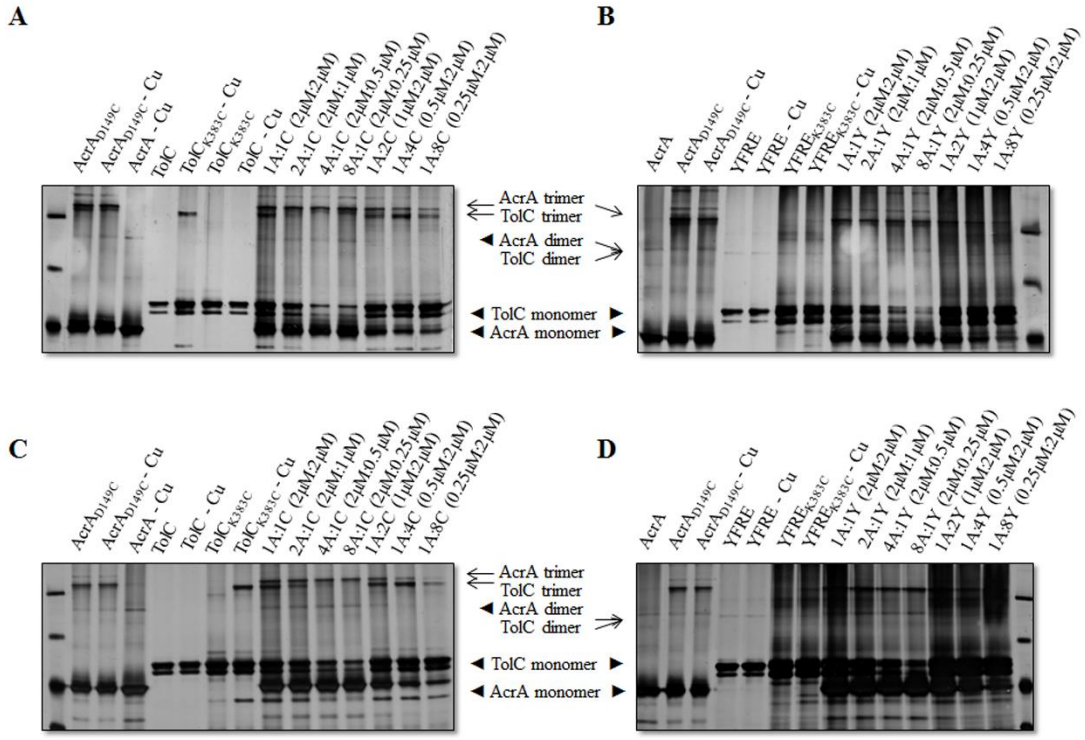

Figure 4.0.9 $AcrA_{D149C}$-$TolC/YFRE_{K383C}$ Interactions Cannot Be Stabilized by Cu^{2+}
Purified protein samples were treated with 5 μM TCEP for 1 hour. Mixed protein combinations (**A** - $AcrA_{D149C}$-$TolC_{K383C}$, **B** - $AcrA_{D149C}$-$YFRE_{K383C}$) were oxidized with 50 μM $CuCl_2$ for 30 minutes to promote disulfide bonding. Samples were boiled and separated by 10% SDS-PAGE gel electrophoresis and visualized using silver staining. Samples were treated with DTT (**C, D**) to reduce high molecular weight samples. We did not note a difference in protein profiles in the presence of DTT.

Taken together, we find that despite the previous results showing interactions of $AcrA_{D149C}$ and $TolC_{K383C}$ [23], we could not reproduce said interactions nor could we determine the integrity of said interactions with the closed and open TolC conformations. Considering experiments with alternate sites of protein labeling did not produce results as expected, we can deduce that conditions are not sensitive enough to map the protein-protein interfaces of the AcrA-TolC bipartite complex. However, experiments with TriAB-OpmH (see previous chapters) indicate that docking of AcrA-TolC, as being studied (wrapping), is different from the preferred mode of assembly (bridging) of MFPs and OMFs. Nonetheless, pyrene maleimide labeling and analysis of excimer formations was not sufficient to characterize interactions within protein protomers.

Chapter 5. Surface Plasmon Resonance Studies of EPI Interactions with Transporter Protein AcrB

There have been strategies proposed and used for the disabling of functional efflux pumps within the bacterial cell [18]. In this study, we explore one such strategy, the use of efflux pump inhibitors (EPIs). These inhibitors are designed to be used in addition to therapeutics to reduce the minimal inhibitory concentrations (MICs) of antibiotics, however, it has also been shown to reduce the invasiveness of human pathogens, such as *Pseudomonas aeruginosa* [80].

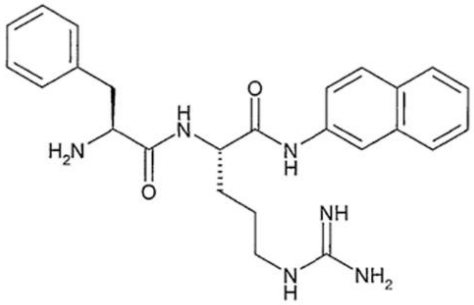

Figure 5.0.1 Phenylalanine Arginyl β-Napthylamide (PAβN).

In collaboration with Basilea Pharmaceutica, we sought to identify EPIs that would interact with the transporter AcrB. For this purpose, we used SPR to analyze the binding kinetics of EPIs to immobilized AcrA, AcrB, and TolC. Phenylalanine arginyl β-napthylamide (PAβN) is the first compound identified as an EPI effective against the *Pseudomonas* MexAB pump (Figure 5.0.1). It has been shown to restore activities of antibiotics of different classes [81, 82]. However, although PAβN has also been shown to compete with certain antibiotics – imipenem and gentamicin– it does not compete with the likes of levofloxacin and carbenicillin [82-84]. PAβN inhibits efflux by causing an accumulation of pump substrates within the cell, as well as altering the permeability of the *P. aeruginosa* outer membrane. We used PAβN as the control for our studies.

Basilea Pharmaceuitica discovered inhibitors (Table 5.0.1) were the analytes of interest for our experiments.

Table 5.0.1 Basilea Pharmaceutica Efflux Inhibitors and Properties.

Compound	Noted Letter	MW (g/mol)	Sample MW (g/mol)	pKa			
				1	2	3	4
BAL 0113299-000-001	A3299	480.65	480.65	-5.00	4.94	9.21	-5.59
BAL 0113347-001-001	B3347	316.82	389.75	-5.16	7.89	10.60	
BAL 0113468-001-001	C3468	424.51	652.55	6.57	10.19	-5.36	-1.83
BAL 0113470-000-001	D3470	308.29	308.29	2.85	-7.17	15.36	-8.32
BAL 0113501-001-001	E3501	483.53	597.55	5.13	-6.40	-5.34	-1.83
BAL 005718-002-002	F5718						
BAL 0108043-001-001	J8043	312.45	385.37	-5.18	9.89	7.11	
BAL 0113594-001-001	K13594	395.72	468.64	-5.16	7.89	10.60	
BAL 0113711-001-001	L13711	249.74	363.76	15.86	8.12	10.66	
BAL 0113731-000-001	M13731	336.14	336.14	-8.13	1.24		
BAL 0113758-001-001	N13758	282.34	355.26	-9.29	7.77	10.58	

To characterize the interactions of the compounds with the AcrB, we used Surface Plasmon Resonance (SPR). SPR is a real-time binding assay that uses changes

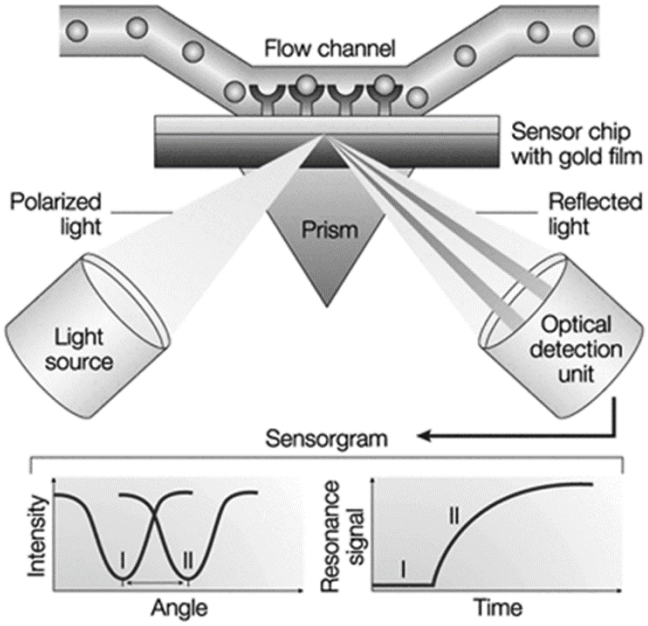

Figure 5.0.2 Surface Plasmon Resonance (SPR)
SPR is a real-time binding assay that uses changes in the refractive index of light at the interface of a gold thin film on glass and solution of interest to measure the association and dissociation of biomolecules [6]

in the refractive index of light at the interface of a gold thin film on glass and solution of interest to measure the association and dissociation of biomolecules [85] (Figure 5.0.2). SPR allows for the study of interactions of proteins, nucleic acids, cells, etc with binding partners as well as small molecules, even those in organic solvents; these interactions can be studied without labeling of binding partners. Another advantage of SPR, is the low volumes needed to run experiments and yet, due to the high sensitivity of the method, detection of interactions allows for kinetic and thermodynamic analysis, concentration assays, binding stoichiometries, etc. In this study, experiments were conducted on 1. the SensíQ® Pioneer, with data analyzed using Qdat©, and 2. the Biacore 3000 unit, with data analyzed using the BIAEvaluation 2.1©. Previously, a

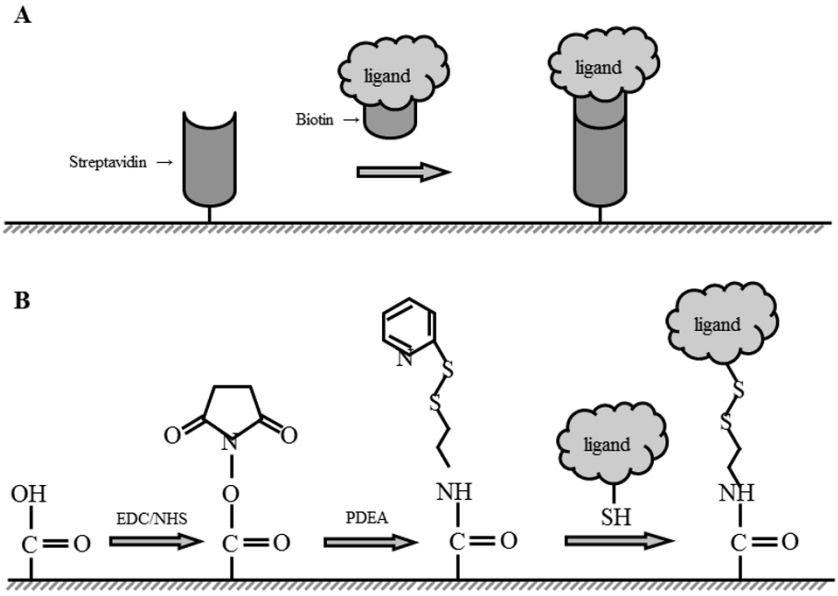

Figure 5.0.3 SPR Chip Surface Chemistry for Protein Immobilization
A. Biotinylated ligand is injected over the streptavidin surface of the chip to form an irreversible. **B**. In the chemistry of thiol coupling, the reduced thiol of the ligand substitutes the aromatic ring of the 2-(2-pryidinyldithio)ethaneamine (PDEA) in the final step.

similar approach had been used to characterize interaction of substrates and inhibitor with AcrB and to study protein-protein interaction of TolC and different MFPs [25, 44].

To immobilize our proteins of interest (AcrB, AcrA, and TolC) to the streptavidin surface of the sensor chip, proteins were biotinylated before injection (Figure 5.0.3A). However, due to the irreversible nature of this bond, we later immobilized the proteins using thiol coupling (Figure 5.0.3B) to allow control of the amount of protein on the chip surface. Preliminary experiments were conducted on the SensíQ® Pioneer, then later simultaneously with experiments on the Biacore 3000.

5.1 Immobilization of AcrB and AcrB$_{D408A}$ and Binding Assay Development on the SensíQ® Pioneer

Previously, the AcrB protein had been genetically modified to replace the two intrinsic cysteine residues, at positions 493 and 887, to serines to create a cysteineless protein [44]. This cysteineless AcrB was further modified by site-directed mutagenesis to

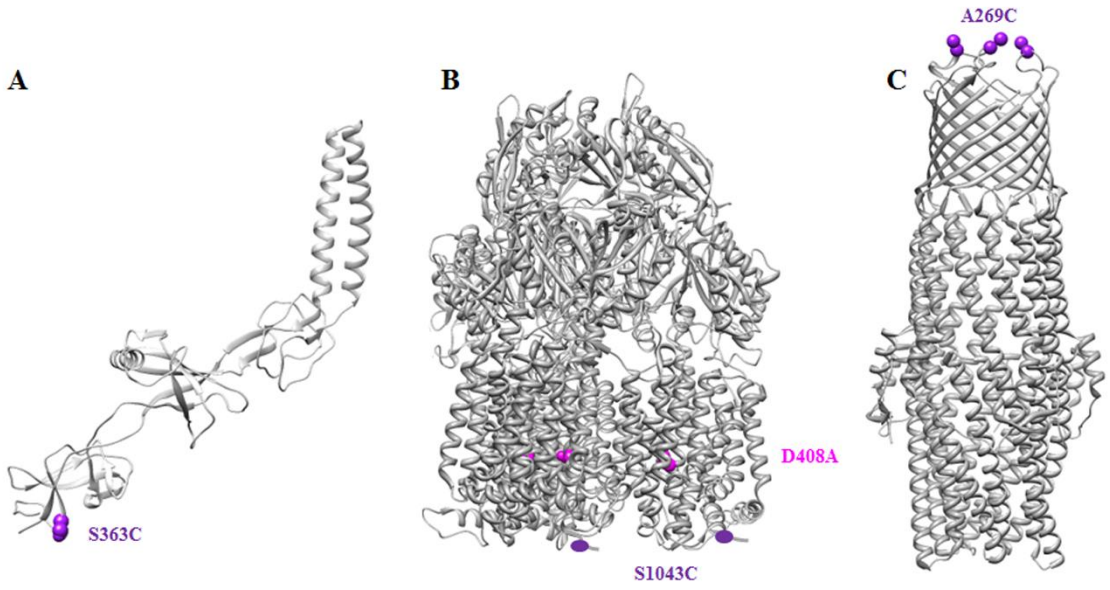

Figure 5.0.4 AcrA, AcrB, and TolC Cysteine Variants for SPR Immobilization **A**. Crystal structure of AcrA$_{S363C}$ based on MexA (PDB code: 2V4D), model was generated using Phyre2 web portal [4]. **B**. AcrB$_{S1043C}$ (purple) and the D408A mutant (magenta) (PDB code: 2HRT). **C.** TolC crystal structure (PDB code: 1EK9) with the A269C mutation.

introduce a cysteine at Ser 1043 (Figure 5.0.4B) to serve as the amino acid residue for the immobilization of the protein. Additionally, four histidine residues were introduced to the C-terminus of AcrB to create a 6-Histidine tag that was used for the purification of the proteins by Cu-NTA affinity chromatography [32].

In the functional mechanism of AcrB, it has been shown that Asp 407, Asp 408, and Lys 940 are at the core of the proton translocation site, and the interactions and relay of a proton is responsible for the functional rotation of the transporter protein. The two negatively charged aspartic acid residues are responsible for the binding and release of the protons and thus are crucial for the binding and extrusion of drug substrates [3, 39, 40, 86]. We substituted the charged aspartic acid amino acid with a neutral alanine residue by site-directed mutagenesis (Figure 5.0.4B). The expression of $AcrB_{D408A}$ was the

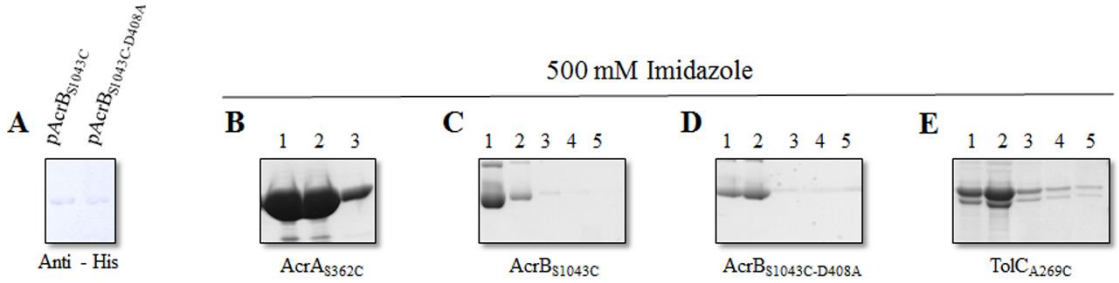

Figure 5.0.5 Expression and Purification of AcrA, AcrB and TolC Mutants
A. 2µg of unboiled AcrB and $AcrB_{D408A}$ were separated by 10% SDS-PAGE and transferred onto a PVDF membrane and incubated with anti-His antibodies. $AcrB_{D408A}$ expresses to the same level was the wildtype. **B – E.** Solubilized membranes in buffer containing 2% DDM was passed through Cu-NTA affinity column to bind Histidine-tagged proteins. Non-specific interactions were disrupted by wash steps, then $AcrA_{S362C}$, $AcrB_{S1043C}$, $AcrB_{S1043C-D408A}$, and $TolC_{A269C}$ proteins were eluted off separate columns in Tris-HCl buffer solutions, supplemented with NaCl, PMSF, DDM, and Imidazole. Elution fractions were separated by 10% SDS-PAGE and visualized by Coomassie Brilliant Blue staining.

same as the wildtype protein (Figure 5.0.5A), but the mutation makes the protein non-functional and thus was used to investigate the effects of function disruption on substrate binding specificity and efficiency with AcrB.

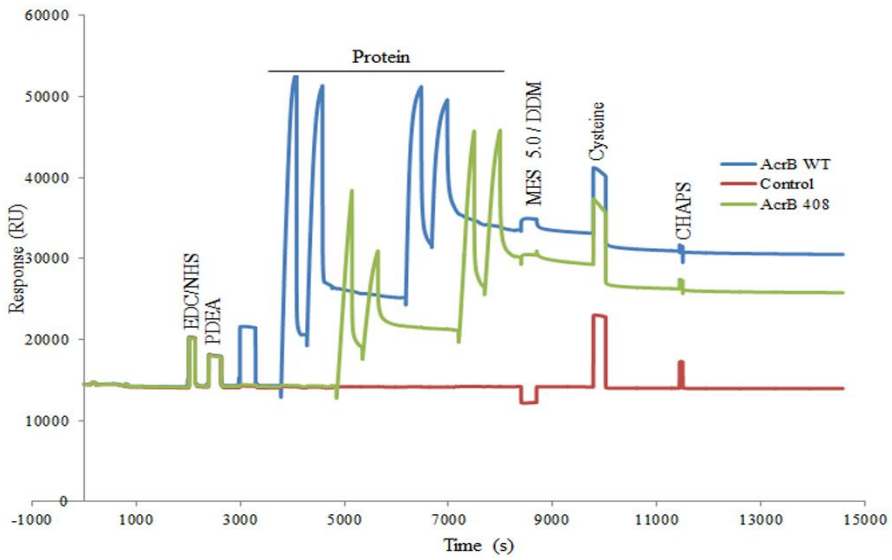

Figure 5.0.6 Immobilization Sensogram of AcrB and mutant using Thiol Coupling All surfaces of gold chip undergo the same surface chemistry with the exception of protein of interest (or the control surface). AcrB and $AcrB_{D408A}$ bound with surface densities of ~16000 RU and ~11000 RU, respectively.

To develop a binding assay, purified $AcrB_{S1043C}$ and non-functional $AcrB_{S1043C-D408A}$ proteins (Figure 5.0.5C, D) were reduced in the presence of tris(2-carboxyethyl)phosphine (TCEP) and immobilized onto the chemically-modified chip surface at approximately the same surface densities of 15898 Response Unit [87] and 11197 RU, respectively (Figure 5.0.6). Wildtype AcrA was injected over the AcrB surfaces to validate that immobilization of protein by thiol coupling was successful, and to ensure that the proteins were still functional and interacting as formerly established [44]. We found that AcrA binds to the AcrB protein and its $AcrB_{D408A}$ variant with the

same affinity (Figure 5.0.7). Thus, both variants of the protein are competent in interaction with AcrA.

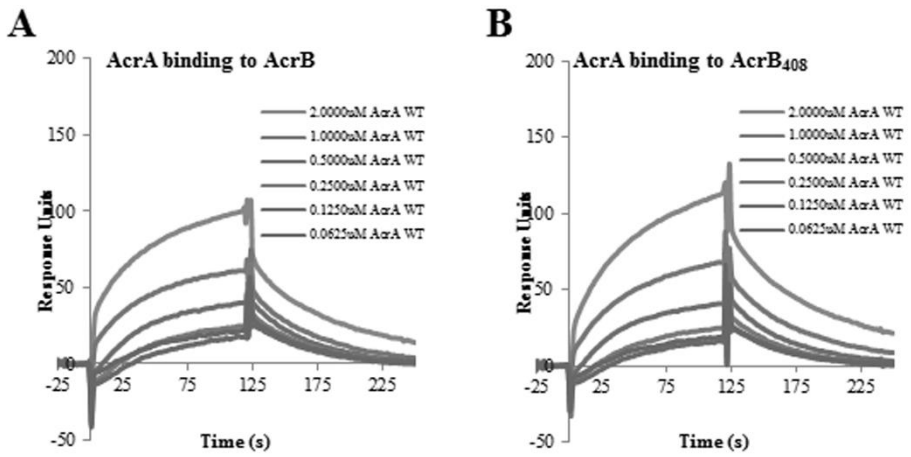

Figure 5.0.7 AcrB and Mutant Bind AcrA with Similar Affinities
Two-fold dilutions of wildtype AcrA (62.5 nM – 2 µM) was injected over the control, wildtype AcrB (**A**) and $AcrB_{D408A}$ (**B**) surfaces of the COOH5 chip. Protein samples in 20 mM MES (6.0), 150 mM NaCl, and 0.03% DDM were injected at 50 µl/min for 2 minutes (association phase) and then stopped for 2 minutes (dissociation phase). Sensograms were normalized to the control surface.

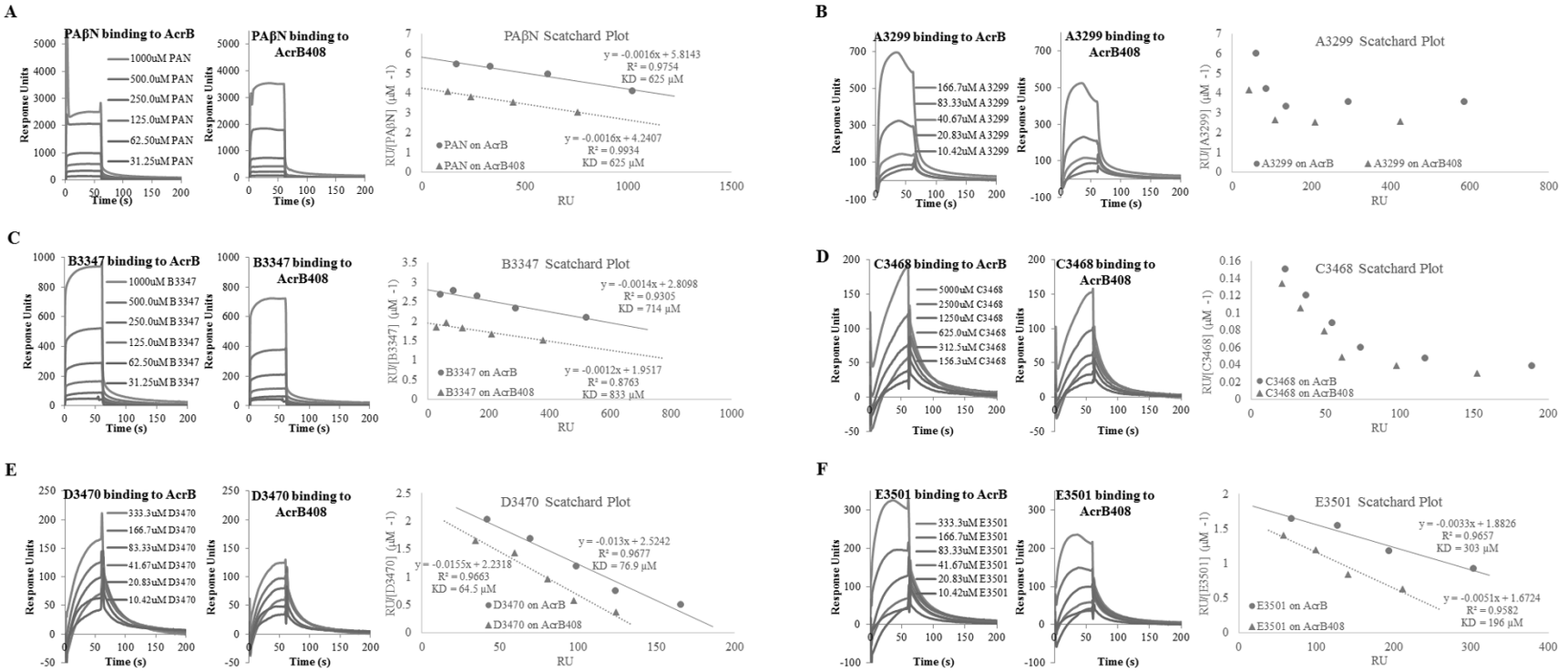

Figure 5.0.8 Binding Curves and Scatchard Plots of Basilea Inhibitors with AcrB and AcrBD408A.
A-F. Small molecules were injected over the protein surfaces in two-fold concentration increases. Binding equilibrium constants were determined from the Scatchard plots, the negative reciprocal of plot slopes. A3299 and C3468 showed evidence of negative cooperative binding of substrate to the transporter proteins (B, D).

5.2 Immobilized AcrB and Its Non-Functional Mutant Bind EPIs.

AcrB functions as a trimer with two binding pockets per monomer. The distal binding pocket has a phenylalanine-rich region that binds low-molecular-weight drugs and a proximal binding pocket and vestibule which binds larger compounds [88, 89]. To determine whether the immobilized AcrB variants were capable of binding the inhibitors and further compare the affinities, two fold dilutions of inhibitors were injected over the AcrB surfaces and the control surface in 20 mM MES running buffer (pH 6.0) supplemented with 150 mM NaCl, 0.03% DDM, and 5% DMSO (solvent for the small molecules).

Table 5.0.2 Kinetic Parameters of Basilea EPI Binding to AcrB and Mutant
Equilibrium constants represent the ratio of the dissociation and association rate constants. Data was analyzed using Scatchard plots

	K_D (μM)	
	AcrB	$AcrB_{D408A}$
PAβN	625	625
A3299	N/A	N/A
B3347	714	833
C3468	N/A	N/A
D3470	76.9	64.5
E3501	303	196

Out of nine EPIs, 5 bound the immobilized AcrB. The binding of B3347 had the greatest responses, implying that it may have multiple binding sites on AcrB. The binding curves of B3347 reached steady-state, as was seen with PAβN, within the one-minute injection time (Figure 5.0.8A, C). The binding curves of A3299 and E3501 also reached steady-state within the experimental parameters, but at higher concentrations they showed a decrease in signal, possibly due to non-specific effects (Figure 5.0.8B, F).

Despite the inactivation of AcrB protein functionality with the D408A mutation, the mutant AcrB was able to bind the small molecules with comparable affinities to that of wildtype AcrB (Table 5.0.2), indicating that this inactivation does not affect substrate binding interactions with the binding pockets of AcrB. The small difference of binding response units and affinities could be accounted to the difference of AcrB immobilized to the chip surface.

5.3 Binding Affinities of EPIs Are Dependent on the Amount of AcrB Present.

The amount of AcrB within the *E. coli* cell was reported to be ~500 copies, compared to AcrA's 5000-7000 copies, and TolC's ~1500 copies [32]. In our experiments, we tested the effect of AcrB and substrate binding and kinetics. Using thiol coupling, we immobilized wildtype AcrB on two surfaces of the sensor chip; surface densities of immobilized proteins was 4706 RU for the low density surface, and 6523 RU for the high density surface. Several substrates were used in experiments, and the kinetic parameters were analyzed by Scatchard plot representations (Figure 5.0.9).

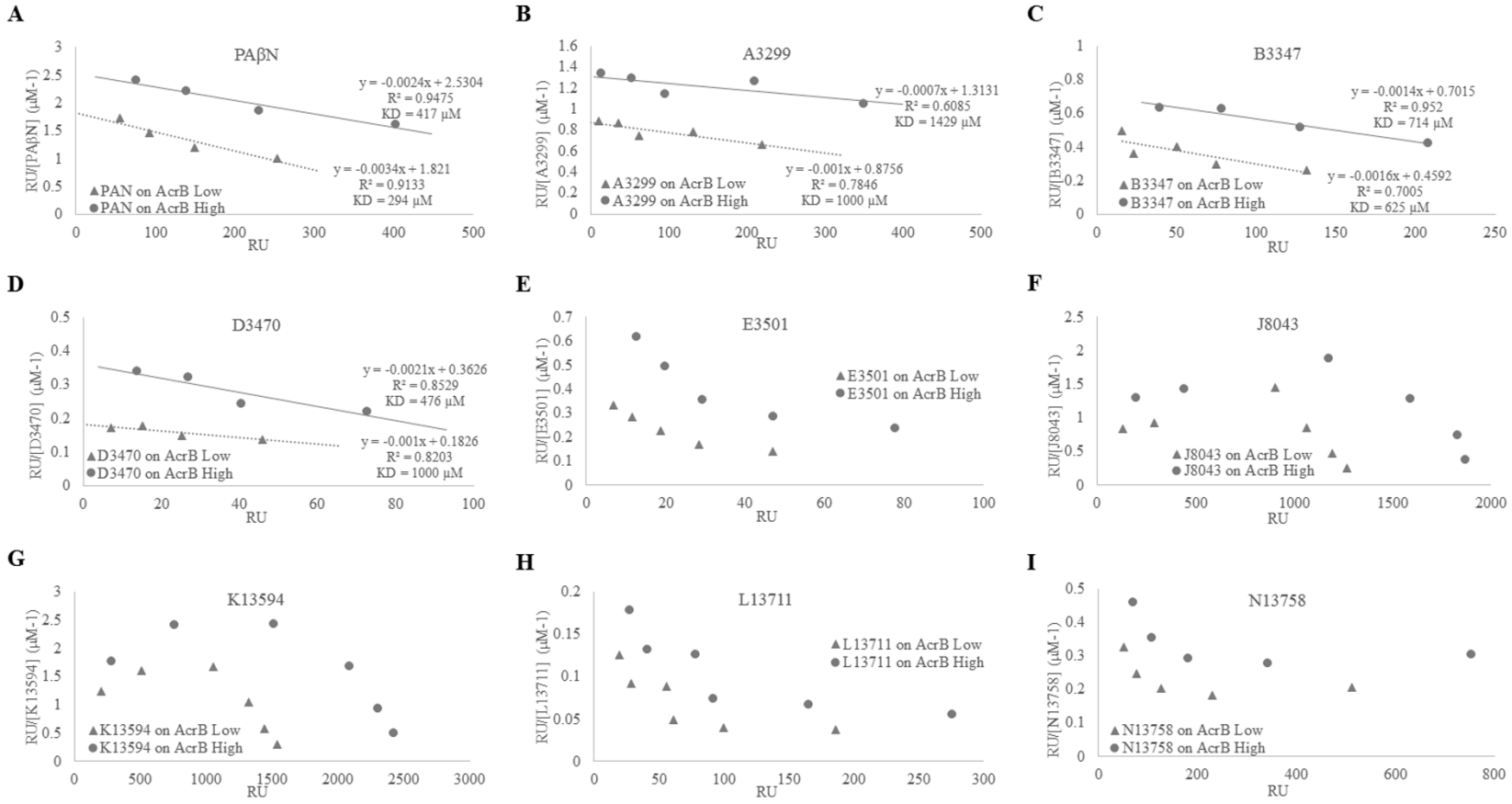

Figure 5.0.9 Scatchard Representation of AcrB-Dependent Substrate Binding

Basilea EPIs were injected over AcrB surfaces of two different surface densities, ~4700 RU (AcrB Low) and ~6500 RU (AcrB High). **A – I.** The Scatchard representation was used to define equilibrium constants (A-D), negative (E, H, I) and positive (F,G) cooperativity patterns.

Affinity constants of PAβN, A3299, B3468, and D3470 were determined by the negative reciprocal of the plot slopes (Figure 5.0.9A-D). Except D3470, the micromolar equilibrium constants correlated with the corresponding surface density of AcrB (Table 5.0.3). As compared to the previous sensor chip with even higher AcrB on the surface, E3501 showed characteristics of negative cooperativity interactions with AcrB at these lower densities of immobilization (Figure 5.0.9E). This suggested that binding of the substrate to AcrB decreases the binding of more substrate in another active site. The same relationship of binding interactions was seen for L13711 and N13758 (Figure 5.0.9H, I). For J8043 and K13594, we observed binding that indicated strong positive cooperativity interactions, both reaching saturation at ~0.625 mM of substrate.

Table 5.0.3 AcrB-Dependent Substrate Binding Affinities
Equilibrium constants of substrate binding is dependent on the amount of AcrB present. AcrB (low), ~4700 RU, and AcrB (high), ~6500 RU, were immobilized by thiol coupling on the SensíQ® Pioneer. Data was analyzed using Scatchard plots.

	K_D (μM)	
	AcrB (low)	AcrB (high)
PAβN	294	417
A3299	1000	1429
B3347	625	714
D3470	1000	476

5.4 Immobilization of AcrA, AcrB and TolC on the Biacore 3000.

The Biacore 3000 unit is a widely used instrument for studying kinetic interactions of biological molecules and structures alike. The sensor chip variations for the Biacore 3000 are comparable to that of the SensíQ® Pioneer, however, one major advantage is the availability of an extra surface which is also independently accessed

for immobilization and experiments. Taking advantage of this, we sought to check the specificity of substrate interactions with AcrB. To do this, we immobilized $AcrA_{S362C}$ and $TolC_{A269C,}$ alongside $AcrB_{S1043C,}$ to orient the proteins in the position of interest for protein-substrate studies (Figure 5.0.4, 5). We used thiol coupling, as discussed before, and attained 2308 RU for AcrA, 12216 RU for AcrB, and 2399 RU for TolC on the sensor surfaces. Per the Biacore manual, 100 RU of response on the CM5 chip is equivalent to 1mg/ml bulk concentration. Therefore, we immobilized ~500 μM AcrA, ~1000 μM AcrB, and ~450 μM TolC. We validated the integrity of the immobilized proteins by injecting PAβN on the AcrA, AcrB, and TolC protein surfaces. There was concentration-dependent substrate binding with acrA and AcrB, but not TolC (data not shown). After this, we proceeded to characterize substrate binding kinetics.

5.5 Basilea EPIs Bind More Specifically to AcrB than to AcrA or TolC

We tested the specificity of binding by the Basilea inhibitors to AcrB by checking binding interactions with AcrA and TolC, alike. We injected increasing concentrations of substrate on each protein surface and analyzed the sensograms, as corrected with the control surface (Figure 5.0.10). Despite the 1 AcrA:2 AcrB:1 TolC ratios of protein immobilization, the binding responses of the substrates do not reflect the same ratios. We observed that there was some binding of A3299, B3347, F5718, L13711 and N13758 to AcrA (Figure 5.0.11) and TolC (Figure 5.0.12), however, the binding curves varied in shapes for the substrate-protein pairs. Analysis of the binding responses with respect to substrate concentrations showed that these produced 3-10

times more binding responses to AcrB than to AcrA or TolC (data not shown). J8043 binding responses to

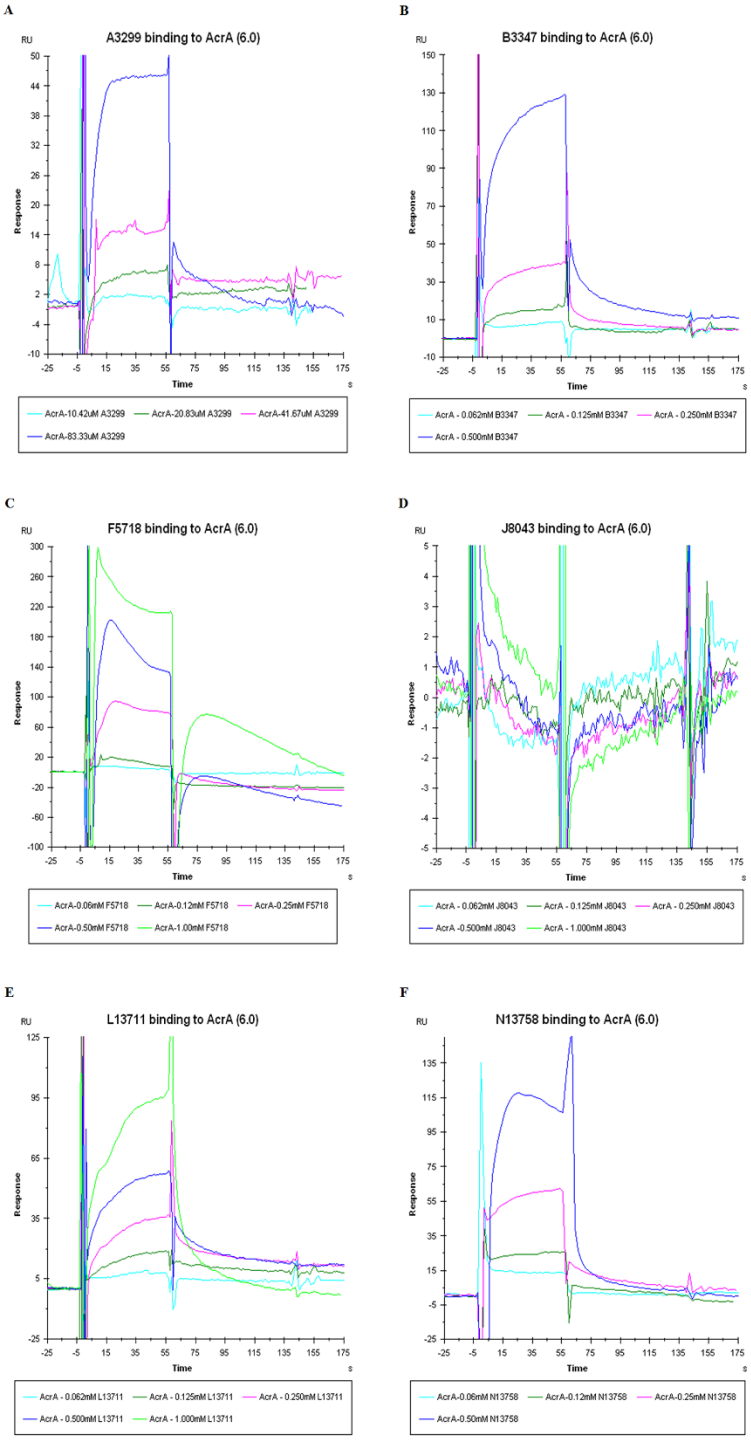

Figure 5.0.10 Inhibitors Bind AcrA
Sensograms of two-fold dilutions of A. A3299, B. B3347, C. F5718, D. J8043, E. L13711, and F. N13758, injected over AcrA (2308 RU) in MES running buffer (pH 6.0) supplemented with NaCl, DDM, and DMSO.

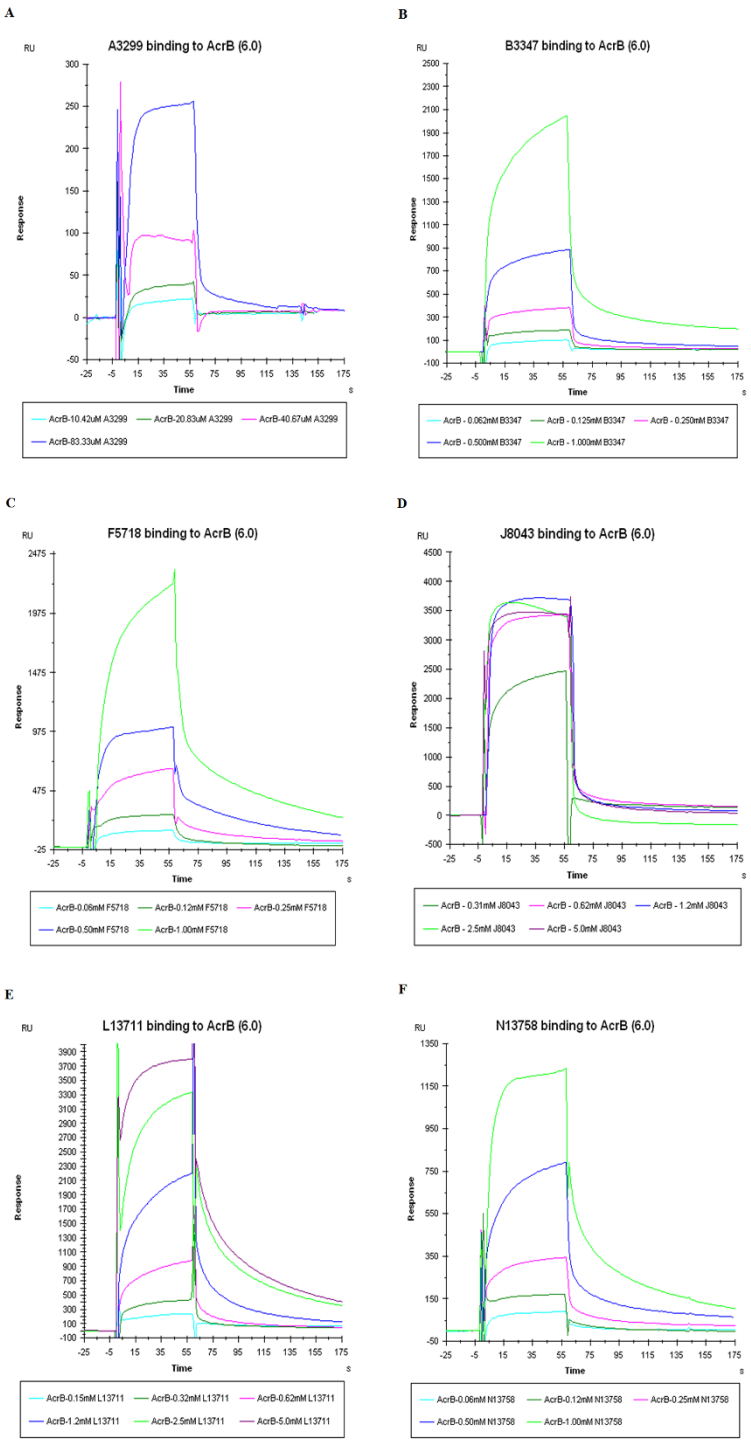

Figure 5.0.11 Inhibitors Bind AcrB
Sensograms of two-fold dilutions of A. A3299, B. B3347, C. F5718, D. J8043, E. L13711, and F. N13758, injected over AcrB (12216 RU) in MES running buffer (pH 6.0) supplemented with NaCl, DDM, and DMSO.

AcrB was 10-40 times higher than that of TolC; there was no binding to AcrA (Figure

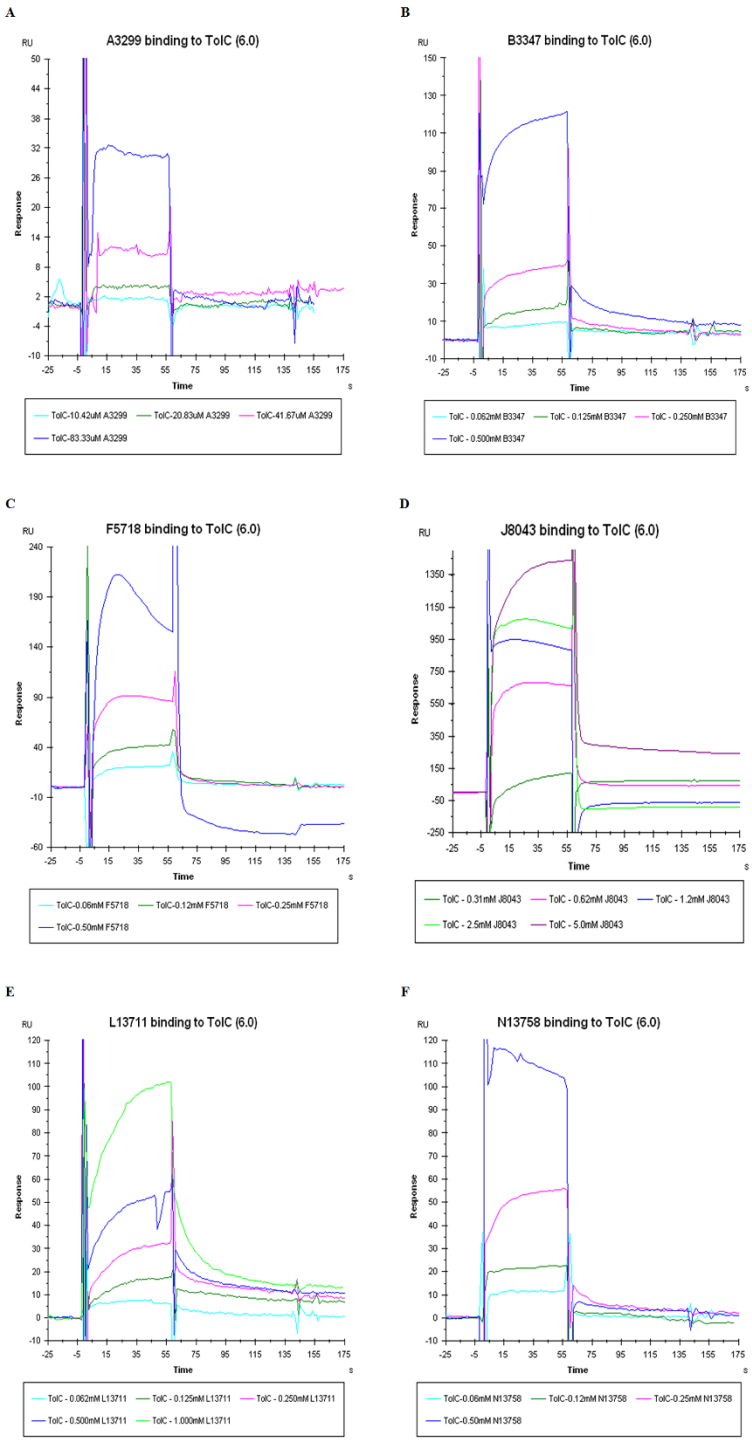

Figure 5.0.12 Inhibitors Bind TolC
Sensograms of two-fold dilutions of A. A3299, B. B3347, C. F5718, D. J8043, E. L13711, and F. N13758, injected over TolC (2399 RU) in MES running buffer (pH 6.0) supplemented with NaCl, DDM, and DMSO.

5.0.10D, 11D, 12D).

5.6 AcrB-Inhibitor Interactions Model a Bivalent Analyte or Two-State Model

We fit the binding curves to kinetic models in the BIAEvaluation software such as the 1:1 binding model, sequential binding model, and two-state model (TS). Global fittings are used to model and fit multiple fold-dilution injections of the same analyte (Figure 5.0.13A). Kinetic parameters produced from the fitting includes rates of

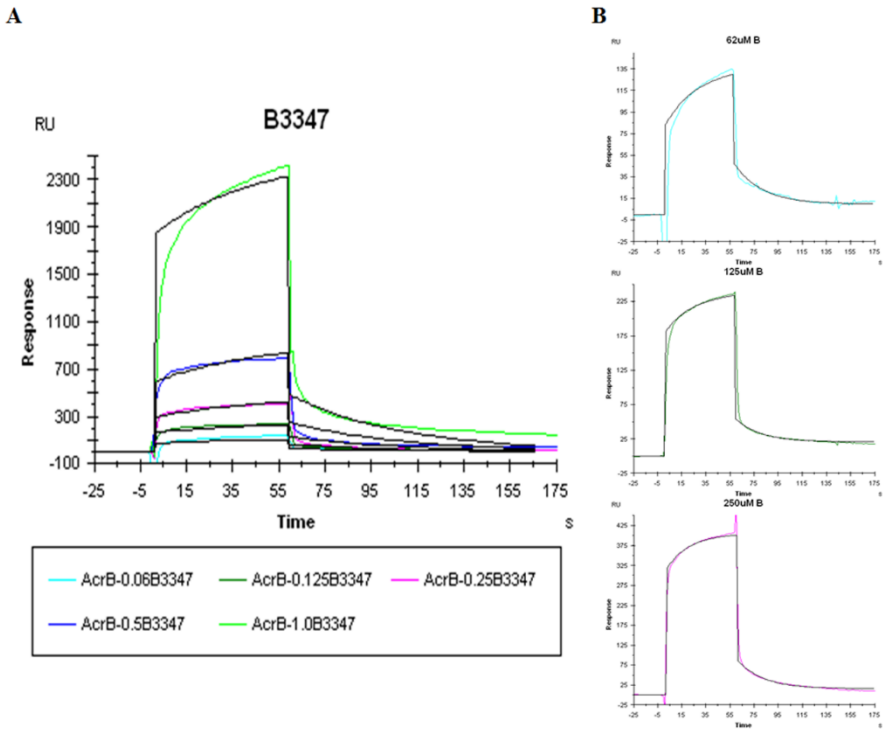

Figure 5.0.13 Global and Local Fitting of B3347
A. Global fitting of concentration-dependent B3347 binding to wildtype AcrB. All binding curves are fit simultaneously to describe the overall binding model in this case it was the Bivalent Analyte model. **B**. Local fittings of B3347 allowed for individual modeling of the binding curves at each of the various concentrations. A more accurate fitting of the single curves produces more accurate rates of association and dissociation association (k_a) and dissociation (k_d), the maximum achievable signal of ligand-analyte pairs (R_{max}), the bulk signal (RI) from the difference of flow buffer and analyte buffer used to better fit binding curves, and Chi^2 to give the measure of the accuracy of fit. Local fittings of binding curves allow for the individual analyte injections to be analyzed separately (Figure 5.0.13B). The same parameters are determined for local

fits as with global fits. Modeling the individual injections to the same model as the global allow for more accurate measurements of each binding curve. It also allows for the distinction of different patterns of binding within the same analyte as concentrations are varied.

We found that the best model, using global and local fittings, for A3299, B3347, F5718, J8043, and N13758 was the bivalent analyte (BA) model. This assumes that binding at the first analyte site facilitates binding at the second site, provided the analyte and ligand are in close proximity (Equation 5.1). The dissociation rates in bivalent

$$L + A \underset{k_{d1}}{\overset{k_{a1}}{\rightleftarrows}} LA + A \underset{k_{d2}}{\overset{k_{a2}}{\rightleftarrows}} LAA$$

Equation 5.0.1 Bivalent Analyte Model Reaction Equation

analyte models are slower than when there is only a single site of binding because dissociation must occur at both substrate binding sites.

Table 5.0.4 Kinetic Parameters of AcrB-Inhibitor Interactions
Data were globally fit using the BA model, k_{-1}, k_{-2}, k_1 and k_2 are microscopic rate constants. Equilibrium dissociation constants (K_D) were calculated from the ratios of the dissociation and association rate constants.

	k_{a1} ($M^{-1}s^{-1}$)	k_{d1} (s^{-1})	k_{a2} ($RU^{-1}s^{-1}$)	k_{d2} (s^{-1})	K_D (M)	Chi
A3299	2.35E+01	1.77E-02	4.74E-06	1.74E-01	2.76E+01	22.7
B3347	1.28E+00	2.12E-02	5.07E-07	1.09E-01	3.56E+03	1090
F5718	5.00E+01	1.41E-02	1.45E-05	2.11E-05	4.10E-04	122000
J8043	6.34E+02	3.71E-01	1.59E-06	5.55E-03	2.04E+00	9400
N13758	4.37E+00	8.10E-02	1.32E-06	1.54E-03	2.16E+01	830

Analysis of B3347 by global and local fitting showed that the rates of association was slower, while rates of dissociation were faster, in the individual injects than was reported for the global fitting (Table 5.0.4, 5). Chi^2 values show that the accuracy of measurements of the single injections are better than with the global fitting.

Table 5.0.5 Kinetic Parameters of B3347 from Local Fitting
B3347 was analyzed by fitting the individual binding curves at the different concentrations. Kinetic parameters, using the Bivalent Analyte model, showed more accurate, yet varied rates than was observed with the global fitting.

	k_{a1} ($M^{-1}s^{-1}$)	k_{d1} (s^{-1})	k_{a2} ($RU^{-1}s^{-1}$)	k_{d2} (s^{-1})	R_{max} (RU)	RI (RU)	Chi^2
62.5 μM B3347	18.6	4.00E-02	4.35E-06	6.10E-06	906	82.2	7.03
125. μM B3347	42.8	4.11E-02	3.89E-05	9.67E-05	254	179	0.998
250. μM B3347	28.3	4.35E-02	1.10E-05	2.35E-05	354	314	2.49

Unlike the other inhibitors analyzed on the Biacore 3000, L13711 binding to AcrB followed the Two-State (TS) model. This model (Equation 5.0.2) suggests that upon binding of substrate, the substrate-ligand complex undergoes a conformational

$$L + A \underset{k_{d1}}{\overset{k_{a1}}{\rightleftarrows}} LA \underset{k_{d2}}{\overset{k_{a2}}{\rightleftarrows}} (LA)^{\dagger}$$

Equation 5.0.2 Two-State Binding Model Reaction Equation

change to facilitate the binding of a second substrate. The final substrate-ligand complex is the most stable conformation, and dissociation of this complex into the independent partners requires a dissociation first to the intermediate conformation.

Global fitting showed that L13711 binding to AcrB had rates of 19.5 $M^{-1}s^{-1}$, 9.37E-02 s^{-1}, 1.41E-02 RU^{-1}, and 1.47E-02 s^{-1} for k_{a1}, k_{d1}, k_{a2} and k_{d2}, respectively. This yields an equilibrium constant of 5.01E-02 M, meaning that despite the expected stability of the substrate-ligand, dissociation is much faster than association of binding partners.

Taken together, we illustrate that protein immobilization by thiol coupling allows for reversible binding of ligand of interest. We show and confirm the binding of more than one substrate to AcrB. While equilibrium constants could not be determined for all tested inhibitors, we were able to characterize the binding patterns by their modes

of cooperative binding. We have, amongst these samples of molecules, potential inhibitors that can be used in tandem with therapeutics to destruct efflux pump functionality.

III. Conclusions

Transporter proteins of multidrug efflux pumps are a good target for efflux pump inhibitors. Basilea inhibitors showed preferred binding to the transporter protein (AcrB) than to the periplasmic adapter protein (AcrA) or the outer membrane channel protein (TolC). Binding interactions were categorized into the Bivalent Analyte and the Two-State binding models. Both models indicate a transition state prior to the final, stable complex of protein and inhibitor.

Fluorescence spectroscopy with pyrene proved a lack of interaction of AcrA-TolC at previously highlighted amino acid positions. Experiments with TriABC-OpmH proved that the bridging model of interactions between membrane fusion proteins and the channel protein was not valid.

Structural analysis of TriABC showed a stable complex in solution. TriC is an RND transporter exhibiting all three domains of the protein family. Although the TriAB structures were not fully resolved, we present an assembled transporter-MFP complex that positions the MFP on the pore and OMP docking domain, as previously postulated. In these studies, we prove that non-equivalent roles of the heterodimeric MFP pair. Assembling asymmetrically around the channel protein, one MFP recruits and assembles the efflux pump complex while the other stabilized interactions for complex functionality. The recruiter MFP, located in the intraprotomer groove of the outer membrane protein, is responsible for the opening of the periplasmic aperture to allow expulsion of substrates of varying classes and function. The stabilizer MFP, located in the interprotomer groove, assumes two different conformations in the presence and absence of the channel protein. A loss of function mutation in the α-

helical domain of this dimeric pair does not disrupt the integrity of the efflux complex. These studies present new information about the interactions of proteins and offer more insight into the mechanism of efflux pump complexes.

References

[1] Long, F., Su, C. C., Lei, H. T., Bolla, J. R., Do, S. V., and Yu, E. W. (2012) Structure and mechanism of the tripartite CusCBA heavy-metal efflux complex, *Philos Trans R Soc Lond B Biol Sci 367*, 1047-1058.

[2] Murakami, S., Nakashima, R., Yamashita, E., and Yamaguchi, A. (2002) Crystal structure of bacterial multidrug efflux transporter AcrB, *Nature 419*, 587-593.

[3] Pos, K. M. (2009) Drug transport mechanism of the AcrB efflux pump, *Biochimica et biophysica acta 1794*, 782-793.

[4] Kelley, L. A., Mezulis, S., Yates, C. M., Wass, M. N., and Sternberg, M. J. (2015) The Phyre2 web portal for protein modeling, prediction and analysis, *Nat Protoc 10*, 845-858.

[5] Kumar, S., Mukherjee, M. M., and Varela, M. F. (2013) Modulation of Bacterial Multidrug Resistance Efflux Pumps of the Major Facilitator Superfamily, *International Journal of Bacteriology 2013*, 15.

[6] Cooper, M. A. (2002) Optical biosensors in drug discovery, *Nat Rev Drug Discov 1*, 515-528.

[7] Zgurskaya, H. I., Weeks, J. W., Ntreh, A. T., Nickels, L. M., and Wolloscheck, D. (2015) Mechanism of coupling drug transport reactions located in two different membranes, *Front Microbiol 6*, 100.

[8] Song, S., Kim, J.-S., Lee, K., and Ha, N.-C. (2015) Molecular architecture of the bacterial tripartite multidrug efflux pump focusing on the adaptor bridging model, *Journal of Microbiology 53*, 355-364.

[9] Symmons, M. F., Marshall, R. L., and Bavro, V. N. (2015) Architecture and roles of periplasmic adaptor proteins in tripartite e ffl ux assemblies, *Front Microbiol 6*, 513.

[10] Nikaido, H. (2009) Multidrug resistance in bacteria, *Annual review of biochemistry 78*, 119-146.

[11] Piddock, L. J. V. (2006) Multidrug-resistance efflux pumps- not just for resistance, *Nature Reviews Microbiology*, 629-636.

[12] Pao, S. S., Paulsen, I. T., and Saier, M. H., Jr. (1998) Major facilitator superfamily, *Microbiology and molecular biology reviews : MMBR 62*, 1-34.

[13] Bay, D. C., Rommens, K. L., and Turner, R. J. (2008) Small multidrug resistance proteins: a multidrug transporter family that continues to grow, *Biochimica et biophysica acta 1778*, 1814-1838.

[14] Moriyama, Y., Hiasa, M., Matsumoto, T., and Omote, H. (2008) Multidrug and toxic compound extrusion (MATE)-type proteins as anchor transporters for the excretion of metabolic waste products and xenobiotics, *Xenobiotica 38*, 1107-1118.

[15] Tseng, T. T., Gratwick, K. S., Kollman, J., Park, D., Nies, D. H., Goffeau, A., and Saier, M. H., Jr. (1999) The RND permease superfamily: an ancient, ubiquitous and diverse family that includes human disease and development proteins, *J Mol Microbiol Biotechnol 1*, 107-125.

[16] Hassan, K. A., Liu, Q., Henderson, P. J., and Paulsen, I. T. (2015) Homologs of the Acinetobacter baumannii AceI transporter represent a new family of bacterial multidrug efflux systems, *MBio 6*.

[17] Zhou, G., Shi, Q. S., Huang, X. M., and Xie, X. B. (2015) The Three Bacterial Lines of Defense against Antimicrobial Agents, *Int J Mol Sci 16*, 21711-21733.

[18] Askoura, M., Mottawea, W., Abujamel, T., and Taher, I. (2011) Efflux pump inhibitors (EPIs) as new antimicrobial agents against Pseudomonas aeruginosa, *Libyan J Med 6*.

[19] Nikaido, H., and Zgurskaya, H. I. (1999) Antibiotic efflux mechanisms, *Curr Opin Infect Dis 12*, 529-536.

[20] Zgurskaya, H. I., and Nikaido, H. (1999) AcrA is a highly asymmetric protein capable of spanning the periplasm, *J Mol Biol 285*, 409-420.

[21] Akama, H., Kanemaki, M., Yoshimura, M., Tsukihara, T., Kashiwagi, T., Yoneyama, H., Narita, S., Nakagawa, A., and Nakae, T. (2004) Crystal structure of the drug discharge outer membrane protein, OprM, of Pseudomonas aeruginosa: dual modes of membrane anchoring and occluded cavity end, *The Journal of biological chemistry 279*, 52816-52819.

[22] Mikolosko, J., Bobyk, K., Zgurskaya, H. I., and Ghosh, P. (2006) Conformational flexibility in the multidrug efflux system protein AcrA, *Structure 14*, 577-587.

[23] Lobedanz, S., Bokma, E., Symmons, M. F., Koronakis, E., Hughes, C., and Koronakis, V. (2007) A periplasmic coiled-coil interface underlying TolC recruitment and the assembly of bacterial drug efflux pumps, *Proceedings of the National Academy of Sciences of the United States of America 104*, 4612-4617.

[24] Bokma, E., Koronakis, E., Lobedanz, S., Hughes, C., and Koronakis, V. (2006) Directed evolution of a bacterial efflux pump: adaptation of the E. coli TolC exit duct to the Pseudomonas MexAB translocase, *FEBS letters 580*, 5339-5343.

[25] Tikhonova, E. B., Dastidar, V., Rybenkov, V. V., and Zgurskaya, H. I. (2009) Kinetic control of TolC recruitment by multidrug efflux complexes, *Proceedings of the National Academy of Sciences of the United States of America 106*, 16416-16421.

[26] Paulsen, I. T., Park, J. H., Choi, P. S., and Saier, M. H., Jr. (1997) A family of gram-negative bacterial outer membrane factors that function in the export of proteins, carbohydrates, drugs and heavy metals from gram-negative bacteria, *FEMS Microbiol Lett 156*, 1-8.

[27] Koronakis, V., Sharff, A., Koronakis, E., Luisi, B., and Hughes, C. (2000) Crystal structure of the bacterial membrane protein TolC central to multidrug efflux and protein export, *Nature 405*, 914-919.

[28] Federici, L., Du, D., Walas, F., Matsumura, H., Fernandez-Recio, J., McKeegan, K. S., Borges-Walmsley, M. I., Luisi, B. F., and Walmsley, A. R. (2005) The crystal structure of the outer membrane protein VceC from the bacterial pathogen Vibrio cholerae at 1.8 A resolution, *The Journal of biological chemistry 280*, 15307-15314.

[29] Kulathila, R., Kulathila, R., Indic, M., and van den Berg, B. (2011) Crystal structure of Escherichia coli CusC, the outer membrane component of a heavy metal efflux pump, *PloS one 6*, e15610.

[30] Lei, H. T., Chou, T. H., Su, C. C., Bolla, J. R., Kumar, N., Radhakrishnan, A., Long, F., Delmar, J. A., Do, S. V., Rajashankar, K. R., Shafer, W. M., and Yu, E. W. (2014) Crystal structure of the open state of the Neisseria gonorrhoeae MtrE outer membrane channel, *PloS one 9*, e97475.

[31] Lu, S., and Zgurskaya, H. I. (2013) MacA, a periplasmic membrane fusion protein of the macrolide transporter MacAB-TolC, binds lipopolysaccharide core specifically and with high affinity, *Journal of bacteriology 195*, 4865-4872.

[32] Tikhonova, E. B., and Zgurskaya, H. I. (2004) AcrA, AcrB, and TolC of Escherichia coli Form a Stable Intermembrane Multidrug Efflux Complex, *The Journal of biological chemistry 279*, 32116-32124.

[33] Weeks, J. W., Nickels, L. M., Ntreh, A. T., and Zgurskaya, H. I. (2015) Non-equivalent roles of two periplasmic subunits in the function and assembly of triclosan pump TriABC from Pseudomonas aeruginosa, *Mol Microbiol 98*, 343-356.

[34] Nikaido, H. (2003) Molecular basis of bacterial outer membrane permeability revisited, *Microbiology and molecular biology reviews : MMBR 67*, 593-656.

[35] Yen, M.-R., Peabody, C. R., Partovi, S. M., Zhai, Y., Tseng, Y.-H., and Saier Jr, M. H. (2002) Protein-translocating outer membrane porins of Gram-negative bacteria, *Biochimica et Biophysica Acta (BBA) - Biomembranes 1562*, 6-31.

[36] Zgurskaya, H. I. (2009) Multicomponent drug efflux complexes: architecture and mechanism of assembly, *Future microbiology 4*, 919-932.

[37] Andersen, C., Koronakis, E., Bokma, E., Eswaran, J., Humphreys, D., Hughes, C., and Koronakis, V. (2002) Transition to the open state of the TolC periplasmic tunnel entrance, *Proceedings of the National Academy of Sciences of the United States of America 99*, 11103-11108.

[38] Seeger, M. A., Diederichs, K., Eicher, T., Brandstatter, L., Schiefner, A., Verrey, F., and Pos, K. M. (2008) The AcrB efflux pump: conformational cycling and peristalsis lead to multidrug resistance, *Curr Drug Targets 9*, 729-749.

[39] Murakami, S., Nakashima, R., Yamashita, E., Matsumoto, T., and Yamaguchi, A. (2006) Crystal structures of a multidrug transporter reveal a functionally rotating mechanism, *Nature 443*, 173-179.

[40] Seeger, M. A., Schiefner, A., Eicher, T., Verrey, F., Diederichs, K., and Pos, K. M. (2006) Structural asymmetry of AcrB trimer suggests a peristaltic pump mechanism, *Science 313*, 1295-1298.

[41] Su, C. C., Long, F., Zimmermann, M. T., Rajashankar, K. R., Jernigan, R. L., and Yu, E. W. (2011) Crystal structure of the CusBA heavy-metal efflux complex of Escherichia coli, *Nature 470*, 558-562.

[42] Du, D., Wang, Z., James, N. R., Voss, J. E., Klimont, E., Ohene-Agyei, T., Venter, H., Chiu, W., and Luisi, B. F. (2014) Structure of the AcrAB-TolC multidrug efflux pump, *Nature 509*, 512-515.

[43] Symmons, M. F., Bokma, E., Koronakis, E., Hughes, C., and Koronakis, V. (2009) The assembled structure of a complete tripartite bacterial multidrug efflux pump, *Proceedings of the National Academy of Sciences of the United States of America 106*, 7173-7178.

[44] Tikhonova, E. B., Yamada, Y., and Zgurskaya, H. I. (2011) Sequential mechanism of assembly of multidrug efflux pump AcrAB-TolC, *Chemistry & biology 18*, 454-463.

[45] Touze, T., Eswaran, J., Bokma, E., Koronakis, E., Hughes, C., and Koronakis, V. (2004) Interactions underlying assembly of the Escherichia coli AcrAB-TolC multidrug efflux system, *Mol Microbiol 53*, 697-706.

[46] Xu, Y., Song, S., Moeller, A., Kim, N., Piao, S., Sim, S. H., Kang, M., Yu, W., Cho, H. S., Chang, I., Lee, K., and Ha, N. C. (2011) Functional implications of an intermeshing cogwheel-like interaction between TolC and MacA in the action of macrolide-specific efflux pump MacAB-TolC, *The Journal of biological chemistry 286*, 13541-13549.

[47] Yum, S., Xu, Y., Piao, S., Sim, S. H., Kim, H. M., Jo, W. S., Kim, K. J., Kweon, H. S., Jeong, M. H., Jeon, H., Lee, K., and Ha, N. C. (2009) Crystal structure of the periplasmic component of a tripartite macrolide-specific efflux pump, *J Mol Biol 387*, 1286-1297.

[48] Ge, Q., Yamada, Y., and Zgurskaya, H. (2009) The C-terminal domain of AcrA is essential for the assembly and function of the multidrug efflux pump AcrAB-TolC, *Journal of bacteriology 191*, 4365-4371.

[49] Mima, T., Joshi, S., Gomez-Escalada, M., and Schweizer, H. P. (2007) Identification and characterization of TriABC-OpmH, a triclosan efflux pump of Pseudomonas aeruginosa requiring two membrane fusion proteins, *Journal of bacteriology 189*, 7600-7609.

[50] Chuanchuen, R., Beinlich, K., Hoang, T. T., Becher, A., Karkhoff-Schweizer, R. R., and Schweizer, H. P. (2001) Cross-resistance between triclosan and antibiotics in Pseudomonas aeruginosa is mediated by multidrug efflux pumps: exposure of a susceptible mutant strain to triclosan selects nfxB mutants overexpressing MexCD-OprJ, *Antimicrobial agents and chemotherapy 45*, 428-432.

[51] Faccone, D., Guerriero, L., Mendez, E., Errecalde, L., Cano, H., Yoyas, N., Togneri, A., Romanowski, V., Galas, M., Whonet, R., Corso, A., and Red, W. (2010) Fluoroquinolone-resistant Streptococcus agalactiae isolates from Argentina, *Rev Argent Microbiol 42*, 203-207.

[52] Dhamdhere, G., and Zgurskaya, H. I. (2010) Metabolic shutdown in Escherichia coli cells lacking the outer membrane channel TolC, *Mol Microbiol 77*, 743-754.

[53] Watson, J. M., and Holloway, B. W. (1978) Linkage map of Pseudomonas aeruginosa PAT, *Journal of bacteriology 136*, 507-521.

[54] Miyamae, S., Ueda, O., Yoshimura, F., Hwang, J., Tanaka, Y., and Nikaido, H. (2001) A MATE family multidrug efflux transporter pumps out fluoroquinolones in Bacteroides thetaiotaomicron, *Antimicrobial agents and chemotherapy 45*, 3341-3346.

[55] Gilson, L., Mahanty, H. K., and Kolter, R. (1990) Genetic analysis of an MDR-like export system: the secretion of colicin V, *EMBO J 9*, 3875-3884.

[56] Schweizer HP, H. T., Propst KL, Ornelas HR, Karkhoff-Schweizer RR. (2001) vector design and host systems forPseudomonas, In *Genetic Engineering* (JK, S., Ed.), Kluwer Plenum.

[57] Guzman, L. M., Belin, D., Carson, M. J., and Beckwith, J. (1995) Tight regulation, modulation, and high-level expression by vectors containing the arabinose PBAD promoter, *Journal of bacteriology 177*, 4121-4130.

[58] Chuanchuen, R., Murata, T., Gotoh, N., and Schweizer, H. P. (2005) Substrate-dependent utilization of OprM or OpmH by the Pseudomonas aeruginosa MexJK efflux pump, *Antimicrobial agents and chemotherapy 49*, 2133-2136.

[59] Damron, F. H., McKenney, E. S., Barbier, M., Liechti, G. W., Schweizer, H. P., and Goldberg, J. B. (2013) Construction of mobilizable mini-Tn7 vectors for bioluminescent detection of gram-negative bacteria and single-copy promoter lux reporter analysis, *Appl Environ Microbiol 79*, 4149-4153.

[60] Choi, K. H., Gaynor, J. B., White, K. G., Lopez, C., Bosio, C. M., Karkhoff-Schweizer, R. R., and Schweizer, H. P. (2005) A Tn7-based broad-range bacterial cloning and expression system, *Nat Methods 2*, 443-448.

[61] Bavro, V. N., Pietras, Z., Furnham, N., Perez-Cano, L., Fernandez-Recio, J., Pei, X. Y., Misra, R., and Luisi, B. (2008) Assembly and channel opening in a bacterial drug efflux machine, *Molecular cell 30*, 114-121.

[62] Pei, X. Y., Hinchliffe, P., Symmons, M. F., Koronakis, E., Benz, R., Hughes, C., and Koronakis, V. (2011) Structures of sequential open states in a symmetrical opening transition of the TolC exit duct, *Proceedings of the National Academy of Sciences of the United States of America 108*, 2112-2117.

[63] Krishnamoorthy, G., Tikhonova, E. B., Dhamdhere, G., and Zgurskaya, H. I. (2013) On the role of TolC in multidrug efflux: the function and assembly of AcrAB-TolC tolerate significant depletion of intracellular TolC protein, *Mol Microbiol 87*, 982-997.

[64] Ip, H., Stratton, K., Zgurskaya, H., and Liu, J. (2003) pH-induced conformational changes of AcrA, the membrane fusion protein of Escherichia coli multidrug efflux system, *The Journal of biological chemistry 278*, 50474-50482.

[65] Tikhonova, E. B., Wang, Q., and Zgurskaya, H. I. (2002) Chimeric analysis of the multicomponent multidrug efflux transporters from gram-negative bacteria, *Journal of bacteriology 184*, 6499-6507.

[66] Mindell, J. A., and Grigorieff, N. (2003) Accurate determination of local defocus and specimen tilt in electron microscopy, *J Struct Biol 142*, 334-347.

[67] Zhu, W., Zhang, Y., Sinko, W., Hensler, M. E., Olson, J., Molohon, K. J., Lindert, S., Cao, R., Li, K., Wang, K., Wang, Y., Liu, Y. L., Sankovsky, A., de Oliveira, C. A., Mitchell, D. A., Nizet, V., McCammon, J. A., and Oldfield, E. (2013) Antibacterial drug leads targeting isoprenoid biosynthesis, *Proceedings of the National Academy of Sciences of the United States of America 110*, 123-128.

[68] Elmlund, H., Elmlund, D., and Bengio, S. (2013) PRIME: probabilistic initial 3D model generation for single-particle cryo-electron microscopy, *Structure 21*, 1299-1306.

[69] Scheres, S. H. (2012) RELION: implementation of a Bayesian approach to cryo-EM structure determination, *J Struct Biol 180*, 519-530.

[70] Lehrer, S. S. (1997) Intramolecular pyrene excimer fluorescence: a probe of proximity and protein conformational change, *Methods Enzymol 278*, 286-295.

[71] Kim, H. M., Xu, Y., Lee, M., Piao, S., Sim, S. H., Ha, N. C., and Lee, K. (2010) Functional relationships between the AcrA hairpin tip region and the TolC aperture tip region for the formation of the bacterial tripartite efflux pump AcrAB-TolC, *Journal of bacteriology 192*, 4498-4503.

[72] Blair, J. M., La Ragione, R. M., Woodward, M. J., and Piddock, L. J. (2009) Periplasmic adaptor protein AcrA has a distinct role in the antibiotic resistance and virulence of Salmonella enterica serovar Typhimurium, *J Antimicrob Chemother 64*, 965-972.

[73] Bohnert, J. A., Karamian, B., and Nikaido, H. (2010) Optimized Nile Red efflux assay of AcrAB-TolC multidrug efflux system shows competition between substrates, *Antimicrobial agents and chemotherapy 54*, 3770-3775.

[74] Misra, R., Morrison, K. D., Cho, H. J., and Khuu, T. (2015) Importance of Real-Time Assays To Distinguish Multidrug Efflux Pump-Inhibiting and Outer Membrane-Destabilizing Activities in Escherichia coli, *Journal of bacteriology 197*, 2479-2488.

[75] Kamisetty, H., Ovchinnikov, S., and Baker, D. (2013) Assessing the utility of coevolution-based residue-residue contact predictions in a sequence- and structure-rich era, *Proceedings of the National Academy of Sciences of the United States of America 110*, 15674-15679.

[76] Ovchinnikov, S., Kamisetty, H., and Baker, D. (2014) Robust and accurate prediction of residue-residue interactions across protein interfaces using evolutionary information, *Elife 3*, e02030.

[77] Koronakis, V. (2003) TolC--the bacterial exit duct for proteins and drugs, *FEBS letters 555*, 66-71.

[78] Hermanson, G. T. (1996) *Bioconjugate Techniques*, Academic Press Inc.

[79] Sissi, C., and Palumbo, M. (2009) Effects of magnesium and related divalent metal ions in topoisomerase structure and function, *Nucleic Acids Res 37*, 702-711.

[80] Hirakata, Y., Kondo, A., Hoshino, K., Yano, H., Arai, K., Hirotani, A., Kunishima, H., Yamamoto, N., Hatta, M., Kitagawa, M., Kohno, S., and Kaku, M. (2009) Efflux pump inhibitors reduce the invasiveness of Pseudomonas aeruginosa, *Int J Antimicrob Agents 34*, 343-346.

[81] Lomovskaya, O., and Bostian, K. A. (2006) Practical applications and feasibility of efflux pump inhibitors in the clinic--a vision for applied use, *Biochem Pharmacol 71*, 910-918.

[82] Lomovskaya, O., Warren, M. S., Lee, A., Galazzo, J., Fronko, R., Lee, M., Blais, J., Cho, D., Chamberland, S., Renau, T., Leger, R., Hecker, S., Watkins, W., Hoshino, K., Ishida, H., and Lee, V. J. (2001) Identification and characterization of inhibitors of multidrug resistance efflux pumps in Pseudomonas aeruginosa: novel agents for combination therapy, *Antimicrobial agents and chemotherapy 45*, 105-116.

[83] Renau, T. E., Leger, R., Filonova, L., Flamme, E. M., Wang, M., Yen, R., Madsen, D., Griffith, D., Chamberland, S., Dudley, M. N., Lee, V. J., Lomovskaya, O., Watkins, W. J., Ohta, T., Nakayama, K., and Ishida, Y. (2003) Conformationally-restricted analogues of efflux pump inhibitors that potentiate the activity of levofloxacin in Pseudomonas aeruginosa, *Bioorg Med Chem Lett 13*, 2755-2758.

[84] Renau, T. E., Leger, R., Yen, R., She, M. W., Flamme, E. M., Sangalang, J., Gannon, C. L., Chamberland, S., Lomovskaya, O., and Lee, V. J. (2002) Peptidomimetics of efflux pump inhibitors potentiate the activity of levofloxacin in Pseudomonas aeruginosa, *Bioorg Med Chem Lett 12*, 763-766.

[85] Arima, Y., Toda, M., and Iwata, H. (2011) Surface plasmon resonance in monitoring of complement activation on biomaterials, *Adv Drug Deliv Rev 63*, 988-999.

[86] Seeger, M. A., von Ballmoos, C., Verrey, F., and Pos, K. M. (2009) Crucial role of Asp408 in the proton translocation pathway of multidrug transporter AcrB: evidence from site-directed mutagenesis and carbodiimide labeling, *Biochemistry 48*, 5801-5812.

[87] Perez, A., Poza, M., Fernandez, A., Fernandez Mdel, C., Mallo, S., Merino, M., Rumbo-Feal, S., Cabral, M. P., and Bou, G. (2012) Involvement of the AcrAB-TolC efflux pump in the resistance, fitness, and virulence of Enterobacter cloacae, *Antimicrobial agents and chemotherapy 56*, 2084-2090.

[88] Husain, F., Bikhchandani, M., and Nikaido, H. (2011) Vestibules are part of the substrate path in the multidrug efflux transporter AcrB of Escherichia coli, *Journal of bacteriology 193*, 5847-5849.

[89] Nakashima, R., Sakurai, K., Yamasaki, S., Nishino, K., and Yamaguchi, A. (2011) Structures of the multidrug exporter AcrB reveal a proximal multisite drug-binding pocket, *Nature 480*, 565-569.